

DEVELOPMENT OF STIMULI-RESPONSIVE POLYPEPTIDE-BASED GELATORS  
FOR BIOAPPLICATIONS AND PHOTO-PATTERNING TECHNOLOGIES

A Dissertation

by

XUN HE

Submitted to the Office of Graduate and Professional Studies of  
Texas A&M University  
in partial fulfillment of the requirements for the degree of

DOCTOR OF PHILOSOPHY

Chair of Committee,	Karen L. Wooley
Committee Members,	Kevin Burgess
	Lei Fang
	Melissa A. Grunlan
Head of Department,	Simon W. North

May 2017

Major Subject: Chemistry

Copyright 2017 Xun He

## ABSTRACT

The past decade has witnessed significantly increased interest in the development of smart polypeptide based organo- and hydrogel systems with stimuli responsiveness, especially those that exhibit sol–gel phase-transition properties, with an anticipation of their utility in the construction of adaptive materials, sensor designs, and controlled release systems, among other applications. This dissertation highlights the rational design and development of polypeptide-based gelators for simple and easily-controlled preparations toward bioapplications and photo-patterning technologies, including full characterization studies of the compositions, structures and properties.

The continuous N<sub>2</sub> flow technology for controlled ring-opening polymerization of *N*-carboxyanhydride (NCA) was recently developed in our lab for construction of well-defined polypeptides, facilitating the investigations of structure-property relationships within polypeptide materials. Based upon this technology, a multi-responsive triblock hydrogelator was synthesized, which exhibited heat-induced sol-to-gel transitions and either sonication- or enzyme-induced gel-to-sol transitions. The formation of  $\beta$  sheets further displayed tertiary ordering into fibrillar structures that, in turn generated a porous and interconnected hydrogel matrix. The reversible macroscopic sol-to-gel transitions triggered by heat and gel-to-sol transitions triggered by sonication were correlated with the transformation of nanostructural morphologies, with fibrillar structures observed in gel and spherical aggregates in sol, respectively. The enzymatic breakdown of the hydrogels was also investigated. This allyl-functionalized

hydrogelator can serve as a platform for the design of smart hydrogels, appropriate for expansion into biological systems as bio-functional and bio-responsive materials. This hydrogelator also displayed capability to dispersing and gelating single-walled carbon nanotubes (SWCNTs) noncovalently in organic solvents, resulting in significant enhancement of the mechanical properties of polypeptide based organogels and unique supramolecular structures, with results presenting in the second study. Based on the above two studies, a strategy for reversible patterning of soft conductive materials is developed. This strategy was enabled by a responsive composite that comprises peptide-based block copolymer hydrogelators and photo-thermally-active carbon nanotubes. This composite photo-responsive gelation at application relevant timescales ( $< 10$  s), allowing for rapid and spatially-defined construction of conductive patterns ( $> 100 \text{ S m}^{-1}$ ), which, additionally, hold the capability to revert to sol upon sonication for reprocessing.

## DEDICATION

To my father and mother

## ACKNOWLEDGEMENTS

I would first like to thank my Ph.D. advisor, Professor Karen L. Wooley. She is kind, supportive, passionate, diligent, and considerate. In addition to learning tremendous knowledge of science from her, I also learnt to be meticulous about experimental details, analytical towards observed phenomena, and most importantly, a good person. Although I have always been worrying about my contribution and how my gel projects fit into the big picture of our group, she never stopped providing me with freedom, support and suggestions to explore the fields that I deem interesting and exciting. Another important lesson I learnt from her is to achieve control of the outcome and do not hope, which is not pessimistic, but instead a fact of taking responsibility, an approach to maximize the possibility of success, and an attitude towards life. With these limited words, I cannot express all my gratitude of having her as my supervisor. However, I still want to thank her again sincerely for being a wonderful mentor.

I would also like to thank my committee members, Prof. Kevin Burgess, Prof. Lei Fang, and Prof. Melissa A. Grunlan for their valuable advice and stimulating discussions, which led to improved research toward the completion of this dissertation.

Within the Wooley group, I would first thank Dr. Jingwei Fan, Dr. Guorong Sun, and Dr. Jiong Zou for their great mentorship and friendship and I have learned many useful research skills and techniques from these talented scientists. I also want to acknowledge my mentee, Tan P. Nguyen, and my internal collaborators, Ms. Sarosh Khan, Mr. Richen Li, Dr. Soon-Mi Lim, Dr. Kevin A. Pollack, Dr. Jeffery E. Raymond,

and Dr. Fuwu Zhang for their great help in my research. Their professional opinions and practical advices are invaluable for my graduate research. I would also like to thank other past and present members of the Wooley group, Mr. Ryan Allen, Dr. Yannick Borguet, Dr. Yingchao Chen, Dr. Sangho Cho, Ms. Mei Dong, Dr. Mahmoud F. A. El Sabahy, Ms. Simcha E. Felder, Dr. Jeniree A. Flores Delgado, Mr. Daniel Dobbins, Dr. Marco Giles, Ms. Amelia Gonzalez, Ms. Alexis Gooch, Dr. Tiffany P. Gustafson, Ms. Jessica Huang, Dr. Ashlee Jahnke, Ms. Nari Kang, Mr. Christopher Komatsu, Dr. Gyu Seong Heo, Dr. Amandine Noel, Dr. Samantha L. Kristufek, Mr. Eric Leonhardt, Dr. Rachel Letteri, Dr. Young Lim, Mr. Yen-nan Lin, Dr. Lauren Link, Mr. Alexander Lonnecker, Ms. Casey McDonald, Ms. Sherry Melton, Mr. Andy Moutray, Mr. Shota Osumi, Dr. Adriana Pavia-Sanders, Ms. Danielle Policarpio Wolf, Ms. Stephanie Pollack, Ms. Randinu Pulukkody, Mr. Joel Russell, Dr. Sandani Samarajeewa, Dr. Kellie Seetho, Mr. Travis Smith, Mr. Justin Smolen, Ms. Yue Song, Dr. Lu Su, Mr. Matthew Svach, Ms. Judy Taylor, Mr. Yi-Yun Tsao, Mr. Eric Vavra, Ms. Virginia Vance, Ms. Mariela Vazquez, Ms. Brooke Versaw, Mr. Kevin Wacker, Mr. Hai Wang, Ms. Sarah Ward, Dr. Shiyi Zhang, Mr. Ryan Zentay, and Dr. Jennifer S. Zigmond, who created a friendly and safe work environment and supported my research.

The Microscopy & Imaging Center (MIC) at Texas A&M University is also gratefully acknowledged.

Lastly, I would like to thank my parents for their continued support for my graduate research. They have given me a lot of care and love, without which I could not have such an awesome life.

## CONTRIBUTORS AND FUNDING SOURCES

### **Contributors**

This work was supervised by a thesis (or) dissertation committee consisting of Professor Karen L. Wooley [advisor] of the Departments of Chemistry, Chemical Engineering, and Materials Science and Engineering; Prof. Kevin Burgess [committee member] of the Department of Chemistry; Prof. Lei Fang [committee member] of the Departments of Chemistry, and Materials Science and Engineering; and Prof. Melissa A. Grunlan [committee member] of the Departments of Biomedical Engineering, and Materials Science and Engineering.

In Chapter 2, the wide angle X-ray scattering data was collected by Dr. Joseph Reibenspies of the Department of Chemistry. Degradation studies were performed by Dr. Jiong Zou of the Department of Chemistry. The dynamic mechanical analysis was performed by Dr. Jingwei Fan of the Department of Chemistry.

In Chapter 3, the UV-Vis, infrared spectroscopy studies, thermogravimetric analyses, transmission electron microscopy studies, and dynamic mechanical analysis was performed by Dr. Jiong Zou of the Department of Chemistry. The atomic force microscope, Raman spectroscopy, confocal and differential interference contrast imaging, and emission decay studies were performed by Dr. Jeffery E. Raymond of the Department of Chemistry.

In Chapter 4, the hot-pressing was made possible with the help from Prof. Jodie L. Lutkenhaus and Dr. Dariya Reid of the Department of Chemical Engineering. I

would also like to thank Prof. Hung-Jue Sue and Dr. Peng Li of the Department of Materials Science and Engineering for access to the Agilent Digital Multimeter.

All other work conducted for the thesis was completed by the student independently.

### **Funding Sources**

For Chapter I, this work was made possible by the National Heart Lung and Blood Institute of the National Institutes of Health as a Program of Excellence in Nanotechnology (HHSN268201000046C), the National Science Foundation (DMR-130972x4 and DMR-1507429) and the Welch Foundation through the W. T. Doherty-Welch Chair in Chemistry (A-0001).

For Chapter II, this work was made possible by the National Heart Lung and Blood Institute of the National Institutes of Health as a Program of Excellence in Nanotechnology (HHSN268201000046C), the National Science Foundation under grant number DMR-1105304, and the Welch Foundation through the W. T. Doherty-Welch Chair in Chemistry (A-0001).

For Chapter III, this work was made possible by the National Heart Lung and Blood Institute of the National Institutes of Health as a Program of Excellence in Nanotechnology (HHSN26820 1000046C), the National Science Foundation under grant number DMR-1105304, and the Welch Foundation through the W. T. Doherty-Welch Chair in Chemistry, grant number A-0001.



For Chapter IV, this work was made possible by the National Science Foundation (DMR-1105304, DMR-1507429, and DMR-1309724), the National Institutes of Health (HHSN268201000046C), and the Welch Foundation (W. T. Doherty-Welch Chair, A-0001).

These contents are solely the responsibility of the authors and do not necessarily represent the official views of the National Science Foundation, National Institutes of Health, and the Welch Foundation.

## NOMENCLATURE

AFM	Atomic force microscopy
AMM	Activated monomer mechanism
ATR-FTIR	Attenuated total reflectance-Fourier transform infrared spectroscopy
CS	chitosan
CDCl <sub>3</sub>	Deuterated chloroform
$C_{\text{gel}}$	Critical gelation concentration
CVD	Chemical vapor deposition
DCM	Dichloromethane
DMA	Dynamic mechanical analysis
DMF	<i>N,N</i> -Dimethylformamide
DMSO	Dimethyl sulfoxide
DNA	Deoxyribonucleic acid
DP <sub>n</sub>	Degree of polymerization
DSC	Differential scanning calorimetry
$E'$	Storage modulus
$E''$	Loss modulus
E <sup>P2</sup>	Poly( $\gamma$ -[2-(2-methoxyethoxy)ethyl]-L-glutamate)
GPC	Gel permeation chromatography
HRP	Horseradish peroxidase

HRMS	High resolution mass spectrometry
LCST	Lower critical solution temperature
MALDI-TOF	Matrix assisted laser desorption ionization-Time of flight
$M_n$	Number-average molecular weight
NAM	Normal amine mechanism
NCA	<i>N</i> -Carboxyanhydride
NIR	Near-infrared
NMR	Nuclear magnetic resonance spectroscopy
ODLAG	Oligo(DL-allylglycine)
OEG	Oligo(ethylene glycol)
OPG	Oligo(propylene glycol)
PA	Poly(alanine)
PAF	Poly(alanine- <i>co</i> -phenyl alanine)
PBLG	Poly( $\gamma$ -Benzyl-L-glutamate)
PDLAG	Poly(DL-allylglycine)
PDMS	Polydimethylsiloxane
PEG	Poly(ethylene glycol)
PFS	Poly(ferrocenylsilane)
PLG	Poly(L-glutamic acid)
PPLG	Poly( $\gamma$ -Propargyl-L-glutamate)
PPO	Poly(propylene oxide)
PS	Polystyrene

PTA	Phosphotungstic acid
ROP	Ring-opening polymerization
$R_s$	Sheet resistance
r.t.	Room temperature
SEM	Scanning electron microscopy
SWCNT	Single-walled carbon nanotube
TEM	Transmission electron microscopy
TA	Tyramine
$T_c$	Crystallization temperature
TCSPC	Time correlated single-photon counting
TFA	Trifluoroacetic acid
TFA-d	Deuterated trifluoroacetic acid
$T_g$	Glass transition temperature
$T_{gel}$	Sol-gel transition temperature
TGA	Thermogravimetric analysis
THF	Tetrahydrofuran
$T_m$	Melting temperature
UV/Vis	Ultraviolet visible spectroscopy
WAXS	Wide-angle X-ray scattering

## TABLE OF CONTENTS

	Page
ABSTRACT .....	ii
DEDICATION .....	iv
ACKNOWLEDGEMENTS .....	v
CONTRIBUTORS AND FUNDING SOURCES .....	vii
NOMENCLATURE .....	x
TABLE OF CONTENTS .....	xiii
LIST OF FIGURES .....	xv
LIST OF TABLES .....	xix
CHAPTER I INTRODUCTION .....	1
1.1 Synthetic polypeptides as stimuli-responsive gelators .....	1
1.2 Synthesis of polypeptides through NCA ROP .....	3
1.3 Polypeptide gelation mechanisms .....	6
1.4 Types of stimuli-responsive sol-gel transitions for polypeptide gelators .....	9
1.5 Scope of the thesis .....	19
CHAPTER II MULTI-RESPONSIVE HYDROGELS DERIVED FROM THE SELF- ASSEMBLY OF TETHERED ALLYL-FUNCTIONALIZED RACEMIC OLIGOPEPTIDES .....	23
2.1 Introduction .....	23
2.2 Experimental section .....	26
2.3 Results and discussions .....	30
2.4 Conclusions .....	44
CHAPTER III SUPRAMOLECULARLY-KNITTED TETHERED OLIGOPEPTIDE/SINGLE-WALLED CARBON NANOTUBE ORGANOGELS .....	45
3.1 Introduction .....	45
3.2 Experimental section .....	49
3.3 Results and discussions .....	54

	Page
3.4 Conclusions .....	69
CHAPTER IV REVERSIBLE PHOTO-PATTERNING OF SOFT CONDUCTIVE MATERIALS VIA SPATIALLY-DEFINED SUPRAMOLECULAR ASSEMBLY ..... 71	
4.1 Introduction .....	71
4.2 Experimental section .....	72
4.3 Results and discussions .....	77
4.4 Conclusions .....	94
CHAPTER V CONCLUSIONS .....	95
REFERENCES .....	102

## LIST OF FIGURES

	Page
Figure 1.1. NAM and AMM pathways for ring-opening polymerizations of NCAs.....	4
Figure 1.2. NCA ROP under N <sub>2</sub> flow <i>via</i> Normal Amine Mechanism. Adapted from ref. 57. Copyright 2013 American Chemical Society.....	5
Figure 1.3. Schematic illustrations of polypeptide gelation mechanisms <i>via</i> fibrillar entanglement, micellar percolation and chemical crosslinking. ....	8
Figure 2.1. Synthesis of ODLAG <sub>6</sub> - <i>b</i> -PEG <sub>68</sub> - <i>b</i> -ODLAG <sub>6</sub> .....	31
Figure 2.2. <sup>1</sup> H NMR spectrum of ODLAG <sub>6</sub> - <i>b</i> -PEG <sub>68</sub> - <i>b</i> -ODLAG <sub>6</sub> .....	33
Figure 2.3. MALDI-TOF mass spectrum of ODLAG <sub>6</sub> - <i>b</i> -PEG <sub>68</sub> - <i>b</i> -ODLAG <sub>6</sub> . ....	33
Figure 2.4. <i>T</i> <sub>gel</sub> of ODLAG <sub>6</sub> - <i>b</i> -PEG <sub>68</sub> - <i>b</i> -ODLAG <sub>6</sub> as a function of concentration. ....	35
Figure 2.5. Storage and loss moduli of ODLAG <sub>6</sub> - <i>b</i> -PEG <sub>68</sub> - <i>b</i> -ODLAG <sub>6</sub> hydrogel (5 wt%) as a function of frequency conducted by DMA at room temperature.....	36
Figure 2.6. Tan (δ) of ODLAG <sub>6</sub> - <i>b</i> -PEG <sub>68</sub> - <i>b</i> -ODLAG <sub>6</sub> hydrogel (5 wt%) as a function of frequency conducted by DMA at room temperature. ....	36
Figure 2.7. ATR-FTIR spectrum of a dried hydrogel made from ODLAG <sub>6</sub> - <i>b</i> -PEG <sub>68</sub> - <i>b</i> - ODLAG <sub>6</sub> . ....	37
Figure 2.8. WAXS pattern of a dried ODLAG <sub>6</sub> - <i>b</i> -PEG <sub>68</sub> - <i>b</i> -ODLAG <sub>6</sub> hydrogel. ....	38
Figure 2.9. (a) DSC trace of ODLAG <sub>6</sub> - <i>b</i> -PEG <sub>68</sub> - <i>b</i> -ODLAG <sub>6</sub> in the solid state. The samples were heated from -100 °C to 200 °C and cooled back to -100 °C with both heating and cooling rates of 10 °C/min. The third heating and cooling traces were shown here. (b) DSC trace of ODLAG <sub>6</sub> - <i>b</i> -PEG <sub>68</sub> - <i>b</i> - ODLAG <sub>6</sub> in the solid state, after rapid cooling above the <i>T</i> <sub>m</sub> . The sample was removed from the DSC at 125 °C, immersed into liquid nitrogen and returned into the DSC during the second cycle. The third heating and cooling traces are shown here. ....	38
Figure 2.10. TEM images of a ODLAG <sub>6</sub> - <i>b</i> -PEG <sub>68</sub> - <i>b</i> -ODLAG <sub>6</sub> hydrogel. ....	39
Figure 2.11. SEM images of a ODLAG <sub>6</sub> - <i>b</i> -PEG <sub>68</sub> - <i>b</i> -ODLAG <sub>6</sub> hydrogel. ....	40
Figure 2.12. An illustrative scheme for the formation of nanofibers and hydrogels formed from self-assembly of ODLAG <sub>6</sub> - <i>b</i> -PEG <sub>68</sub> - <i>b</i> -ODLAG <sub>6</sub> . ....	41

Figure 2.13. (a) Digital photographs showing responsiveness of ODLAG <sub>6</sub> - <i>b</i> -PEG <sub>68</sub> - <i>b</i> -ODLAG <sub>6</sub> hydrogels towards different stimuli. (b) TEM image of a ODLAG <sub>6</sub> - <i>b</i> -PEG <sub>68</sub> - <i>b</i> -ODLAG <sub>6</sub> sol. ....	42
Figure 2.14. Weight loss profile of ODLAG <sub>6</sub> - <i>b</i> -PEG <sub>68</sub> - <i>b</i> -ODLAG <sub>6</sub> hydrogel with/without enzyme. Measurements were repeated five times for each enzyme and control sample. ....	43
Figure 3.1. Graphic illustration of ODLAG <sub>6</sub> - <i>b</i> -PEG <sub>68</sub> - <i>b</i> -ODLAG <sub>6</sub> based organogels with/without SWCNT incorporation. ....	54
Figure 3.2. a) UV-vis spectra of SWCNT in DMF with 1 (black); SWCNT in DMF with NH <sub>2</sub> -PEG <sub>68</sub> -NH <sub>2</sub> (green), 1 in DMF (blue), SWCNT in DMF without 1 (red) and NH <sub>2</sub> -PEG <sub>68</sub> -NH <sub>2</sub> in DMF (pink); b) Images of SWCNT in DMF with/without 1. ....	58
Figure 3.3. TEM images of a) hierarchical assembly of 1-SWCNT composites in SWCNT organogel without staining; b) SWCNT; c) 1 DMF organogel with PTA stain; d) 1 DMF organogel without staining. ....	59
Figure 3.4. TEM images of hierarchically-assembled structures in 1-SWCNT composites. ....	61
Figure 3.5. SEM image of lyophilized 1-SWCNT DMF gels. ....	62
Figure 3.6. AFM images of a) height image of SWCNT after deposition onto freshly-cleaved mica from a solution in DMF and drying <i>in vacuo</i> ; b) height image of 1-SWCNT composite after spin coating onto mica from the DMF gel state and drying <i>in vacuo</i> ; c) height image of 1 after spin coating onto mica from the DMF gel state and drying <i>in vacuo</i> ; d) phase image of the sample from c). ....	62
Figure 3.7. Confocal and differential interference contrast imaging of a) triblock 1 DMF gel; b) 1-SWCNT DMF gel; c) SWCNTs in DMF; d) DMF 5,6-FAM dye solution. ....	63
Figure 3.8. Emission decay profiles for 5,6-FAM dye in the presence of DMF (left, black), SWCNT DMF (left, red), 1 DMF gel (right, black), 1-SWCNT DMF gel (right, red). ....	64
Figure 3.9. FT-IR spectra of dried 1, 1-SWCNT composites and SWCNT. ....	65



Figure 3.10. Expanded amide region from FT-IR spectra of dried 1, 1-SWCNT composites and SWCNT.....	66
Figure 3.11. Raman spectra of triblock 1 DMF gel (50 mg/mL, red line), 1-SWCNT gel (50 mg/mL polymer with 2 wt% SWCNT loading, blue line), SWCNT in DMF suspension (pink line), 1-SWCNT solution (5 mg/mL polymer with 2 wt% SWCNT loading, green line).....	67
Figure 3.12. TGA measurements of dried 1, 1-SWCNT composites and SWCNT.....	68
Figure 3.13. (a) Moduli of organogels from ODLAG <sub>6</sub> -PEG <sub>68</sub> -ODLAG <sub>6</sub> SWCNT gel (50 mg/mL, with 1.5 wt% SWCNT incorporation) as a function of frequency conducted by DMA. $E'$ and $E''$ indicate storage and loss modulus, respectively. ....	69
Figure 4.1. <sup>1</sup> H NMR of (a) DLAG-NCA monomer and (b) PEG- <i>b</i> -PDLAG block copolymer. ....	76
Figure 4.2. Synthetic route for PEG- <i>b</i> -PDLAG block copolymer. ....	78
Figure 4.3. (a) Stimuli-responsive reversible sol-gel transitions of PEG- <i>b</i> -PDLAG block copolymer in water. (b) Change of $T_{gel}$ as a function of polymer concentration for a series of PEG- <i>b</i> -PDLAG, having consistent PEG chain length and variation of the PDLAG chain lengths.....	79
Figure 4.4. (a) Illustrative formation of $\beta$ sheets as constructive units of nanofibrils. (b) Relationships between the functions of the PEG- <i>b</i> -PDLAG and SWCNT composite components.....	80
Figure 4.5. Images of SWCNTs in H <sub>2</sub> O without (upper images) and with polymer (lower images), correlated with various time points after sonication (1 mg/mL SWCNTs, 0 or 10 mg/mL polymer). ....	82
Figure 4.6. UV/vis spectra of assorted systems (with 0.05 mg/mL SWCNTs, 1 mg/mL polymer, if applicable).....	82
Figure 4.7. TEM images of (a) SWCNT sol and (b) PEG- <i>b</i> -PDLAG/SWCNT composite sol, without staining. SEM images of aerogels of (c) 5 wt% PEG- <i>b</i> -PDLAG and (d) 5 wt% PEG- <i>b</i> -PDLAG/0.5 wt% SWCNT composite. ....	83
Figure 4.8. Incorporation of SWCNTs increased the thermal responsive sensitivity of the composite gel materials. ....	84

Figure 4.9. Moduli of PEG- <i>b</i> -PDLAG/SWCNT hydrogels as a function of frequency conducted by DMA ( $E'$ and $E''$ indicate storage and loss modulus, respectively).....	85
Figure 4.10. IR spectra of polymer/SWCNT aerogel, polymer aerogel, and SWCNTs. .	86
Figure 4.11. (a) Reversible stimuli-responsive sol-gel transitions of the composite material having 5 wt% PEG- <i>b</i> -PDLAG and 0.5 wt% SWCNT. TEM images of (b) PEG- <i>b</i> -PDLAG/SWCNT composite sol, (c) PEG- <i>b</i> -PDLAG/SWCNT composite gel, (d) PEG- <i>b</i> -PDLAG gel, and (e) SWCNT sol, with phosphotungstic acid stain. For each TEM image, the sample concentrations were at 1 mg/mL PEG- <i>b</i> -PDLAG and 0.1 mg/mL SWCNT, if applicable. ....	87
Figure 4.12. Schematic illustration of a PEG- <i>b</i> -PDLAG/SWCNT dispersion, and reversible conversion of polymeric supramolecular structures that correlates to the formation or break-down of gel matrix in response to a stimulus. ....	89
Figure 4.13. Schematic illustration of the reversible photo-patterning process for production of soft electronics. ....	90
Figure 4.14. Electrical conductivity of composite films (PEG <sub>45</sub> - <i>b</i> -PDLAG <sub>28</sub> /SWCNT) as a function of percentage SWCNT incorporation.....	91
Figure 4.15. Raman spectrum of SWCNTs in solid form. ....	91
Figure 4.16. Conductivities of films composed of 15 wt% of SWCNTs and 85 wt% of PEG <sub>45</sub> - <i>b</i> -PDLAG <sub>28</sub> . One recycle process involves resuspension of the composite into water with sonication, responsive sol-to-gel transition, and film formation through air dry. ....	92
Figure 4.17. A printed free standing thin film fabricated into a Möbius strip. ....	92
Figure 4.18. Linear fitted I-V curves of composite films with various percentage of SWCNT incorporation. Each spot was generated by measuring conductivity at a different location. ....	93

## LIST OF TABLES

	Page
Table 2.1. Synthesis and hydrogelation capabilities of ODLAG- <i>b</i> -PEG- <i>b</i> -ODLAG with different lengths of ODLAG blocks .....	31
Table 2.2. Solubility studies of ODLAG <sub>6</sub> - <i>b</i> -PEG <sub>68</sub> - <i>b</i> -ODLAG <sub>6</sub> in different organic solvents. ....	34
Table 3.1. Solubility studies of SWCNT, ODLAG <sub>6</sub> -PEG <sub>68</sub> -ODLAG <sub>6</sub> (1) and 1-SWCNT composites in different organic solvents. ....	56
Table 3.2. Critical gelation concentrations ( $C_{gel}$ ) of ODLAG <sub>6</sub> -PEG <sub>68</sub> -ODLAG <sub>6</sub> (1) and 1-SWCNT composites in different organic solvents. ....	57
Table 4.1. Sheet resistance, thickness, and electrical conductivity of composite films as a function of percentage of SWCNT incorporation. ....	94

## CHAPTER I

### INTRODUCTION\*

#### 1.1 Synthetic polypeptides as stimuli-responsive gelators

Smart gels contain medium (typically liquid) in a matrix of physically- and/or covalently-crosslinked solid network, and show controllable chemical structure changes or physical property variations *via* treatment with certain stimuli, which include but are not limited to changes of environmental factors (temperature, mechanical force), exposure of electromagnetic fields (light, magnetic field), and subjection of (bio)chemical species (protein, acid/base, redox agent).<sup>1-3</sup> A highly attractive feature of most gel materials is that they require only a small fraction of gelators to promote molecular-to-macroscopic amplifications in response to a stimulus. In the last two decades, significant efforts have been devoted to the research of smart gels due to their capability to respond to stimuli rapidly, the versatility to assemble into specific nano- and/or microstructures in various environments, and the ability to exhibit changes in macroscopic characteristics, such as switches between liquid and gel states, also named sol-gel phase transitions.<sup>4,5</sup> Gels with stimuli-triggered sol-gel transitions, through construction and deconstruction of the gel networks by either covalent or non-covalent interactions, have found extensive applications in controlled drug release,<sup>6-10</sup> tissue engineering,<sup>11,12</sup> selective sensing,<sup>13,14</sup> and photolithography fields.<sup>15</sup> The drastic

---

\* Reprinted (adapted) with the permission from “Stimuli-triggered Sol-Gel Transitions of Polypeptide Gels Derived from N-carboxyanhydride (NCA) Polymerizations” by He, X.; Fan, J.; Wooley, K. L., *Chem. Asian J.* **2016**, *11*, 437-447. Copyright 2016 Wiley-VCH.

difference of the physical properties between sol and gel states, and the rapid switch of sol-gel transitions have rendered smart gels as potential materials for applications that require both sol and gel type behaviors during different stages of operation.<sup>16</sup> The stimuli-triggered sol-gel transition process enables the localization and breakdown of the soft gelation materials with spatial and temporal precision, which is of great significance for controlled material fabrication, implantation and degradation.

Among the smart stimuli-responsive gelators, synthetic polypeptides are of great interest toward biomedical applications due to their innate biocompatibility and biodegradability, and have been widely investigated for their gelation mechanisms and responsive sol-gel transition behaviors owing to the following reasons.<sup>17</sup> Firstly, compared with conventional solid-phase peptide synthesis, ring-opening polymerization (ROP) of *N*-carboxyanhydrides (NCAs) has provided a more practical synthetic approach to prepare well-defined polypeptides in scalable quantities with controllable polymerization rates, predictable molecular weights, narrow molecular weight distributions and unchanged amino acid chirality.<sup>18,19</sup> In addition, depending on the side chain moieties, polypeptides can adopt unique ordered conformations, including  $\alpha$ -helix and  $\beta$ -sheet, which can be controlled *via* molecular design and tuned through triggers from external stimuli, with correlations between the conformational switch of secondary structures and the sol-gel phase transition.<sup>20-22</sup> Moreover, side chain functionalities with diverse responsive components can be readily incorporated onto polypeptides, contributing to the exceptional versatility of natural and synthetic side-chain-

functionalized monomer species and highly efficient orthogonal functionalization techniques, for pre- and post-polymerization modifications, respectively.<sup>23-27</sup>

Recently, a number of reviews have been published with focus on the subjects of synthetic methodologies, stimuli-responsive properties and biomedical applications of polypeptide-based materials.<sup>19,20,23,28-31</sup> In this introduction chapter, the most recent advances of synthetic approaches for NCA ROPs are briefly captured; followed by highlights and descriptions of diverse gelation mechanisms and categories of stimuli-triggered sol-gel transitions, with an aim to provide a tutorial in the chemical composition, supramolecular structure and responsive property relationships for rational design of polypeptide gel materials.

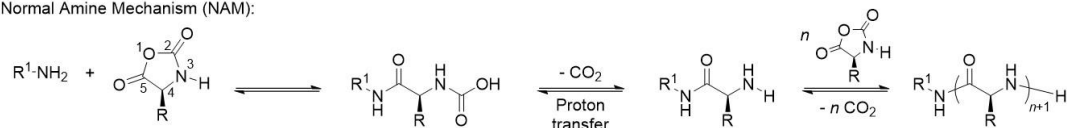
## **1.2 Synthesis of polypeptides through NCA ROP**

Amino acid NCAs have been studied for over 100 years, since the first report by Leuchs and co-workers in 1906.<sup>32-34</sup> In comparison with conventional solid-phase peptide synthesis, the ROP of NCAs is a more economical and practical synthetic approach for the preparation of polypeptides and peptide hybrid polymeric materials, especially for the synthesis of polypeptides having over 100 repeat units.<sup>18,29,30,35-37</sup> NCA ROP can be initiated by a range of nucleophiles and bases. Depending on the initiators used in the polymerization, two widely accepted pathways of NCA polymerizations are “normal amine mechanism” (NAM) and “activated monomer mechanism” (AMM) (Figure 1.1).<sup>30,35</sup> In NAM, the polymerization is generally initiated by nonionic initiators, which exhibit more nucleophilicity than basicity, such as primary amines, alcohols and water. During the polymerization, the initiator acts as the

nucleophile to attack the carbonyl group at 5-C to open the ring structure of the NCA monomer. After the release of CO<sub>2</sub>, the reproduced amine chain end will continue to serve as a nucleophile to attack the carbonyl group of another NCA monomer to propagate the polymer growth. In contrast, AMM involves the initiator acting as a base rather than as a nucleophile, which deprotonates the nitrogen (3-N) in the NCA monomer, resulting in the formation of a corresponding anion. This anion then acts as a nucleophile to attack the carbonyl group at 5-C of another NCA monomer, leading to ring-opening and further chain propagation in the same manner as in NAM. Due to the relatively slower initiation step in comparison with the propagation in AMM, polymerizations following the AMM pathway commonly yield less controlled and ill-defined polypeptides.<sup>35</sup> Of course, these two mechanistic treatments are at extremes, with all processes involving equilibria and each in competition.

Due to the coexistence of these two polymerization pathways during NCA ROPs, it is often problematic to synthesize high molecular weight polypeptides with controlled

Normal Amine Mechanism (NAM):



Activated Monomer Mechanism (AMM):

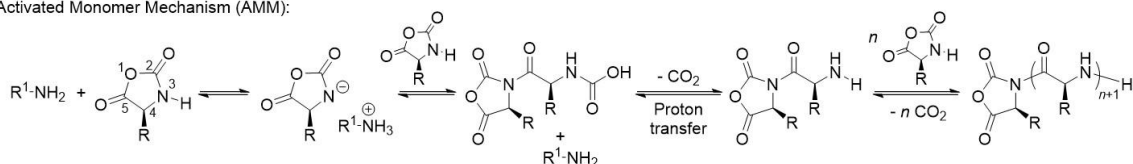


**Figure 1.1.** NAM and AMM pathways for ring-opening polymerizations of NCAs.





### 1.3 Polypeptide gelation mechanisms

The formation of crosslinking sites by either physical interactions or chemical crosslinkers is one of the most important factors for the creation of three-dimensional networks to entrap organic solvents or aqueous media in a gel.<sup>58-61</sup> Commonly, physical crosslinking interactions include relatively strong supramolecular interactions, such as hydrogen-bonding, hydrophobic interactions,  $\pi$ - $\pi$  stacking, host-guest interactions and metal-ligand interactions.<sup>62-64</sup> For example, driven by inter- and intramolecular hydrogen-bonding interactions, polypeptides can supramolecularly assemble into nanofibril and/or nanoribbon structures with one-dimensional stacking of polymers or polymer aggregations, including  $\alpha$ -helical and  $\beta$ -sheet secondary structures.<sup>7,49,65-69</sup> Stimuli-triggered construction of the nanostructures in polypeptide materials, or change of the conformations between secondary structures, would result in gel formation. Another vital factor to consider for gelation is the solvophilic-solvophobic balance. Due to the nano- and/or microphase separation derived from supramolecular assembly of polypeptides, a delicate solvophilic-solvophobic balance should be achieved in polypeptide-based gels. Interactions that are strong enough to break this balance would cause either gel breaking into viscous liquid or polymer precipitation.

For polypeptide-based gelators that contain at least one polypeptide block segment, secondary structures are considered as one of the remarkable driving forces for gelation. In order to construct supramolecularly assembled gels, the alignment of secondary structures, including  $\alpha$ -helices and  $\beta$ -sheets, into one-dimensional nanofibril or nanoribbon structures have been investigated widely, together with incorporation of

another block segment, commonly adopting random coil conformations, to increase the solubility of supramolecular assemblies and balance the solvophilic-solvophobic interactions (Figure 1.3 a)<sup>65,67-69</sup> For example, Kim et al. reported poly(ferrocenylsilane)-*block*-poly( $\gamma$ -benzyl-L-glutamate) (PFS-*b*-PBLG) as an organogelator in toluene, originating from the monolayer one-dimensional stacking of the  $\alpha$ -helical polypeptide segments (PBLG) into nanoribbons, driven by the dipolar  $\pi$ - $\pi$  stacking of phenyl groups on the side chains of PBLG, which further entangled physically to construct networks for gelation.<sup>65</sup> The PFS block segment could be replaced by polystyrene (PS) and poly(ethylene glycol) (PEG) and similar gelation processes were observed, resulting from the high solubility of all three polymers in toluene when possessing random coil conformations. Due to the significant roles of secondary structures in the gelation process of polypeptide-based materials, the gelation property can be readily tuned by control over the secondary structures *via* structural modifications, such as tuning stereochemistry of polypeptides, varying block lengths of solvophilic and solvophobic segments, and introducing other moieties that are capable of hydrogen-bonding or other supramolecular interactions into the gelation systems. Compared with polypeptides derived from L-amino acids, polypeptides from *rac*-amino acids typically could not undergo gelation or required much higher concentrations for gelation.<sup>70,71</sup> In the range of the suitable solvophilic-solvophobic balance, longer solvophobic segments would induce stronger interactions in the nano- and/or microphase domains, which enhanced the gel-forming ability and gel strength.<sup>72,73</sup> In 2011, Jang *et al.* reported a poly(ethylene glycol)-*block*-poly(alanine)-*graft*-chitosan (PEG-*b*-PA-*g*-

CS) with extensive intermolecular hydrogen-bonding from the protonation of chitosan at an acidic environment to improve gel-forming ability.<sup>74,75</sup>

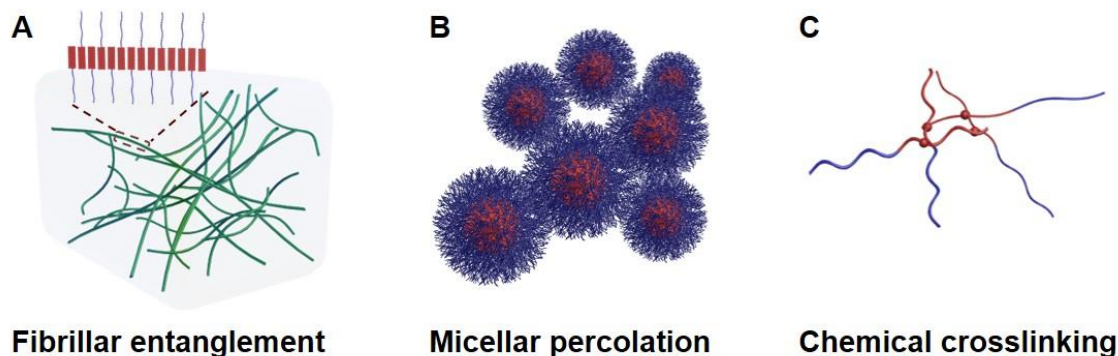


**Figure 1.3.** Schematic illustrations of polypeptide gelation mechanisms *via* fibrillar entanglement, micellar percolation and chemical crosslinking.

In the last decade, several groups have reported reverse thermal gelation from PEG-*block*-polypeptide diblock copolymers, which underwent a thermally-induced sol-to-gel transition with an increase of the temperature.<sup>7,76-80</sup> Depending on the secondary structures formed in the polypeptide segment domains, two gelation mechanisms were proposed for this reverse thermal gelation. For polypeptides with  $\beta$ -sheets dominating the secondary structure populations, the polypeptide block segments assembled supramolecularly into nanofibril or nanoribbon structures from one-dimensional stacking of polypeptides, while PEG possessed random coil conformations in aqueous solution.<sup>76,79</sup> With an increase of temperature, dehydration of PEG altered the hydrophilic-hydrophobic balance toward the hydrophobic direction. At the same time,

the hydrophobic core was stabilized by strengthening the secondary structures from the polypeptides due to a smaller packing distance from the shrinking of PEG. Also, dehydration of the PEG block upon an increase of the temperature enhanced the physical crosslinking between the hydrophobic domains *via* stronger hydrophobic interactions. Further increased temperature (*ca.* 60 °C) shifted the hydrophilic-hydrophobic balance out of the gelation range, resulting in precipitation of polymer from the mixtures. On the other side, for polymers with more  $\alpha$ -helical components in the polypeptide domains, micellar structures were often observed for amphiphilic block copolymers, in which the polypeptides assembled into the core and PEG constructed the shell domain.<sup>70,80</sup> With an increase of the temperature, dehydration of the PEG enhanced the hydrophobic interactions, and led to aggregation and close packing of micelles for the creation of percolating gel networks (Figure 1.3 b).<sup>81,82</sup>

In addition to the above mechanisms that relate to the formation of physically-crosslinked nanofibril/nanoribbons or aggregated micelles, chemical crosslinkings between functional side chains of polypeptides enable gel formation and also introduce novel stimuli-responsive properties, including photo, pH and redox, which will be discussed in the next section (Figure 1.3 c).

## **1.4 Types of stimuli-responsive sol-gel transitions for polypeptide gelators**

### *1.4.1 Unique responsive behaviors by assembly or hydrolysis of polypeptides*

Unique to the polypeptide-based gelator systems are the sol-gel transitions resulting from assembly or disassembly of polypeptide domains due to changes in interactions between their secondary structures, and/or degradation of the backbones

resulting from the hydrolysis of amide bonds upon treatment with enzymes. These assembly and degradation behaviors were commonly correlated to the stimuli, including change of temperature, exposure of mechanical force, and treatment with enzymes, which will be discussed in the beginning of this section.

#### **1.4.1.1 Heat-induced gel-to-sol transition**

Gel-to-sol transitions due to an increase of temperature have been observed extensively in gelators derived from natural or artificial proteins. For this type of responsive phase transition, a renowned natural protein example is gelatin, which is commonly used as a gelling agent in the food industry. The hydrogelation mechanism of gelatin may be attributed to physical network formation resulting from the coil-to-helix transition of protein chains in response to a decrease of temperature.<sup>83</sup> In terms of artificial proteins, a notable example are the proteins that contain leucine zipper domains, which may create hydrophobic interhelical interfaces that strengthen the interchain interactions.<sup>84</sup>

For polypeptide-derived gelators synthesized by NCA ROP, one of the most popular components is PBLG because of its capability to adopt a rigid  $\alpha$ -helical conformation. This stiff conformation showed unique solution behavior, such as nematic liquid crystalline ordering, which contributed to the thermoreversible gelation of PBLG-containing gelators in  $\alpha$ -helicogenic solvents (*e.g.* toluene and benzyl alcohol).<sup>85,86</sup> For example, in 2012, the Mezzenga group reported a triblock copolymer, PBLG-*block*-polydimethylsiloxane-*block*-PBLG (PBLG-*b*-PDMS-*b*-PBLG), which displayed thermo-induced gel-to-sol behavior in toluene.<sup>87</sup> The rods (derived from the

$\alpha$ -helical PBLG components) and the coils (derived from PDMS domains) assembled into nanofibrils with the rods densely packed in the center of the fibrils, of which the thickness was tunable through control of the PBLG block length. Since identical Fourier transform infrared (FTIR) spectra were collected at 25 °C (gel state) and 50 °C (sol state), the reason for heat-induced gel-to-sol transition was assigned to an increased solubility of the PBLG block in toluene at higher temperature.

Thermo-induced reversible gel-to-sol transition was also observed in polypeptide gelators that formed  $\beta$ -sheets. In 2013, Wooley's group reported a series of PEG-*block*-poly(DL-allylglycine) (PEG-*b*-PDLAG) organogels, of which the organogelation was proposed to result from the supramolecular assembly of the peptide blocks into  $\beta$ -sheet-driven polymeric ribbons in a monolayer fashion.<sup>68</sup> Gel melting was observed when the temperature was increased to the sol-gel transition temperature ( $T_{gel}$ ), which was tunable by varying the polymer block lengths or solvents, while transparent gel recovery was achieved after several hours at room temperature. This gelator displayed ultra-low (*ca.* 0.1 wt%) critical gelation concentration ( $C_{gel}$ ) in DMF, DMSO and methanol, even though the peptide domains were constructed from racemic monomers.

#### **1.4.1.2 Thermo-reversed gelation**

An aqueous system that undergoes sol-to-gel transition as the temperature increases is defined as a thermo-reversed gelation system, which has attracted intense interests for the potential to deliver therapeutic molecules locally *via* a minimally invasive administration. Due to the capability of tuning the gelation temperature close to human physiological temperature, great attention has been attracted to apply this reverse

thermal gelation toward injectable biomedical applications. By this approach, it is expected that drugs or cells can be mixed into the polymer aqueous solutions at lower temperature, such as room temperature. After being injected into the targeted site, the increase of temperature (for example, the change to human physiological temperature, 37 °C) triggers the gel formation and promotes the cohesion of the mixture, which can act as a drug release system or a cell growing matrix.

From a synthetic standpoint, one popular design of a thermo-reversed hydrogelator is to construct a hybrid PEG-*b*-peptide copolymer, for which the PEG block dehydrates and the peptide block displays increased  $\beta$ -sheet content, with increase of temperature. For instance, in 2008 and 2009, the Jeong group reported the incorporation of PEG, oligo(propylene glycol) (OPG) and oligopeptides into a series of multiblock amphiphilic hydrogelators, in which the two end-capped oligopeptide blocks were composed of oligo(alanine) or statistical oligopeptides of alanine and phenylalanine.<sup>71,72</sup> As heat was applied to these polymer sols, the secondary structures of two oligopeptide end blocks changed from random coils to  $\beta$ -sheets, as confirmed by circular dichroism (CD) spectra; while the central PEG and OPG block dehydrated. Both of the heat-induced formation of  $\beta$ -sheets and block dehydration were anticipated to reinforce the interactions of the amphiphilic polymers to form a percolating network, resulting in gelation over macroscale dimensions.

Analogous to the design from the Jeong group, more PEG-*b*- $\beta$ -sheet peptides with thermo-reversed gelation behaviors and mechanisms were reported by the Heise,<sup>76</sup> Chen,<sup>77</sup> Li,<sup>78</sup> and Wooley groups.<sup>79</sup> As an illustration, for the oligo(DL-allylglycine)-

*block*-PEG-*block*-oligo(DL-allylglycine) (ODLAG-*b*-PEG-*b*-ODLAG) triblock structure synthesized in the Wooley group, the reversible macroscopic sol-to-gel transitions were correlated with the transformation of nanostructural morphologies, with spherical aggregates observed in the sol state and fibrillar structures in the gel state, respectively. Upon heating, the spherical aggregates re-assembled into fibrils, which were hypothesized to be composed of hydrophobic  $\beta$ -sheeting cores and hydrophilic PEG that protruded to increase the solubility. The entanglement, crystallinity, and cross-linking of these fibrils were assumed to create a physical network that constituted the hydrogel matrix.

To further understand the effect of control over structure of the thermo-reversed gelators related to  $\beta$ -sheet formation, detailed studies on the relationship between the chemical compositions and the gelation behaviors were conducted. For example, in order to tune the  $T_{\text{gel}}$ , synthetic approaches including control of the block length,<sup>77</sup> modification of the chain end groups,<sup>88</sup> and change of the hydrophobic alkyl side chain length were investigated.<sup>89</sup>

Apart from  $\beta$ -sheet-rich systems, heat-induced gelation was also described in polypeptide gelators that adopted considerable amounts of  $\alpha$ -helical conformation. Recently, Deming's group designed a coil-helical structure, in which the coil was made of highly water-soluble racemic polypeptide, and the helix was derived from helicogenic polypeptides that contained poly( $\gamma$ -[2-(2-methoxyethoxy)ethyl]-L-glutamate) ( $E^{\text{P2}}$ ).<sup>90</sup> The thermo-responsive gelation phenomenon may be attributed to the lower critical solution temperature (LCST) behavior of the  $E^{\text{P2}}$  domains, of which the peptide side



chains were functionalized with oligo(ethylene glycol) (OEG).<sup>91</sup> In addition, other  $\alpha$ -helix-rich thermo-reversed gelators were also reported, with the responsive gelation driving forces related to the dehydration of poloxamer,<sup>92</sup> and the  $T_{\text{gel}}$  tunable through coordination of metals.<sup>93</sup>

In addition to hydrogelation, thermo-reversed organogelation was also reported by the Jeong group for a PEG-*block*-polypeptide copolymer in chloroform.<sup>80</sup> At low temperature, this polymer assembled into micelles, which might aggregate upon increase of temperature, resulting in the organogelation of the system. The organogelation due to intermicellar aggregation was attributed to the decreased hydrodynamic radius of PEG, which was characterized by the measurement of intrinsic viscosity.

#### **1.4.1.3 Mechanical force**

Sonication typically refers to a process by which ultrasound waves are applied to generate cavitation (formation, growth, oscillation, and collapse of bubbles) in a pressure field.<sup>94</sup> Since 2005, there have been extensive studies on the sol-gel transitions of soft matter when ultrasound is applied.<sup>95-97</sup> Nevertheless, most of the existing sonication-induced sol-gel transition studies were based on the self-assembly and reorganization of small molecules, while the polymeric systems were less explored.<sup>98</sup>

Recently, the Wooley group described sonication-triggered gel-to-gel transitions in the cases of  $\alpha$ -helix-rich organogel systems, while gel-to-sol transitions were observed in  $\beta$ -sheet-rich systems.<sup>99</sup> For the PEG-*block*-statistical polypeptides that had higher  $\alpha$ -helical content, immediate reassembly of short nano-rods with maintenance of long-range interactions, in situ after sonication, facilitated the rebuilding of three-dimensional

networks and resulted in sonication-triggered gel-to-gel transitions. On the other hand, in similar systems with higher  $\beta$ -sheet content, the longer nanofibrils were expressly converted into short nanorods, which were well-aligned in nanodomains, but lacked longer range connectivity between clusters, ultimately resulting in gel-to-sol transitions.

Another sonication-triggered gel-to-sol transition system, consisted of  $\beta$ -sheet-rich ODALG-*b*-PEG-*b*-ODLAG gelator, was also reported by the Wooley group.<sup>68,79,100</sup> Disruption of nanofibrils with long-range interactions into discrete spherical aggregates was observed when sonication was applied, ultimately resulting in a gel-to-sol transition. Based on the above two studies, the effect on the external sonication-responsive property due to secondary structural control of polypeptide-based gels provides a novel and facile method to modify the properties of stimuli-responsive materials by tuning the self-assembled nano- or micro-structures without the need of precise control on the molecular level.

#### **1.4.1.4 Enzyme**

Owing to the presence of enzyme-cleavable amide bonds linking the amino acid repeat units along the backbone, polypeptide-based hydrogels have exhibited responsive degradation when treated with enzymes. The degradation of polypeptide hydrogels was studied both *in vitro* and *in vivo*, in order to investigate the potential applications such as enzyme-controlled release of encapsulated cargoes, desert-greening and agricultural materials.<sup>79,92,101</sup>

In these studies, the hydrogel degradation profile was found to be dependent on the structure of the peptide units and the type of enzymes chosen, as polypeptides

showed various susceptibilities towards an enzyme and enzymes also showed different efficiencies in degrading a polypeptide chain. As an example, the Jeong group reported an enzymatically-degradable temperature-sensitive polypeptide, poly(ethylene glycol)-*block*-poly(alanine-*co*-phenyl alanine) (PEG-PAF), of which the sol underwent gelation in situ upon injection.<sup>101</sup> The gel was comparably stable in phosphate buffered saline while it degraded much faster in the subcutaneous layer of rats. The degradation was assumed to occur in the presence of proteolytic enzymes and was confirmed by gel permeation chromatography. In this study, various enzymes were tested and different degradation rates were observed. Another example of an enzyme-triggered gel-to-sol transition was described by the Wooley group.<sup>79</sup> In this study, the enzyme-responsiveness of the hydrogel system was observed by studying in vitro hydrogel weight loss profiles. Through comparison of the rate of weight loss, the efficiencies of different enzymes on triggering gel-to-sol transitions of the hydrogels were able to be compared. In addition, Yamamoto and coworkers observed the suppression of hydrolysis and break down of the gel matrix by incorporating unnatural amino acids into the polypeptide backbone, when the hydrogels were incubated with proteases or microorganisms that secreted hydrolytic enzymes.<sup>102</sup> The observation of these phenomena is fortunate, as it allows the optimization of the degradation profile through synthetic approaches. Unfortunately, however, enzymatic cleavage of the backbone has to this point resulted in irreversible gel-to-sol transitions. It is worth consideration for how to reverse this process, perhaps by reconstruction of a polypeptide backbone or release of a gelator from a sol-state polypeptide-based copolymer system.

There have been some highly interesting recent studies related to the enzyme-triggered sol-to-gel transition, with the addition of enzymes to interact with the peptide side-chain functionalities and, for instance, facilitate covalent crosslinking reactions.<sup>103,104</sup> A part of these works will be highlighted in the redox part in the next section.

#### *1.4.2 General responsive behaviors due to the versatility of polypeptide side chain functionalities*

The technique to achieve responsive sol-gel transition behavior through control of the chemistries of the polypeptide side chains is not unique to polypeptide gelators but is usually generally applicable. This technique includes the incorporation of photo-, pH- or redox- responsive groups that undergo crosslinking or de-crosslinking upon treatment with a stimulus to achieve phase transition. In this regard, some examples will be described briefly to demonstrate the versatility of polypeptides in the incorporation of various smart functional units.

##### **1.4.2.1 Light**

Sol-gel transitions have been extensively investigated through the chemistry of photo-crosslinking, photo-polymerization, photo-degradation, or isomerization of photo-active compounds, as light is one of the most convenient stimuli to manipulate, with spatiotemporal control. Previously, most of the peptide-based photo-responsive sol-gel transition systems were derived from oligopeptides or polypeptides with defined sequence.<sup>105,106</sup> To incorporate photo-responsive behaviors into the polypeptides synthesized *via* NCA ROP, Ohkawa *et al.* functionalized poly(L-lysine) and poly(L-

ornithine) side chains with coumarin moieties.<sup>107,108</sup> The attached coumarin underwent photo-induced cyclodimerization to create a crosslinked network, resulting in sol-to-gel transition after light irradiation. The crosslinking densities could be controlled *via* light irradiation and the resulting photo-crosslinked gels were degradable by certain enzymes and microorganisms.

#### **1.4.2.2 pH**

Sol-gel transition systems that respond to pH changes have certain advantages over other stimulus-responsive systems. For example, in the application of injectable hydrogels, the sol state of thermo-reversed gelators tends to be thickened and may experience pre-gelation issues, whereas pH responsive systems were designed so that gelation would not occur until the pH of the sol was changed and approached that of physiological conditions.<sup>109</sup> One pH responsive system was described by Dong's group in 2010.<sup>110</sup> In this system, poly(L-glutamic acid)-*block*-PEG (PLG-*b*-PEG) was dissolved in water to form normal micelles (with PLG as core and PEG as shell), or reverse micelles (with  $\beta$ -cyclodextrin/PEG polypseudorotaxanes as core and anionic PLG as shell, with the initial addition of  $\alpha$ -cyclodextrins and NaOH). Both of the normal and reverse micelle systems displayed a pH-responsive behavior, in which gelation occurred at lower pH values when hydrogen-bonding interactions among PLG segments facilitated the formation of the hydrogel network. On the other hand, an increase of the pH deprotonated the PLG segments and the resulting repulsive anionic polyelectrolytes dissociated the hydrogen-bonding and disrupted the micellar formation, further resulting in the gel-to-sol transition. In addition to sol-gel phase transitions, other

macroscopic changes such as volume phase transitions were also achieved with polypeptide-based gels, through control of repulsive polyelectrolyte formation.<sup>111,112</sup>

#### **1.4.2.3 Redox**

Redox-responsive sol-gel transitions have been realized through various chemistries, such as switching the redox states of metal ions in metal complexes,<sup>113,114</sup> and controlling the formation/cleavage of disulfide bonds.<sup>115</sup> Recently, Chen's group developed an injectable hydrogel system, in which the sol-to-gel transition occurred under physiological conditions with the presence of horseradish peroxidase (HRP) and hydrogen peroxide ( $\text{H}_2\text{O}_2$ ).<sup>104</sup> The gelator (PLG-g-TA/PEG) was based on PLG grafted with PEG and tyramine (TA), which underwent crosslinking through enzyme-mediated oxidative reactions using HRP and  $\text{H}_2\text{O}_2$ . As one of the most popular enzymes for enzymatically-crosslinked hydrogels, HRP was shown to be capable of catalyzing the oxidative coupling of aniline or phenol derivatives in the presence of  $\text{H}_2\text{O}_2$  under physiological conditions. Crosslinking of the polypeptide side chain functionalities ultimately resulted in formation of a hydrogel matrix that displayed a sol-to-gel transition on a macroscale. In addition, the gelation time, mechanical strength and porous structure of the resulting hydrogel could be controlled through modulation of the HRP activity.

### **1.5 Scope of the thesis**

This dissertation is focused on the design and development of polypeptide-based gelators derived from NCA ROP, with emphases on gelation mechanism, stimuli-responsive behaviors, and demonstration of potential applications. This thesis starts with

the development a multi-responsive triblock hydrogelator that was able to undergo reversible sol-gel transitions in response to heat, sonication, or enzyme (Chapter II). Then this hydrogelator was mixed with single-walled carbon nanotubes (SWCNT), and was demonstrated with the capability of dispersing and gelating SWCNTs in organic solvents (Chapter III). Based on the responsive sol-gel transition behaviors and dispersion of SWCNTs, a polymer-SWCNT composite was designed for reversible photo-patterning of soft conductive materials (Chapter IV).

In Chapter II, a series of multi-responsive hydrogels composed of PEG tethered oligopeptides, was prepared with extraordinarily low synthetic complexity. The triblock system exhibited reversible and repeatable sol-to-gel and gel-to-sol transitions that can be triggered by heat and sonication, respectively. In addition, certain enzymes accelerated the breakdown of the bio-responsive hydrogels into sols. The ability to form hydrogels is shown to be dependent on the hydrophobic and hydrophilic balance and is dictated by the block length of the oligopeptide blocks, which is in turn easily controlled by reaction feed ratio. Detailed characterization studies indicated that hydrogelation may be driven by a combination of oligopeptide  $\beta$ -sheeting and a balance between PEG-PEG interactions and PEG-water interactions, with effects observed at the supramolecular, nano-, micro- and macro-scales. Moreover, the oligopeptide segments carry reactive allyl side chain groups, which have the potential to be further functionalized into intelligently-designed systems of increased complexity and functionality.

With these triblock PEG-tethered oligopeptides, in Chapter III, SWCNTs were efficiently dispersed in the triblock network, with low compositional and structural complexity, being based upon a hydrophilic PEG middle block and two hydrophobic racemic synthetic oligopeptide end segments. Detailed characterization studies indicated that the supramolecular self-assembly of  $\beta$ -sheets in the oligopeptide blocks form one dimensional stacked nanoribbons, in which allyl-rich ODLAG peptide domains have strong propensity for  $\pi$ - $\pi$  stacking with SWCNT surfaces, and consequently, efficiently separated and dispersed SWCNTs in organic solvent. The ODLAG peptide  $\beta$ -sheets could both noncovalently associate with the SWCNTs and assemble peptide-coated nanotubes into hierarchically-ordered structures *via* peptide-peptide interactions. Despite these structures manifesting on the nanoscale, micro/mesoscale homogeneity was increased in the composite gels when compared to the triblock gel alone. With the incorporation of SWCNTs the mechanical properties of triblock-based organogels increased greatly, further displaying a dispersed (not merely encapsulated) state in the gel matrix.

Based upon the above these studies, in Chapter IV, a hydrogel-based block copolymeric/inorganic composite system that exhibited a wide range of thermo-, mechano- and photo-responsive properties was developed. These materials are highly processable with assorted stimuli inputs, including temperature increase or photo irradiation for gelation and patterning, and sonication for material recycling. Furthermore, this system provided a novel method to process conductive materials in a liquid phase, followed by facile and rapid curing into desired patterns with the potential



to take advantage of the modern photo stereolithographic technologies, without the requirement of a pre-treated substrate or a specific irradiation wavelength.

## CHAPTER II

# MULTI-RESPONSIVE HYDROGELS DERIVED FROM THE SELF-ASSEMBLY OF TETHERED ALLYL-FUNCTIONALIZED RACEMIC OLIGOPEPTIDES\*

### 2.1 Introduction

Stimuli-responsive hydrogels have attracted significant attention in the last two decades with a wide range of applications being targeted for controlled drug release,<sup>116</sup> tissue engineering,<sup>117</sup> flow control,<sup>118</sup> and selective sensing<sup>14</sup>. Commonly used stimuli for responsive hydrogels include temperature,<sup>71,119</sup> light,<sup>120</sup> pH,<sup>121</sup> enzymes,<sup>122</sup> sonication,<sup>94</sup> and oxidation-reduction.<sup>115</sup> Temperature, pH, and enzymes are particularly interesting stimuli for applications in biological systems. In part, this is due to local physiological environments being different from ex situ environments, which can lead to highly specific triggered response for systems that need both sol and gel type behavior during different periods of their usage. Applied stimuli typically trigger construction or deconstruction of the hydrogel networks by either covalent<sup>123</sup> or non-covalent interactions.<sup>71</sup> Recently, hydrogels composed of materials with non-covalent interactions have received attention due to their ability to rapidly respond to physical or chemical stimuli, the versatility to self assemble into different nano- or micro-structures in different environments, and the ability to exhibit changes in macroscopic

---

\* Reprinted (adapted) with permission from “Multi-responsive Hydrogels Derived from the Self-assembly of Tethered Allyl-functionalized Racemic Oligopeptides” by He, X.; Fan, J.; Zhang, F.; Li, R.; Pollack, K. A.; Raymond, J. E.; Zou, J.; Wooley, K. L., *J. Mater. Chem. B* **2014**, 2, 8123-8130. Copyright 2014 The Royal Society of Chemistry.

characteristics, such as sol-gel transitions.<sup>124,125</sup> Compared with single stimulus-responsive systems, dual- or multi-responsive hydrogels provide higher flexibility in material fabrication and opportunities to achieve greater control of physical configurations or additional kinetic properties (*e.g.* degradation or drug release).<sup>126,127</sup> For instance, Lee *et al.* reported an injectable hydrogel, for which hydrogelation occurred with a slight change of the pH at physiological conditions upon injection, followed by slow release of insulin owing to the hydrolytic degradation of polymer backbone.<sup>128</sup> A difficulty in developing a catalogue of multi-responsive systems is the requirement for precise control of one or more chemistries within the system, ultimately, leading to increasingly difficult synthetic approaches. The generation of multi-responsive materials, thus, remains a challenge.

The generation of peptide-based hydrogels is a topic of intense interest to achieve increased biocompatibility,<sup>104,129</sup> specific enzymatic response<sup>130,131</sup> and versatility of supramolecular assembly.<sup>110</sup> The formation of these hydrogel matrices can be attributed, in the majority of cases, to the entanglement of fibrillar structures assembled through noncovalent interactions, such as hydrogen bonding,<sup>132</sup>  $\pi$ - $\pi$  stacking,<sup>133</sup> electrostatic interactions,<sup>134</sup> and/or hydrophobic interactions.<sup>87,135</sup> A focus on hydrogen bonding in peptide-rich systems is particularly appropriate, as it is a primary factor in the formation of robust secondary structures, including  $\alpha$ -helix<sup>24,49,136</sup> or  $\beta$ -sheet,<sup>134</sup> depending on the type or sequence of amino acids. Specifically, we are interested in the utilization of DL-allylglycine. The ease with which various functionalities can be incorporated into poly(DL-allylglycine) (PDLAG) through thiol-ene click chemistry<sup>137</sup> and the strong

gelation properties it possesses in organic solvents<sup>68</sup> make it an ideal candidate for advanced applications when compared with other  $\beta$ -sheet-forming peptides composed of natural amino acids (*e.g.* valine, alanine, isoleucine, *etc.*). Recently, gels composed of PEG-*b*- $\beta$ -sheet-peptides synthesized by ring-opening polymerization (ROP) of *N*-carboxyanhydrides (NCAs) have been described by Jeong,<sup>138</sup> Heise,<sup>76</sup> Li,<sup>78</sup> and Chen<sup>77</sup> to show a reverse thermal gelation profile (heat-induced sol-to-gel transition), and have been reported by our group to exhibit gel-to-sol or gel-to-gel behavior with sonication.<sup>99</sup> To the best of our knowledge, oligo or polyDLAG have not been used directly in the formation of hydrogels. Therefore, we chose to investigate this system to determine its stimuli-responsive properties by seeking a suitable chemical structure and hydrophobic-hydrophilic balance.

Herein, we report a thermo-, sonication-, and enzyme-responsive ODLAG-*b*-PEG-*b*-ODLAG hydrogelator. The hydrophobic blocks are synthesized facilely by ring-opening polymerization of racemic allylglycine. Although racemic peptides (*vs.* stereoregular peptides) are reported to have a lower ability to form  $\alpha$ -helix or  $\beta$ -sheet secondary structures,<sup>49,139,140</sup> these ODLAG-*b*-PEG-*b*-ODLAG hydrogels were found to have critical gelation concentrations as low as 1.0 wt%. Furthermore, in contrast to many polypeptide-based hydrogelators which undergo gel melting with increased temperature,<sup>87,141</sup> a reverse thermal gelation profile was observed. The driving force for this heat induced gelation is discussed in conjunction with a comprehensive study of the responsive behaviors. This multi-responsive hydrogel system is appropriate to serve as a platform for the development of drug delivery vehicles, sensors, and smart devices.

## 2.2 Experimental section

### 2.2.1 Materials

Ethyl acetate, *n*-hexane, tetrahydrofuran (THF), diethyl ether, N,N-dimethylformamide (DMF, anhydrous,  $\geq 99.8\%$ ), trifluoroacetic acid (TFA), DL-allylglycine,  $\alpha$ -pinene, and triphosgene were purchased from Sigma-Aldrich Company (USA).  $\alpha,\omega$ -Diamino-terminated poly(ethylene glycol) ( $\text{NH}_2\text{-PEG}_{68}\text{-NH}_2$ ,  $M_n = 3000$  g/mol) was purchased from Rapp Polymere (Germany). All chemicals were used without further purification, unless otherwise noted. Nanopure water ( $18\text{ M}\Omega\cdot\text{cm}$ ) was acquired by means of a Milli-Q water filtration system, Millipore Corp (USA).

### 2.2.2 Instrumentation

$^1\text{H}$  and  $^{13}\text{C}$  NMR spectra were recorded on a Varian Inova 300 spectrometer interfaced to a UNIX computer using VnmrJ software. Chemical shifts were referenced to the solvent resonance signals. Attenuated total reflection Fourier transform infrared spectroscopy (ATR-FTIR) spectra were recorded on an IR Prestige 21 system (Shimadzu Corp.) and analyzed using IRsolution v. 1.40 software.

Matrix assisted laser desorption ionization mass spectrometry (MALDI-TOF MS) was performed on a Kratos/Shimadzu Axima CFR (Manchester, England) MALDI-TOF mass spectrometer. Ions were generated by nitrogen laser at 337 nm, a frequency of 10 Hz, and an acceleration voltage of 25 kV. Dithranol was used as the matrix. The polymer sample was dissolved in TFA (10 mg/mL), and dithranol was dissolved in THF (35 mg/mL). The sample solution was mixed with the matrix at a volume ratio of 1:1

before being spotted onto a sample plate. The sample was then analyzed under linear conditions.

Thermogravimetric analysis (TGA) was performed under argon atmosphere using a Mettler Toledo model TGA/DSC 1 (Mettler Toledo, Inc., Columbus, OH), with a heating rate of 10 °C/min. Measurements were analyzed using Mettler Toledo STAR<sup>c</sup> v. 7.01 software. Glass transition temperatures ( $T_g$ ) were measured by differential scanning calorimetry (DSC) on a Mettler Toledo DSC822<sup>®</sup>, with a heating rate of 10 °C/min and a cooling rate of 10 °C/min. Measurements were analyzed using Mettler Toledo STAR<sup>c</sup> v. 7.01 software. The  $T_g$  was taken as the midpoint of the inflection tangent, upon the third heating scan.

Wide-angle X-ray scattering (WAXS) was performed on a Bruker D8 Bragg-Brentano X-ray powder diffractometer. The sample was placed in the sample holder of a two circle goniometer, enclosed in a radiation safety enclosure. The X-ray source was a 2.2 kW Cu X-ray tube, maintained at an operating current of 40 kV and 40 mA. The X-ray optics was the standard Bragg-Brentano para-focusing mode with the X-ray diverging from a DS slit (1 mm) at the tube to strike the sample and then converging at a position sensitive X-ray Detector (Lynx-Eye, Bruker-AXS). The two-circle 250 mm diameter goniometer was computer controlled with independent stepper motors and optical encoders for the  $\theta$  and  $2\theta$  circles with the smallest angular step size of 0.0001°  $2\theta$ . The software suit for data collection and evaluation was window based. Data collection was automated COMMANDER program by employing a DQL file and analyzed by the program EVA.

Dynamic mechanical analysis (DMA) was performed on a Mettler Toledo TT-DMA system. DMA measurements of the hydrogels (5 wt%) were performed over 3 h in compression on a 3.2 mm thick, 10 mm diameter cylinder. Dynamic measurements were recorded over a range of 0.1 to 10 Hz at room temperature with static stress modulated to 2% compression and a dynamic force applied to provide  $\pm 1\%$  deformation. Kinetic data presented were obtained as a single exponential decay using Origin Pro 8.1 software.

Transmission electron microscopy (TEM) images were collected on a JEOL 1200 EX operating at 100 kV and micrographs were recorded at calibrated magnifications using a SLA-15C CCD camera. Samples for TEM measurements were prepared as follows: 10  $\mu\text{L}$  of the dilute solution was deposited onto a carbon-coated copper grid, and after 2 min, the excess of the solution was quickly wicked away by a piece of filter paper. The samples were then negatively stained with 1 wt% phosphotungstic acid (PTA) aqueous solution. After 30 s, the excess staining solution was quickly wicked away by a piece of filter paper and the samples were left to dry under vacuum overnight.

Scanning electron microscopy (SEM) imaging was performed in JOEL JSM-6400 SEM operated at an acceleration voltage of 15 kV. The preparation of samples for SEM involved placing a drop of hydrogel on a carbon thin film. The gel was then subjected to immediate freezing by liquid nitrogen, followed by lyophilization for 3 days. The surface of the gel was sputter coated with gold for 3 min under argon before imaging.

Sonication was performed in an ultrasonic homogenizer (maximum power, 150 W, 20 kHz, Model 150 V/T, Biologics, Inc.) equipped with a micro tip with a diameter of 3.81 mm, employing the power output of 30 W in the frequency of 20 kHz at room temperature.

### 2.2.3 Synthesis

Synthesis of DL-allylglycine *N*-carboxyanhydride (DLAG NCA). The DLAG NCA monomer was prepared following the previously reported method.<sup>142</sup> In a 250 mL two-neck flask, equipped with septum and pipet for nitrogen inlet and a condenser with a tubing connector that allowed outlet flow through a base solution (NaOH<sub>(aq)</sub>), DL-allylglycine (2.52 g, 21.9 mmol) was dissolved in 100 mL THF and triphosgene (5.41 g, 18.2 mmol) was added directly to the reaction flask.  $\alpha$ -Pinene (7 mL) was then added and the reaction mixture was allowed to stir for 2.5 h at 50 °C, while being constantly flushed with a stream of dry nitrogen. The crude product was concentrated and precipitated from *n*-hexane, recrystallized four times from ethyl acetate/*n*-hexane 1:8 (v/v), and then dried *in vacuo*; yielding 1.02 g (40%) of product as a white needle-like crystal. <sup>1</sup>H NMR (300 MHz, CDCl<sub>3</sub>, ppm):  $\delta$  2.55 and 2.75 (m, 2 H, CH<sub>2</sub>), 4.42 (m, 1 H, CH), 5.31 (m, 2 H, H<sub>2</sub>C=CH), 5.77 (m, 1 H, H<sub>2</sub>C=CH), 6.55 (br, 1 H, NH). <sup>13</sup>C NMR (75 MHz, CDCl<sub>3</sub>, ppm):  $\delta$  36.0, 57.4, 121.7, 130.0, 152.7, 169.0. FT-IR (cm<sup>-1</sup>): 3345, 3017, 2934, 1825, 1748, 1290, 926. HRMS: calculated [M-H]<sup>-</sup> for C<sub>6</sub>H<sub>7</sub>NO<sub>3</sub>: 140.0353, found: 140.0354.

Synthesis of ODLAG-*b*-PEG-*b*-ODLAG. A typical procedure for the preparation of ODLAG-*b*-PEG-*b*-ODLAG was as follows: into a flame-dried 25 mL



Schlenk flask equipped with a stir bar and capped with a rubber stopper with a needle outlet connected to a tube filled with drying agent, DLAG-NCA (281.9 mg, 1.998 mmol) in DMF (8 mL) was injected. After being stirred at room temperature for 5 min, NH<sub>2</sub>-PEG<sub>68</sub>-NH<sub>2</sub> (497.6 mg, 0.1659 mmol) in DMF (8 mL) was injected *via* a syringe. The reaction mixture was stirred at room temperature (stir rate = 340 rpm) under continuous nitrogen flow (flow rate = 100 mL/min) for 6 h. The reaction mixture was then precipitated into 180 mL diethyl ether twice. The triblock was centrifuged, collected, and dried *in vacuo* to yield 450.0 mg (64.8%) as a white powder. <sup>1</sup>H NMR (300 MHz, DMSO-d<sub>6</sub>, ppm):  $\delta$  2.34 (br, 24 H, CHCH<sub>2</sub>CHCH<sub>2</sub>), 3.50 (br, 272 H, OCH<sub>2</sub>) 4.34 (br, 12 H, NHCHCO), 5.00 (br, 24 H, CH<sub>2</sub>CHCH<sub>2</sub>), 5.69 (br, 12 H, CH<sub>2</sub>CHCH<sub>2</sub>), 8.09 (br, 12 H, COCHNH). <sup>13</sup>C NMR (75 MHz, DMSO-d<sub>6</sub>, ppm):  $\delta$  36.5, 52.1, 69.8, 117.5, 134.0, 170.5. FT-IR (cm<sup>-1</sup>): 3672-3402, 3284, 3075, 2870, 1667, 1626, 1526, 1101, 696. DSC:  $T_g$  = -18 °C,  $T_c$  = 4 °C,  $T_m$  = 37 °C,  $T_g$  = 102 °C. TGA: 25-303 °C: 0% mass loss, 303-376 °C: 26% mass loss, 376-423 °C: 50% mass loss, 423-500 °C: 3% mass loss, 21% mass remaining above 500 °C. Other copolymers with different degrees of polymerization (DP<sub>n</sub>) were similarly prepared, and the compositions of the resulting copolymers are listed in Table 2.1.

## 2.3 Results and discussions

With our general interest in the creation of biodegradable stimuli-responsive materials that are synthetically approachable while also being modifiable, specifically for applications in biology and medicine, we began investigations into the syntheses and gelation properties of peptide-containing amphiphilic block copolymers with easily

modifiable allyl side chain groups. Recently, our group reported a polypeptide-based organogelator, PEG-*b*-PDLAG, with ultralow critical gelation concentrations (*ca.* 0.1 wt%) in various organic solvents.<sup>68</sup> Here, we took advantage of the strong gelation capability of PEG-*b*-PDLAG system in organic solvents and extended this capability into aqueous medium by designing a triblock structure, in which two oligopeptide segments were tethered by a central PEG block (Fig. 2.1).

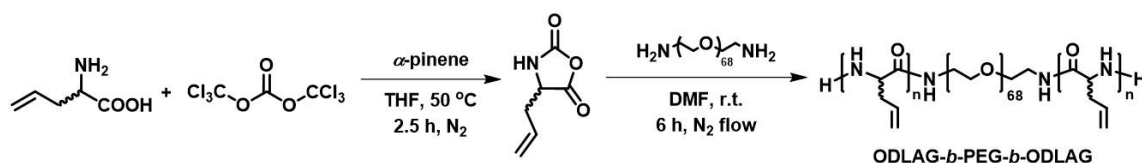


**Figure 2.1.** Synthesis of ODLAG<sub>6</sub>-*b*-PEG<sub>68</sub>-*b*-ODLAG<sub>6</sub>

**Table 2.1.** Synthesis and hydrogelation capabilities of ODLAG-*b*-PEG-*b*-ODLAG with different lengths of ODLAG blocks

Polymer	[I] <sub>0</sub> : [M] <sub>0</sub>	DP <sub>n</sub> <sup>a</sup>	Hydrogelation <sup>b</sup>	C <sub>gel</sub> <sup>b,d</sup>
1	1 : 5	5	No	N/A
2	1 : 12	12	Yes	1.0 wt%
3	1 : 18	18	No <sup>c</sup>	N/A

<sup>a</sup> Degree of polymerization, calculated by <sup>1</sup>H NMR spectroscopy, equal to the total number of the repeating units of both ODLAG blocks; <sup>b</sup> determined by test tube inversion method; <sup>c</sup> precipitates were observed; <sup>d</sup> critical gelation concentrations, in water

NCA ROPs have been widely used in the syntheses of polypeptide-based materials with well-defined structures at large scales because of the advancement of living polymerization strategies that have occurred in the last two decades.<sup>44,48,50,51,53</sup>

Recently, we found that NCA ROPs can be conducted by normal Schlenk techniques, with the enhancement of polymerization rates and retention of living features by a straightforward N<sub>2</sub> flow method.<sup>57</sup> Therefore, in this synthetic route, ROP of DLAG NCA (M) with continuous N<sub>2</sub> flow (100 mL/min) over the reaction solution was utilized with  $\alpha,\omega$ -diamino-terminated poly(ethylene glycol) (NH<sub>2</sub>-PEG<sub>68</sub>-NH<sub>2</sub>, I) as a macroinitiator. For each polymerization (Table 2.1), varied ratios of NCA monomer and PEG initiator were dissolved in anhydrous DMF and the ROPs were allowed to proceed for 6 h at room temperature, until the monomer conversions had reached *ca.* 99%, as determined by the intensity of NCA anhydride absorption at 1786 cm<sup>-1</sup> from attenuated total reflectance-Fourier transform infrared spectroscopy (ATR-FTIR). The reaction mixtures were then precipitated into diethyl ether and dried under vacuum to yield the triblock structures with controlled block sizes as white solids.

The degrees of polymerization and molecular weights were determined by <sup>1</sup>H NMR spectroscopy and MALDI-TOF mass spectrometry. Fortuitously, our systems had a delayed gelation response in DMSO, allowing confirmation of polymerization by <sup>1</sup>H NMR spectroscopy. In addition, degrees of polymerization were analyzed by comparison of the intensities of methylene proton resonances of the PEG chain at *ca.* 3.5 ppm (f in Fig. 2.2) with the intensities of ODLAG methine proton at *ca.* 5.7 ppm (d in Fig. 2.2), or the alkenyl protons at *ca.* 5.0 ppm (e and e' in Fig. 2.2), or the methylene protons at *ca.* 2.3 ppm (c in Fig. 2.2). A MALDI-TOF measurement using dithranol as matrix was also carried out to characterize the molecular weight of ODLAG<sub>6</sub>-*b*-PEG<sub>68</sub>-*b*-ODLAG<sub>6</sub>. As shown in Fig. 2.3, the distribution with molecular weight centered at *ca.*

4.0 kDa was consistent with the number-average molecular weight calculated by  $^1\text{H}$  NMR (*ca.* 4.2 kDa). Due to gelation or aggregate formation in most of the organic solvents (Table 2.2), gel permeation chromatography (GPC) was not employed to characterize the polymer.

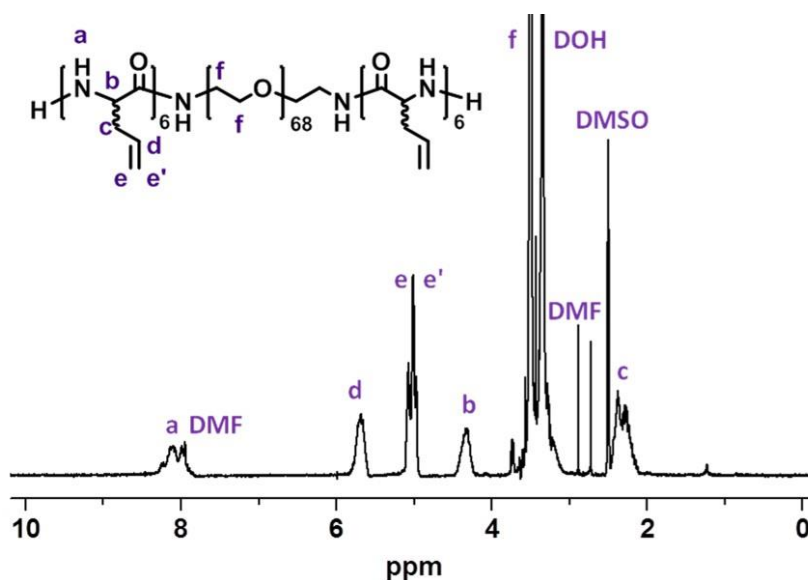


**Figure 2.2.**  $^1\text{H}$  NMR spectrum of  $\text{ODLAG}_6\text{-}b\text{-PEG}_{68}\text{-}b\text{-ODLAG}_6$

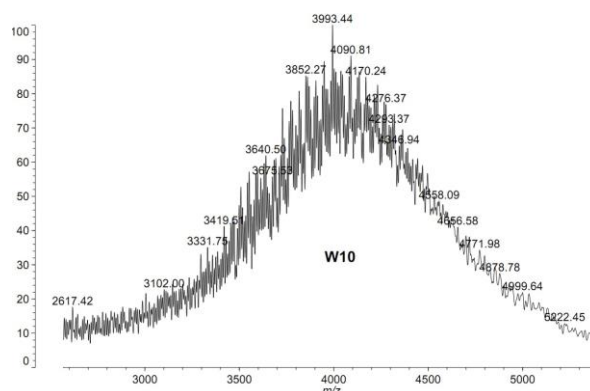


**Figure 2.3.** MALDI-TOF mass spectrum of  $\text{ODLAG}_6\text{-}b\text{-PEG}_{68}\text{-}b\text{-ODLAG}_6$ .

**Table 2.2.** Solubility studies of ODLAG<sub>6</sub>-*b*-PEG<sub>68</sub>-*b*-ODLAG<sub>6</sub> in different organic solvents.

Solvent <sup>a</sup>	State <sup>b</sup>
DMF	Gel
DMSO	Gel
Methanol	Gel
TFA	Solution
CHCl <sub>3</sub>	Suspension
Toluene	Suspension
Ethyl acetate	Suspension
Hexane	Suspension
THF	Suspension
Isopropanol	Suspension

<sup>a</sup> The concentration of ODLAG<sub>6</sub>-*b*-PEG<sub>68</sub>-*b*-ODLAG<sub>6</sub> was 5.0 wt% in each solvent.

<sup>b</sup> Observed after resting in room temperature for 72 h.

The ability to form hydrogels for ODLAG-*b*-PEG-*b*-ODLAG with different block lengths of oligopeptides was explored (Table 2.1). It can be concluded from the data of Table 2.1 that precise control of block lengths for the oligopeptides is required for gelation. Polymers 1 or 3, which had either shorter or longer block lengths of oligopeptides, compared with polymer 2, respectively, did not form hydrogels.

A thorough assessment of the physical gelation properties of ODLAG<sub>6</sub>-PEG<sub>68</sub>-ODLAG<sub>6</sub> hydrogels was performed, with data presented in Fig. 2.4. To prepare the hydrogel systems, denoted weight fractions of polymers and aqueous media were mixed and sol-to-gel transitions were observed when the systems were heated to the gel transition temperatures ( $T_{\text{gel}}$ ), which were measured by the test tube inversion method with a temperature increment step of 1 °C per 20 min. The formed hydrogels were stable and no gel-to-sol transitions were observed when they were left undisturbed for a long period (> 2 weeks) at room temperature. In order to probe the effect of polymer

concentration on  $T_{\text{gel}}$ , the  $T_{\text{gel}}$  values of a series of hydrogels with varying polymer concentration of 2 were measured. The sol-gel phase diagram revealed that  $T_{\text{gel}}$  decreased with increase of polymer concentration from 1.0 wt% (95 °C) to 10 wt% (80 °C), and was then maintained at *ca.* 80 °C. Furthermore, DMA was used to assess the mechanical response of the gels. A hydrogel with a polymer concentration of 5 wt% was used in the DMA study, which produced a robust gel appropriate for high frequency operation. With larger operating frequency, both the storage ( $E'$ ) and loss ( $E''$ ) moduli increased at similar rate, indicating a shear thickening response (Fig. 2.5). Given the time-temperature superposition principle of DMA, this finding is expected for a gel system with triggered gelation at increased temperatures. During the overall range of frequency modulation (0.1 to 10 Hz),  $E''$  maintained smaller than  $E'$ , indicating no gel-to-sol transition was taking place in this frequency range at room temperature. In fact, the  $\tan(\delta)$  data indicated increased stiffness with sustained shear as well (Fig. 2.6).

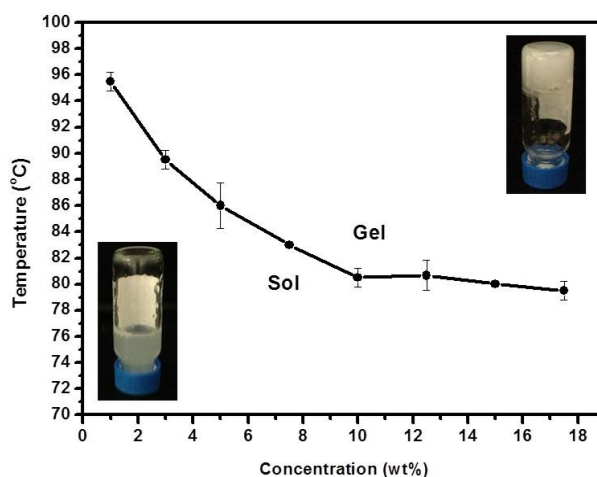


**Figure 2.4.**  $T_{\text{gel}}$  of ODLAG<sub>6</sub>-*b*-PEG<sub>68</sub>-*b*-ODLAG<sub>6</sub> as a function of concentration.

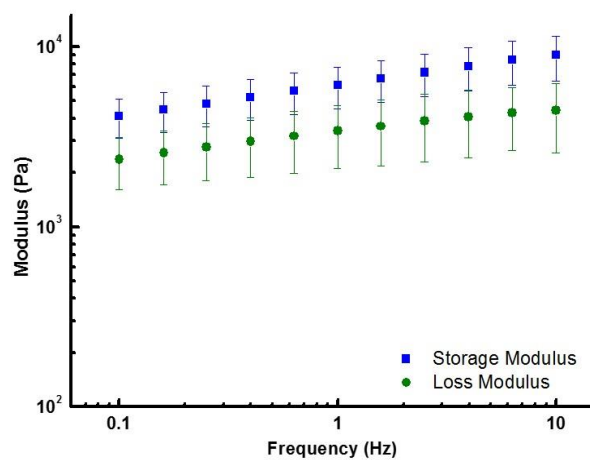


**Figure 2.5.** Storage and loss moduli of ODLAG<sub>6</sub>-*b*-PEG<sub>68</sub>-*b*-ODLAG<sub>6</sub> hydrogel (5 wt%) as a function of frequency conducted by DMA at room temperature.

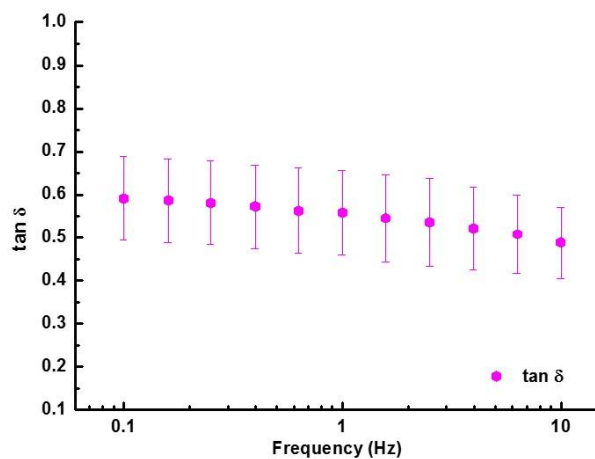


**Figure 2.6.** Tan ( $\delta$ ) of ODLAG<sub>6</sub>-*b*-PEG<sub>68</sub>-*b*-ODLAG<sub>6</sub> hydrogel (5 wt%) as a function of frequency conducted by DMA at room temperature.

In order to study the driving force for the sol-to-gel transition, the supramolecular structure of the dried hydrogel was investigated by ATR-FTIR and WAXS, with both characterization techniques indicating the existence of  $\beta$ -sheet conformations. Characteristic strong absorption of an amide I band at  $1626\text{ cm}^{-1}$  and a shoulder peak at  $1667\text{ cm}^{-1}$  were attributed to corresponding parallel and antiparallel  $\beta$ -sheet conformations of the peptide blocks, respectively (Fig. 2.7).<sup>69,134</sup> In addition, a peak in the amide II region at  $1526\text{ cm}^{-1}$  and an amide V band at *ca.*  $700\text{ cm}^{-1}$  were observed in accordance with  $\beta$ -sheet structures, in contrast to peptides with  $\alpha$ -helix conformations, which tend to have low or no absorption at *ca.*  $700\text{ cm}^{-1}$ .<sup>143,144</sup> Comparison of ATR-FTIR spectra with  $\text{NH}_2\text{-PEG}_{68}\text{-NH}_2$  and DLAG NCA, which expressed no characteristic peaks in these regions, indicated that the  $\beta$ -sheeting was due to the formation of ODLAG blocks upon polymerization.

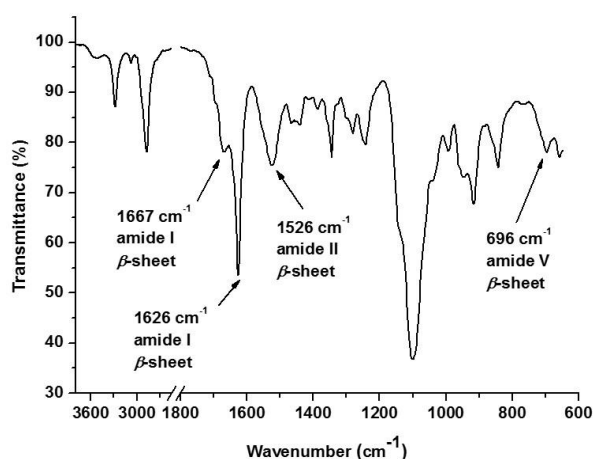


**Figure 2.7.** ATR-FTIR spectrum of a dried hydrogel made from ODLAG<sub>6</sub>-*b*-PEG<sub>68</sub>-*b*-ODLAG<sub>6</sub>.



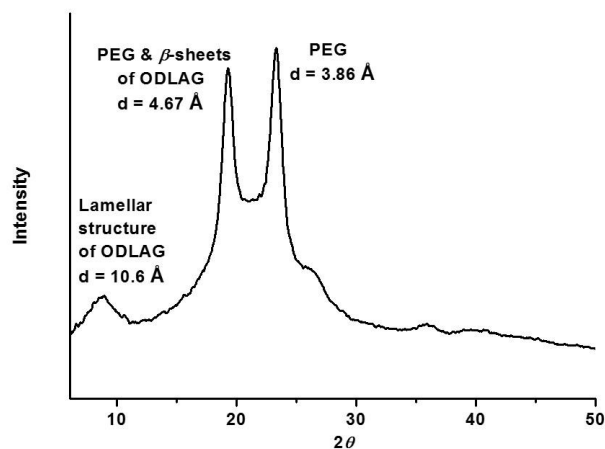


**Figure 2.8.** WAXS pattern of a dried ODLAG<sub>6</sub>-*b*-PEG<sub>68</sub>-*b*-ODLAG<sub>6</sub> hydrogel.

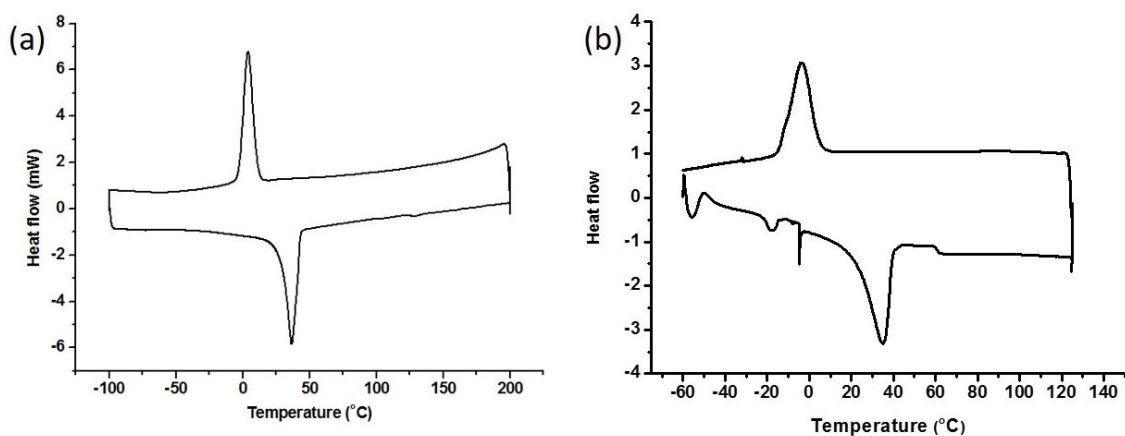


**Figure 2.9.** (a) DSC trace of ODLAG<sub>6</sub>-*b*-PEG<sub>68</sub>-*b*-ODLAG<sub>6</sub> in the solid state. The samples were heated from -100 °C to 200 °C and cooled back to -100 °C with both heating and cooling rates of 10 °C/min. The third heating and cooling traces were shown here. (b) DSC trace of ODLAG<sub>6</sub>-*b*-PEG<sub>68</sub>-*b*-ODLAG<sub>6</sub> in the solid state, after rapid cooling above the  $T_m$ . The sample was removed from the DSC at 125 °C, immersed into liquid nitrogen and returned into the DSC during the second cycle. The third heating and cooling traces are shown here.

WAXS study also confirmed the existence of  $\beta$ -sheets. The d spacing of 10.6 Å was assigned to the inter-sheet distance of peptide segments (Fig. 2.8).<sup>145,146</sup> A d spacing of *ca.* 4.67 Å was described in a variety of  $\beta$ -sheet forming peptides as a characteristic hydrogen bonding length in the conformation of  $\beta$ -sheet secondary structures.<sup>99,147,148</sup> This WAXS signal overlapped with the 120 reflection of monoclinic PEG crystals,<sup>69</sup> which together with the signal corresponding to a d spacing of 3.86 Å correlated well with the crystallization and melting peaks in the DSC trace (Fig. 2.9).

TEM and SEM were also utilized to characterize the nanostructural morphologies of the ODLAG<sub>6</sub>-*b*-PEG<sub>68</sub>-*b*-ODLAG<sub>6</sub> hydrogel. The TEM sample was prepared with a polymer concentration of 1 mg/mL from dilution of a 5 wt% hydrogel, and stained by a PTA aqueous solution. Fibrillar morphologies with micron scale fibers were observed as bundles in many cases (Fig. 2.10). Reasonable contributions to the formation of bundles include supramolecular cross-linking from residual peptide chain

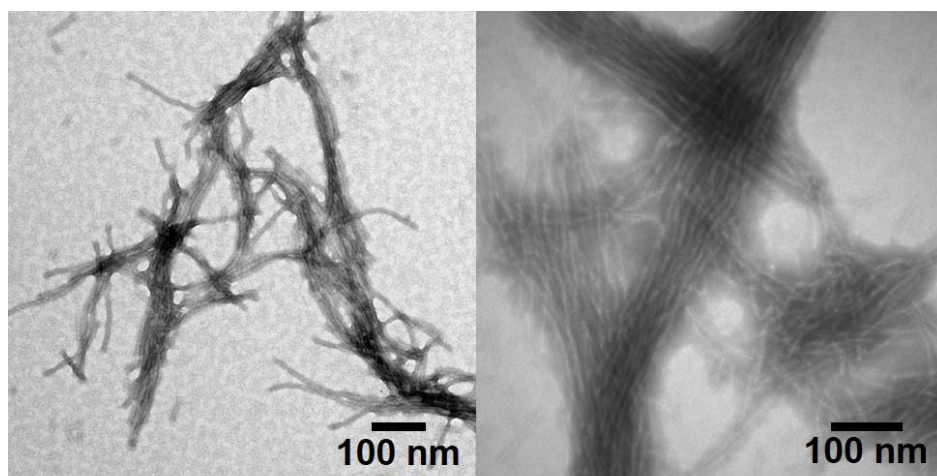


**Figure 2.10.** TEM images of a ODLAG<sub>6</sub>-*b*-PEG<sub>68</sub>-*b*-ODLAG<sub>6</sub> hydrogel.

ends at the surface of the fibrils and inter-fibrillar PEG-PEG interactions arising from strong semi-crystalline binding sites.

To visualize the ODLAG<sub>6</sub>-*b*-PEG<sub>68</sub>-*b*-ODLAG<sub>6</sub> hydrogel on the microscale, SEM was used on samples that were prepared by freeze-drying (to maintain the network structures of hydrogels). From SEM, it can be observed that three-dimensional interconnected networks were formed in the system, a necessary feature of hydrogels (Fig. 2.11a). The network possessed a highly porous structure with a broad range of pore sizes (Fig. 2.11b). Direct observation of network porosity is fortunate, as it allows for the potential to encapsulate cargoes such as therapeutic drugs or cells in biological applications.

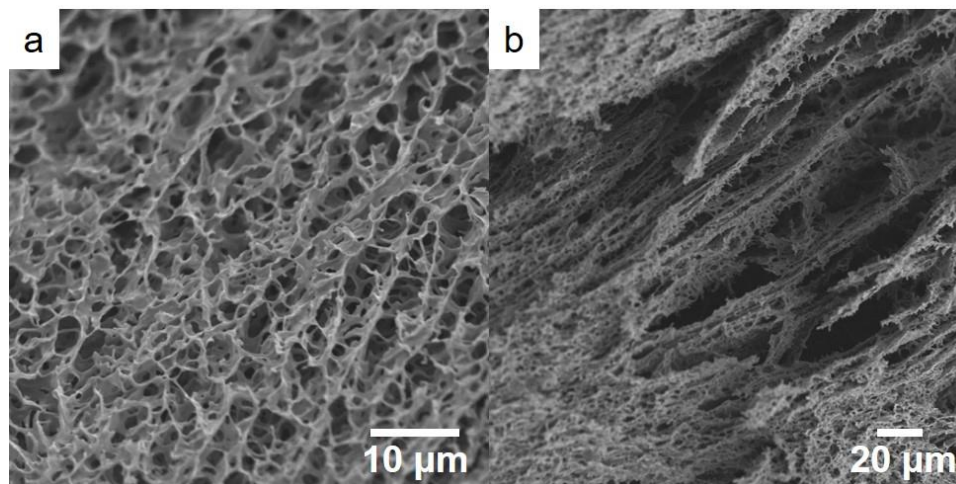


**Figure 2.11.** SEM images of a ODLAG<sub>6</sub>-*b*-PEG<sub>68</sub>-*b*-ODLAG<sub>6</sub> hydrogel.

Based on the results from ATR-FTIR, WAXS, TEM and SEM analyses, a mechanism for the hydrogelation of ODLAG<sub>6</sub>-*b*-PEG<sub>68</sub>-*b*-ODLAG<sub>6</sub> can be proposed

(Fig. 2.12). Self-assembly of the triblock structures into fibers is driven by intermolecular hydrogen bonding of oligopeptide blocks (in red) as hydrophobic domains, which further self-organize into parallel or antiparallel  $\beta$ -sheets. The hydrophilic PEG block (in blue) prevents precipitation of the fibers by increasing the aqueous solubility, and maintains the hydrogel structure by capturing water molecules. The thermo-gelation profile may result from heat-induced formation of  $\beta$ -sheets and lower water occupancy of the volume that would normally have strong PEG-water associations at lower temperatures, both of which can enhance the hydrophobic interactions.<sup>76-78,138,149</sup> As observed in TEM, supramolecularly cross-linked fibers can be formed, with possible mechanisms including inter-fibrillar peptide-peptide interaction or PEG-PEG associations. The entanglement resulting from long range interactions of fibers plays an integral part in the construction of the hydrogel matrix, as observed by SEM.

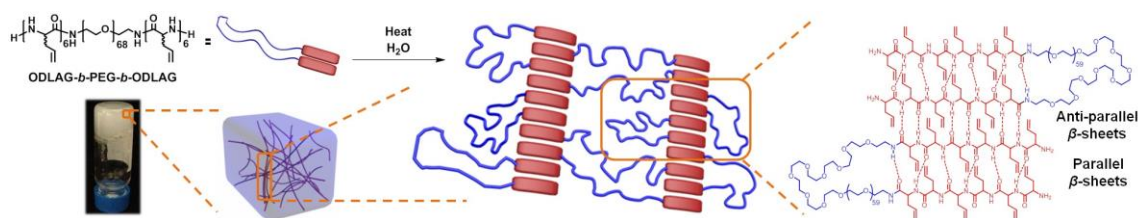


**Figure 2.12.** An illustrative scheme for the formation of nanofibers and hydrogels formed from self-assembly of ODLAG<sub>6</sub>-*b*-PEG<sub>68</sub>-*b*-ODLAG<sub>6</sub>.

The multi-responsive properties of ODLAG<sub>6</sub>-*b*-PEG<sub>68</sub>-*b*-ODLAG<sub>6</sub> hydrogels (Fig. 2.13a), and the correlation of nanostructure with physical behavior were investigated.

As shown in the phase diagram (Fig. 2.4), a reverse thermal gelation behavior was observed. Sol-to-gel transitions occurred by maintaining the sol state at  $T_{\text{gel}}$  for 20 min, while gel-to-sol transitions were achieved by sonication in less than 10 s. The sol-gel transitions could be conducted for a minimum of 5 cycles without apparent change in gel transition temperatures, which indicated the reversibility of the supramolecular assembly of these physical hydrogels. In order to further understand the hydrogelation and gel breaking behaviors, TEM was employed to compare the differences in nanostructural morphologies between the sol and gel states. The sol state sample was prepared by subjecting the hydrogel to sonication for 10 s, followed by dilution and staining using similar methods to the hydrogel sample. Drastically different from the micrometer-long fibrillar morphologies observed in the gel state (Fig. 2.10), spherical aggregates and shorter nanofibrils (*ca.* 100 nm in length) were observed for the sol state (Fig. 2.13b). The sonication-promoted gel-to-sol transition implies a fundamental disruption of the fibrils, converting them into spherical aggregates incapable of long range interactions, and not a mere disruption of long range fiber interactions.

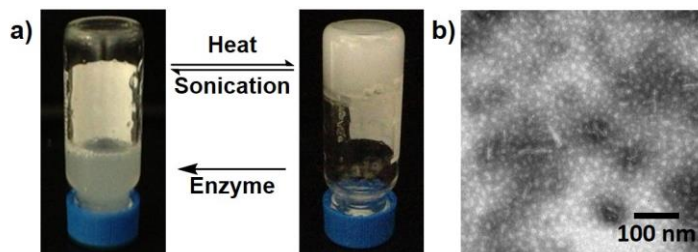


**Figure 2.13.** (a) Digital photographs showing responsiveness of ODLAG<sub>6</sub>-*b*-PEG<sub>68</sub>-*b*-ODLAG<sub>6</sub> hydrogels towards different stimuli. (b) TEM image of a ODLAG<sub>6</sub>-*b*-PEG<sub>68</sub>-*b*-ODLAG<sub>6</sub> sol.

Enzyme-responsiveness of this hydrogel system was observed by studying in vitro hydrogel weight loss profiles, which were assessed by measuring the weight loss of hydrogels (5 wt%) incubated at 37 °C in 1.5 mL vials. Tris-HCl buffer (0.05 M, pH = 8.0, 0.2 wt% NaN<sub>3</sub>) containing 1 mg/mL proteinase K or trypsin was used as the degradation medium, and hydrogels with Tris-HCl buffer were used as the control. The buffer solution (0.5 mL) was gently added into each vial prior to incubation, and was removed along with any gel debris that had accumulated. According to the weight loss profiles, hydrogels that were subjected to enzymes (proteinase K and trypsin) broke down much faster than did the control (Fig. 2.14). For example, around 70% and 50% weight losses in 48 h were observed for the hydrogels incubated in the medium with proteinase K and trypsin, respectively, while *ca.* 15% weight loss for the control was observed in 72 h. The enzyme accelerated weight loss of the hydrogels may be a result of the surface erosion and the fast degradation of the oligopeptide chains.

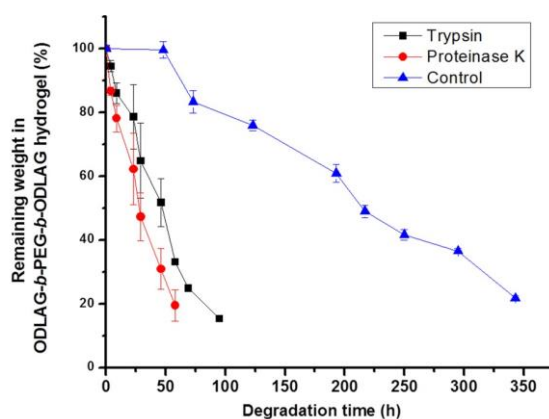


**Figure 2.14.** Weight loss profile of ODLAG<sub>6</sub>-*b*-PEG<sub>68</sub>-*b*-ODLAG<sub>6</sub> hydrogel with/without enzyme. Measurements were repeated five times for each enzyme and control sample.

## 2.4 Conclusions

In summary, a series of multi-responsive hydrogels composed of PEG tethered oligopeptides, was prepared with extraordinarily low synthetic complexity. The triblock system exhibited reversible and repeatable sol-to-gel and gel-to-sol transitions that can be triggered by heat and sonication, respectively. In addition, certain enzymes accelerated the breakdown of the bio-responsive hydrogels into sols. The ability to form hydrogels is shown to be dependent on the hydrophobic and hydrophilic balance and is dictated by the block length of the oligopeptide blocks, which is in turn easily controlled by reaction feed ratio. Detailed characterization studies indicated that hydrogelation may be driven by a combination of oligopeptide  $\beta$ -sheeting and a balance between PEG-PEG interactions and PEG-water interactions, with effects observed at the supramolecular, nano-, micro- and macro-scales. Moreover, the oligopeptide segments carry reactive allyl side chain groups, which have the potential to be further functionalized into intelligently-designed systems of increased complexity and functionality. This multi-responsive hydrogel system provides a potential platform for development of drug delivery vehicles, sensors, and smart devices.

CHAPTER III

SUPRAMOLECULARLY-KNITTED TETHERED OLIGOPEPTIDE/SINGLE-  
WALLED CARBON NANOTUBE ORGANOGELS\*

### 3.1 Introduction

Since being synthesized in the early 1990s,<sup>150</sup> carbon nanotubes (CNTs) have drawn significant interest due to their extraordinary optical, thermal, mechanical and electronic properties.<sup>151-154</sup> Single-walled carbon nanotubes (SWCNTs) are particularly intriguing, typified as one-atom-thick graphite lattices rolled into cylindrical nanostructures with a diameter range of 0.4-3 nm and varying chirality. SWCNTs have been extensively explored for a variety of applications, such as optical emitting devices,<sup>155</sup> flame-retardant coatings,<sup>156</sup> mechanical reinforcing materials,<sup>157</sup> flexible electronics,<sup>158</sup> sensors<sup>159</sup> and many others.<sup>160,161</sup> Recently, increasing attention has been given to the incorporation of SWCNTs in biological systems to take advantage of their near-infrared (NIR) responsive exothermicity properties<sup>162</sup> in drug delivery,<sup>163</sup> tissue engineering,<sup>164</sup> cancer diagnoses and therapy,<sup>165</sup> among other applications.

However, due to the extremely strong  $\pi$ - $\pi$  stacking and van der Waals interactions, large SWCNT bundles tend to be difficult to disperse homogeneously in common organic and aqueous solutions. This challenge imposes significant limitations on the use of SWCNTs after they have aggregated. With the help of prolonged

---

\* Reprinted (adapted) with permission from “Supramolecularly-knitted Tethered Oligopeptide/Single-walled Carbon Nanotube Organogels” by Zou, J.; He, X.; Fan, J.; Raymond, J. E.; Wooley, K. L., *Chem. Eur. J.* **2014**, 20, 8842-8847. Copyright 2014 Wiley-VCH.



sonication, SWCNTs can be dispersed in some solvents, though precipitation occurs soon thereafter.<sup>166</sup>

Two common approaches applied to the above dispersion problem include covalent modification of SWCNT surfaces and noncovalent adsorption of functional small molecules and polymers.<sup>167-171</sup> Noncovalent modification of SWCNTs is particularly attractive because the strategy preserves the intrinsic properties of SWCNTs without disruption to the electronic and optical responses of the system.<sup>172</sup> It has been demonstrated that SWCNTs interact with conjugated species, such as pyrene derivatives,<sup>173</sup> phthalocyanines,<sup>174</sup> porphyrins,<sup>175</sup> phenazine,<sup>176</sup> and thionine types of dyes,<sup>177</sup> based on  $\pi$ - $\pi$  stacking. Twelve-membered cyclodextrins<sup>178</sup> and select DNA sequences<sup>179</sup> have also been reported to allow structure-specific recognition of SWCNTs with specific surface structure due to host-guest supramolecular complexation. Compared with small molecule SWCNT stabilizers, functional polymers are quite efficient dispersants, due to an ability to wrap around SWCNTs, thereby, displacing and disrupting the van der Waals and  $\pi$ - $\pi$  interactions between aggregated SWCNTs. Different polymeric systems, including acrylates,<sup>180</sup> epoxy resins,<sup>181</sup> hydrocarbon polymers<sup>161</sup> and conjugated polymers,<sup>182-185</sup> have been developed for CNT dispersal in organic solvents. However, limited studies have been conducted using biodegradable polymers to disperse CNTs.<sup>179,186-189</sup>

Polypeptides with tunable sequences and secondary structures have been employed to noncovalently disperse CNTs in aqueous solutions.<sup>190,191</sup> By tuning the sequence and length of these polypeptide systems, differentiated binding affinity for

different types of SWCNTs could be realized.<sup>192</sup> Specifically, the secondary structure ( $\alpha$ -helix<sup>191,193</sup> and  $\beta$ -sheet<sup>194</sup> formation) of an intelligently-designed amphiphilic polypeptide system was reported to bind the surface of SWCNTs in aqueous solutions. However, the polypeptide-SWCNT dispersal remained primarily limited to sequences composed of 12-30 natural amino acids, with  $\pi$ - $\pi$  stacking between aromatic residues (derived from amino acids such as tyrosine, phenylalanine and histidine) on polypeptide and the SWCNT surface playing the most important role in the polypeptide dispersing capability. The dispersion of SWCNTs by nonaromatic peptides has not been reported. Typically, the synthesis of polypeptide dispersants with special sequences has required several steps of solid phase synthesis and has experienced technical challenges with production scale-up.<sup>29</sup> Compared with solid phase synthesis, ring opening polymerization (ROP) of *N*-carboxyanhydrides (NCA) provides a more effective, scalable and economic method for the preparation of high molecular weight polypeptides for SWCNT dispersion.<sup>189</sup>

Recently, our group reported a functional polypeptide-based organogelator, poly(ethylene oxide)-*block*-poly(DL-allylglycine) (PEG-*b*-PDLAG), containing a racemic allyl functional homopolypeptide block.<sup>68</sup> Gelation in high polar organic solvents was shown to be driven by supramolecular assembly of the PDLAG peptide segment into  $\beta$ -sheets. With  $\beta$ -sheet formation, hierarchical one-dimensional stacking of block copolymers then led to the construction of well-defined ribbon-like morphologies and, ultimately, gelation. The present work stems from the hypothesis that  $\beta$ -sheets

composed of allyl-rich PDLAG peptide domains would have a strong propensity for  $\pi$ - $\pi$  stacking with SWCNT surfaces.

It was anticipated that the diblock PEG-*b*-PDLAG would lead merely to dispersion of SWCNT, whereas our interest in this work was the creation of functional hybrid organogels reinforced by SWCNTs. Therefore, a new triblock cooligopeptide oligo(DL-allylglycine)-*block*-poly(ethylene oxide)-*block*-oligo(DL-allylglycine) (ODLAG-*b*-PEG-*b*-ODLAG) was designed to allow for binding to and bridging between SWCNTs. The ODLAG peptide  $\beta$ -sheets are shown to undergo noncovalent association with the SWCNTs, while also regulating assembly into hierarchically-ordered structures *via* peptide-peptide interactions between adjacent ODLAG-*b*-PEG-*b*-ODLAG-decorated SWCNTs. The triblock structure formed  $\beta$ -sheets and showed good ability to homogeneously disperse SWCNTs in DMF solution. With increased polymer concentration, the triblock-SWCNT composites resulted in fibrillar organogels. Compared with the ODLAG-*b*-PEG-*b*-ODLAG organogel without SWCNTs, the triblock-SWCNT composite organogels possess significantly increased stiffness as characterized by dynamic mechanical analysis (DMA). The triblock-SWCNT organogels were characterized at different length scales including scanning electron microscopy (SEM), transmission electron microscopy (TEM), confocal microscopy and atomic force microscopy (AFM). Interestingly, with disruption of the  $\beta$ -sheeting, the triblock could no longer disperse SWCNTs or form organogels. Based upon the hypothesis and results, this work has demonstrated a new and efficient strategy to disperse SWCNTs.

## 3.2 Experimental section

### 3.2.1 Materials

Ethyl acetate, n-hexane, tetrahydrofuran (THF), diethyl ether, *N,N*-dimethylformamide (DMF, anhydrous,  $\geq 99.8\%$ ), toluene, dichloromethane (DCM), dimethyl sulfoxide (DMSO), DL-allylglycine,  $\alpha$ -pinene, triphosgene, trifluoroacetic acid, isopropanol, methanol and single-walled carbon nanotube (SWCNT, product number: 704113) were purchased from Sigma-Aldrich Company (USA).  $\alpha,\omega$ -Diamino-terminated poly(ethylene oxide) ( $\text{NH}_2\text{-PEG}_{68}\text{-NH}_2$ ,  $M_n = 3000$  g/mol) was purchased from Rapp Polymere (Germany). All chemicals were used without further purification, unless otherwise noted.

### 3.2.2 Instrumentation

$^1\text{H}$  and  $^{13}\text{C}$  NMR spectra were recorded on a Varian Inova 300 spectrometer interfaced to a UNIX computer using VnmrJ software. Chemical shifts were referenced to the solvent resonance signals. ATR-FTIR spectra were recorded on an IR Prestige 21 system (Shimadzu Corp.) and analyzed using IRsolution v. 1.40 software. Raman spectroscopy was performed with a B&K Tek iRaman system operated with a 785 nm NIR stimulation source through a fiber optic cable (excitation & collection) while the samples remained in glass vials. Spectra were analyzed with Origin Pro 9.0.

Thermogravimetric analysis (TGA) was performed under Argon atmosphere using a Mettler-Toledo model TGA/SDTA851<sup>°</sup> (Mettler-Toledo, Inc., Columbus, OH), with a heating rate of 10  $^{\circ}\text{C}/\text{min}$ . Measurements were analyzed using Mettler-Toledo STAR<sup>°</sup> v. 7.01 software. Glass transition temperatures ( $T_g$ ) were measured by

differential scanning calorimetry (DSC) on a Mettler-Toledo DSC822<sup>®</sup>, with a heating rate of 10 °C/min. Measurements were analyzed using Mettler-Toledo STAR<sup>e</sup> v. 7.01 software. The  $T_g$  was taken as the midpoint of the inflection tangent, upon the second heating scan.

Dynamic mechanical analysis (DMA) was performed on a Mettler Toledo TT-DMA system. DMA measurements of the organogels in DMF were performed over 3 h in compression on a 3.2 mm thick, 10 mm diameter cylinder. Dynamic measurements were recorded over a range of 0.1 to 10 Hz at room temperature with static stress modulated to 10% compression and a dynamic force applied to provide  $\pm 5\%$  deformation. Kinetic data presented were obtained as a single exponential decay using Origin Pro 8.1 software. The gel strength was quantified by the evaluation of the compression storage modulus ( $E'$ ).

Transmission electron microscopy (TEM) images were collected on a JEOL 1200 EX operating at 100 kV and micrographs were recorded at calibrated magnifications using a SLA-15C CCD camera. Samples for TEM measurements were prepared as follows: 10  $\mu$ L of the dilute solution was deposited onto a carbon-coated copper grid, and after 2 min, the excess of the solution was quickly wicked away by a piece of filter paper. The samples were then negatively stained with 1 wt% phosphotungstic acid (PTA) aqueous solution. After 30 s, the excess staining solution was quickly wicked away by a piece of filter paper and the samples were left to dry under vacuum overnight.

Scanning electron microscopy (SEM) imaging was performed in JOEL JSM-6400 SEM operated at an acceleration voltage of 15 kV. The preparation of samples for SEM involved placing a drop of gel on a carbon film. The gel was then subjected to immediate freezing by liquid nitrogen, followed by being placed under high vacuum for 3 days. The surface of the gel was sputter coated with gold for 3 min under argon.

Atomic force microscopy (AFM) imaging was performed using a MFP-3D system (Asylum Research, Santa Barbara, CA) in tapping mode using standard tips (Vista Probes, T190-25; length (L), 225 mm, normal spring constant, 48 N m<sup>-1</sup>; resonance frequency, 190 kHz). The samples as DMF solutions were deposited onto freshly-cleaved mica and allowed to dry *in vacuo* before analyses. The average height and diameter values were determined by section analyses, using the IGOR Pro software package.

Confocal fluorescence images were taken using a FV 1000 system (Olympus) with a 10x objective (Olympus) and a 488 nm Argon laser excitation source. Emission was collected using a monochromator set to a 100 nm band pass (510 – 610 nm) and a photomultiplier tube. Image analysis was performed in Fluoview software (Olympus) with identical scan conditions and no image adjustment for the polypeptide-SWCNT gel and triblock polypeptide gels. A 1.1 gamma correction was used to enhance feature contrast after scaling image contrast intensity to minimum and maximum threshold set points of 1% above dark count and 1% below maximum counts for fluorescence of the SWCNT in DMF and dye in DMF samples. All differential interference contrast (DIC) images were adjusted for contrast. Slides were generated by lightly compressing the

gels between a cleaned glass microscope slide and a cleaned glass cover slip after dye addition. Samples were made from 1-SWCNT DMF gel, 1 DMF gel and SWCNTs in DMF. A stock solution of 1 mg/mL 5,6-FAM dye (Anaspec, Fremont, CA) in DMF was generated, which was then added to the samples at 1% by mass. Similarly, a reference sample of diluted stock solution (1% by mass) in DMF was made. Lifetime decays for the four samples were obtained by time correlated single-photon counting (TCSPC) by way of a fluorescence lifetime imaging system (PicoQuant LSM module for FV1000 system). Excitation occurred with a 405 nm ps laser (FWHM 50 ps) operated at 2.5 MHz. Emission lifetimes were calculated from single or double exponential decay tail-fitting beginning at 90% of total decay intensity (Origin Pro 9.0).

Sonication was performed in an ultrasonic homogenizer (maximum power, 150 W, 20 kHz, Model 150 V/T, Biologics, Inc.) equipped with a micro tip with a diameter of 3.81 mm, employing the power output of 30 W in the frequency of 20 kHz at room temperature.

### *3.2.3 Synthesis*

Synthesis of DL-Allylglycine NCA. The DL-allylglycine NCA monomer was prepared following the previously reported method. In a 250 mL two-neck flask, equipped with septum and pipet for nitrogen inlet and a condenser with a tubing connector that allows outlet flow through a base solution ( $\text{NaOH}_{(\text{aq})}$ ), DL-allylglycine (3.0 g, 26 mmol) was dissolved in 100 mL THF and triphosgene (6.4 g, 22 mmol) was added directly to the reaction flask. Then 9 mL  $\alpha$ -pinene was added and the reaction mixture was allowed to stir for 2.5 h at 50 °C, while being constantly flushed with a

stream of dry nitrogen. The crude product was concentrated and precipitated from hexane, recrystallized four times from ethyl acetate/hexane, and then dried *in vacuo*; yield: 1.4 g (46%) as a white needle-like crystal.  $^1\text{H}$  NMR (300 MHz,  $\text{CDCl}_3$ , ppm):  $\delta$  2.51 and 2.74 (m, 2H,  $\text{CH}_2$ ), 4.38 (m, 1H,  $\text{CH}$ ), 5.29 (m, 2H,  $\text{H}_2\text{C}=\text{CH}$ ), 5.74 (m, 1H,  $\text{H}_2\text{C}=\text{CH}$ ), 6.35 (br, 1H,  $\text{NH}$ ).  $^{13}\text{C}$  NMR (75 MHz,  $\text{DMSO-d}_6$ , ppm):  $\delta$  34.9, 56.9, 120.0, 131.4, 151.9, 171.0. FT-IR ( $\text{cm}^{-1}$ ): 3348, 3016, 2932, 1829, 1753, 1292, 922. HRMS: calculated  $[\text{M-H}]^-$  for  $\text{C}_6\text{H}_7\text{NO}_3$ : 140.0349, found: 140.0354.

Synthesis of ODLAG<sub>6</sub>-*b*-PEG<sub>68</sub>-*b*-ODLAG<sub>6</sub>. Into a flame-dried 25 mL Schlenk flask equipped with a stir bar and capped with a rubber stopper with a needle outlet connected to a tube filled with drying agent, DLAG-NCA (199.5 mg, 1.414 mmol) in dry DMF (10 mL) was injected. After being stirred at r.t. for 5 min,  $\text{NH}_2\text{-PEG}_{68}\text{-NH}_2$  (368.7 mg, 0.1229 mmol) in dry DMF (5 mL) was injected *via* a dry syringe. The reaction mixture was stirred at r.t. (stir rate = 340 rpm) under continuous nitrogen flow (100 mL/min) for 12 h. The reaction mixture was then precipitated into 80 mL diethyl ether twice. The triblock was collected by filtration and dried *in vacuo* at r.t. yield 285.0 mg (50%) as a white powder.  $^1\text{H}$  NMR (300 MHz,  $\text{DMSO-d}_6$ , ppm):  $\delta$  2.32 (m, 2H,  $\text{CHCH}_2\text{CHCH}_2$ ), 3.50 (br, 2H,  $\text{OCH}_2$ ) 4.32 (m, 1H,  $\text{NHCHCO}$ ), 5.01 (m, 2H,  $\text{CH}_2\text{CHCH}_2$ ), 5.68 (m, 1H,  $\text{CH}_2\text{CHCH}_2$ ), 8.10 (br, 1H,  $\text{COCHNH}$ ).  $^{13}\text{C}$  NMR (75 MHz,  $\text{DMSO-d}_6$ , ppm):  $\delta$  36.3, 52.1, 69.8, 117.5, 134.1, 170.7. FT-IR ( $\text{cm}^{-1}$ ): 3672-3402, 3284, 3075, 2870, 1677, 1626, 1526, 1101, 696. DSC:  $T_g = -38\text{ }^\circ\text{C}$ ,  $T_c = 9\text{ }^\circ\text{C}$ ,  $T_m = 40\text{ }^\circ\text{C}$ ,  $T_g = 77\text{ }^\circ\text{C}$ . TGA in Argon: 25-303  $^\circ\text{C}$ : 5% mass loss, 303-425  $^\circ\text{C}$ : 74% mass loss, 423-800  $^\circ\text{C}$ : 4% mass loss, 17% mass remaining above 800  $^\circ\text{C}$ .



### 3.3 Results and discussions

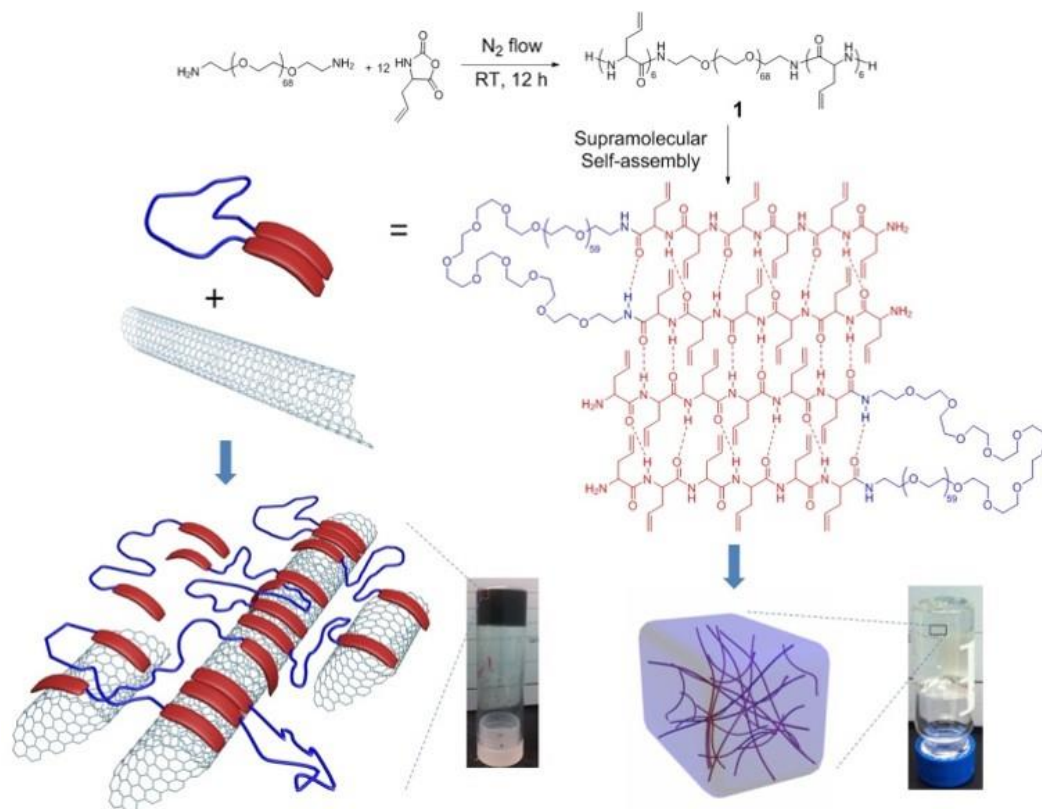


**Figure 3.1.** Graphic illustration of  $\text{ODLAG}_6\text{-}b\text{-PEG}_{68}\text{-}b\text{-ODLAG}_6$  based organogels with/without SWCNT incorporation.

With our broad interest in the creation of original well-defined functional polymer-based nanomaterials having simple molecular design and synthetic feasibility, for fundamental studies and biomedical applications, we began investigation into the preparation of A-B-A type amphiphilic triblock copolypeptides having broadly modifiable allyl side chains. Shvartzman-Cohen *et al.* reported an amphiphilic A-B-A type triblock copolymer, poly(ethylene oxide)<sub>100</sub>-*b*-poly(propylene oxide)<sub>65</sub>-*b*-

poly(ethylene oxide)<sub>100</sub>, (PEG<sub>100</sub>-*b*-PPG<sub>65</sub>-*b*-PEG<sub>100</sub>) as an efficient SWCNT disperser in aqueous solution *via* noncovalent interaction between polymers and SWCNT surfaces, and further shaped the inter-nanotube potential against aggregation.<sup>195</sup> We had expected that a triblock structure having an inversion of the positioning of the amphiphilic units, to a structure with peptide-based hydrophobic end blocks capable of binding to the surface of hydrophobic SWCNT and tethered by a central polar segment could disperse SWCNT in polar solvents and, further, lead to gelation properties. A ODLAG-*b*-PEG-*b*-ODLAG triblock structure 1 was, therefore, synthesized *via* facile ring opening polymerization of DL-allylglycine NCA by using  $\alpha,\omega$ -diamino terminated poly(ethylene oxide) (NH<sub>2</sub>-PEG<sub>68</sub>-NH<sub>2</sub>) as the macroinitiator (Fig. 3.1).

Our recent study found that by using normal Schlenk techniques, NCA ROPs can be conducted on a large scale with the rate of polymerization being controlled by a straightforward nitrogen flow method.<sup>57</sup> For the current investigation, the required amounts of allyl functional NCA monomers and diamino macroinitiator were dissolved in anhydrous DMF and the ROP was allowed to proceed up to 12 h at room temperature, under a continuous nitrogen flow (flow rate = 100 mL/min). The conversion of the monomer was monitored by measuring the intensity of the DLAG NCA anhydride peak at 1788 cm<sup>-1</sup> using attenuated total reflectance-Fourier transform infrared spectroscopy (ATR-FTIR). After monomer conversion of > 95% was obtained, the polymerization was quenched by pouring the viscous reaction mixture into diethyl ether and dried under vacuum to yield the targeted triblock structure as a white powder. Similar to previously reported DLAG NCA polymerization, the A-B-A triblock had a tendency to form a gel

in DMF at high conversion. The detailed structures, compositions and thermal properties of the triblock structures were determined by using  $^1\text{H}$  NMR,  $^{13}\text{C}$  NMR, ATR-FTIR, DSC and TGA analyses. The processing capability of **1** was explored in terms of secondary structures, supramolecular interaction with SWCNTs, gelation behavior and mechanical properties of organogels with/without SWCNTs incorporated. The capability of **1** to form organogels in different solvents was explored and the properties of the gels in DMF were investigated comprehensively (Table 3.1). The triblock structure could be dissolved in polar organic solvents (DMF, DMSO, methanol, TFA and chloroform), but not in apolar organic solvents or water, indicating that the solvation properties were dominated by the oligopeptide end block properties. With an increase in concentration (50 mg/mL) the **1** DMF solution tended to form organogels (r.t., 1~5 h).

**Table 3.1.** Solubility studies of SWCNT, ODLAG<sub>6</sub>-PEG<sub>68</sub>-ODLAG<sub>6</sub> (**1**) and **1**-SWCNT composites in different organic solvents.

	SWCNT <sup>a</sup>	<b>1</b> <sup>b</sup>	<b>1</b> -SWCNT composites <sup>c</sup>
DMF	Suspension	Gel	Gel
DMSO	Suspension	Gel	Solution with precipitates
Methanol	Suspension	Gel	Solution with precipitates
CHCl <sub>3</sub>	Suspension	Solution	Suspension
TFA	Suspension	Solution	Suspension
Toluene	Suspension	Suspension	Suspension
Ethyl acetate	Suspension	Suspension	Suspension
Hexane	Suspension	Suspension	Suspension
THF	Suspension	Suspension	Suspension
Isopropanol	Suspension	Suspension	Suspension
Water	Suspension	Suspension	Suspension

<sup>a</sup> The concentration of SWCNT was 0.5 mg/mL in each solvent.

<sup>b</sup> The concentration of **1** was 50 mg/mL in each solvent.

<sup>c</sup> The concentration of **1** was 50 mg/mL with 0.5 mg/mL SWCNTs. The solutions/suspensions were kept at room temperature for 24 h before observations were made.

Gelation was driven by supramolecular assembly of  $\beta$ -sheets into well-defined fiber-like nanostructures, further generating a 3-D networks through longer-range interactions. This result is similar to that observed for the mPEG<sub>45</sub>-*b*-ODLAG<sub>12</sub> diblock copolymer organogelators reported previously. The triblock **1** DMF organogel also responded to sonication stimulus, rapidly obtaining a sol state (20 s sonication). SWCNTs (0.5 mg/mL) incorporated into solutions of **1** (50 mg/mL) formed homogeneous SWCNT DMF solutions (2 min sonication). After standing (r.t., 5 h), self-supported uniform SWCNTs DMF gels formed. It was also found that the ability of **1** to undergo dispersion and gelation with SWCNTs changed with different organic solvents (Table 3.1). Compared with DMF, similar SWCNT loading into DMSO or methanol solutions resulted in SWCNT precipitates that did not gel with time (r.t., 24 h).

**Table 3.2.** Critical gelation concentrations ( $C_{gel}$ ) of ODLAG<sub>6</sub>-PEG<sub>68</sub>-ODLAG<sub>6</sub> (**1**) and **1**-SWCNT composites in different organic solvents.

	DMF	DMSO	Methanol
<b>1</b>	10 mg/mL	35 mg/mL	50 mg/mL
<b>1</b> -SWCNT composites <sup>a</sup>	25 mg/mL	Not detected	Not detected

<sup>a</sup> The concentration of SWCNT was 0.5 mg/mL in each solvent.

The critical gel concentrations ( $C_{gel}$ , Table 3.2) were obtained by preparing different polymer concentrations in DMF, DMSO and methanol (test tube inversion method, r.t.), with DMF requiring the lowest concentration for gelation. With the incorporation of SWCNTs, the  $C_{gel}$  of **1** in DMF increased from 10 mg/mL to 25

mg/mL, while the  $C_{\text{gel}}$  in DMSO was not observed even at 100 mg/mL. The increase of  $C_{\text{gel}}$  after SWCNT incorporation indicates strong noncovalent interaction between the SWCNTs and oligopeptide segments, resulting in a decrease in available peptide-peptide interactions. However, while TFA was used as solvent, **1** could be totally dissolved unimolecularly by disrupting the supramolecular secondary structure. The SWCNT could not be homogeneously suspended in TFA solutions of **1**, which indicated that the  $\beta$ -sheeting is a critical component of both gelation and SWCNT dispersion.

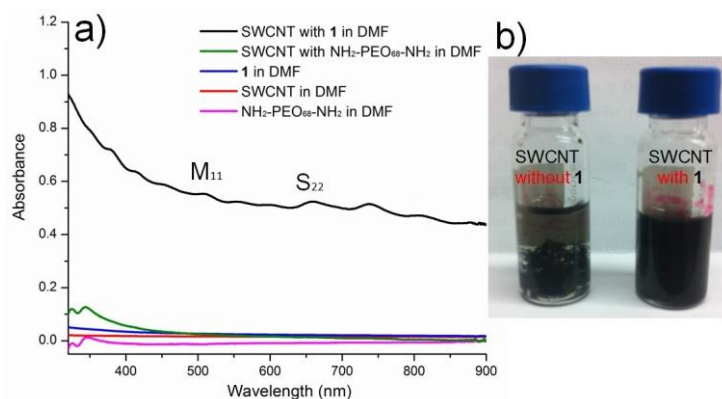


**Figure 3.2.** a) UV-vis spectra of SWCNT in DMF with **1** (black); SWCNT in DMF with  $\text{NH}_2\text{-PEG}_{68}\text{-NH}_2$  (green), **1** in DMF (blue), SWCNT in DMF without **1** (red) and  $\text{NH}_2\text{-PEG}_{68}\text{-NH}_2$  in DMF (pink); b) Images of SWCNT in DMF with/without **1**.

The dispersion ability of SWCNTs by  $\text{ODLAG}_6\text{-}b\text{-PEG}_{68}\text{-}b\text{-ODLAG}_6$  was characterized by using UV-vis spectroscopy. SWCNT (0.20 mg) was suspended into DMF (1 mL, r.t., 2 min sonication) resulting in SWCNT precipitation within 2 min after sonication (Fig. 3.2). In comparison, **1** (5 mg) was added to a similar SWCNT DMF suspension (1 mL, at 0.2 mg/mL, 2 min sonication) and a homogeneous SWCNT

dispersion was obtained. The solution was stable (1 week in r.t.) and no precipitation was observed. UV-vis absorbance spectra were measured after five-fold dilution of the 1-SWCNT DMF solution. As a control, the ODLAG<sub>6</sub>-PEG<sub>68</sub>-ODLAG<sub>6</sub> in DMF (1 mg/mL) showed very low absorbance in UV-Vis. In the absorbance spectrum of 1-SWCNT composites, the second interband transitions ( $S_{22}$ ) for semiconducting SWCNTs can be found from 600-800 nm, and the absorption band around 550 nm can be assign to the first interband transitions ( $M_{11}$ ) of metallic SWCNTs. The dispersion ability of NH<sub>2</sub>-PEG<sub>68</sub>-NH<sub>2</sub> was also measured at the concentration of 1 mg/mL, indicating that without the aid of the oligopeptide segments, the PEG block could not disperse SWCNTs in DMF.

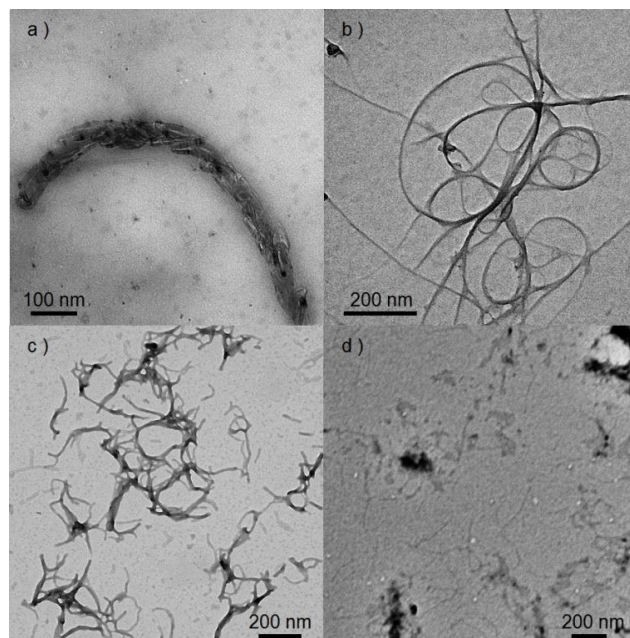


**Figure 3.3.** TEM images of a) hierarchical assembly of 1-SWCNT composites in SWCNT organogel without staining; b) SWCNT; c) 1 DMF organogel with PTA stain; d) 1 DMF organogel without staining.

The nanoscopic supramolecular self-assembly of 1-SWCNTs composites was characterized by TEM (Fig. 3.3a and Fig. 3.4). SWCNTs interacting with the triblock structures exhibited higher contrast and increased diameter (ca. 6.4 nm, Figure 2a) when compared with the SWCNT without oligopeptide association (ca. 3.2 nm, Fig. 3.3b). Upon interaction with 1, the bent SWCNT fibers exhibited much more flexible morphology and had a tendency to form quasi-aligned aggregates. Hierarchical nanoscopic structures could also be observed in the 1-SWCNT composites (Fig. 3c). “Knitted” fibers, have spacing between SWCNTs that indicate several polymers associating and encapsulating, further reinforce the function of the  $\beta$ -sheets as both SWCNT binding and self-binding. The allyl-rich segments in the triblock nanoribbon may also serve as conjugation-rich domains which interact with the sidewalls of SWCNTs resulting in both plaquing ( $\beta$ -sheets driven) and  $\pi$ - $\pi$  stacking effects contributing to the triblock SWCNT interactions. By observation (Fig. 3.4) the 1 supramolecular fibril assemblies tend to take a helical conformation, wrapping around the SWCNTs, which suggests that a soluble PEG “shell” disperses the SWCNTs, and is in keeping with peptide driven polymer-SWCNT interactions. In contrast, control studies of the SWCNT or organogel, each independently, gave much less interesting features. A cylindrical morphology was observed in 1 DMF organogel with phosphotungstic acid (PTA) staining. The width of the cylinder was  $\sim 8.8$  nm and the length  $\sim 100$ -300 nm (Fig. 3.3c). Without PTA staining, the cylinders could only be observed sparingly by TEM imaging (Fig. 3.3d).

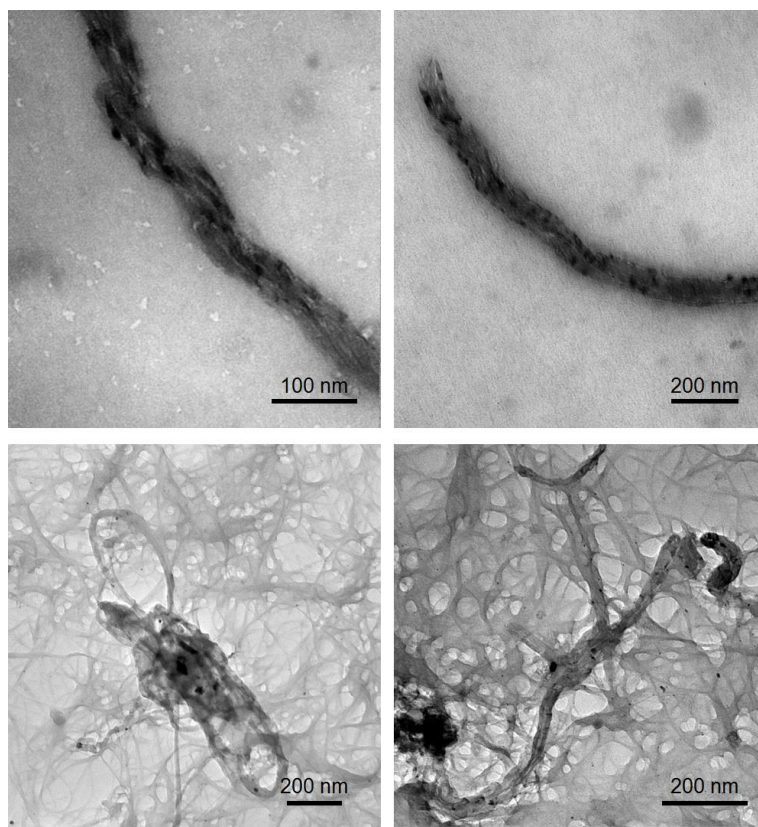


**Figure 3.4.** TEM images of hierarchically-assembled structures in 1-SWCNT composites.

The gels were also characterized at the meso scale (SEM, AFM and confocal microscopy). Porous network structures could be observed in both SEM and AFM characterizations (Fig. 3.5, Fig. 3.6). Dye doping of the 1 and 1-SWCNT gels indicated a greater homogeneity within the gel on addition of the SWCNTs (confocal and fluorescence life-time imaging, Fig. 3.7, Fig. 3.8).



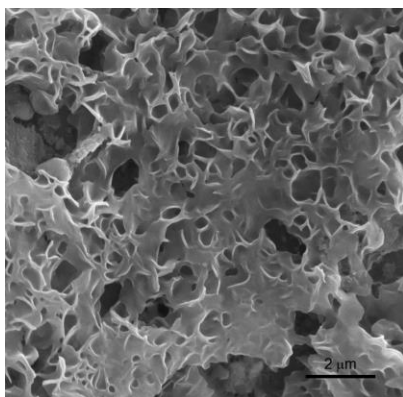


**Figure 3.5.** SEM image of lyophilized 1-SWCNT DMF gels.

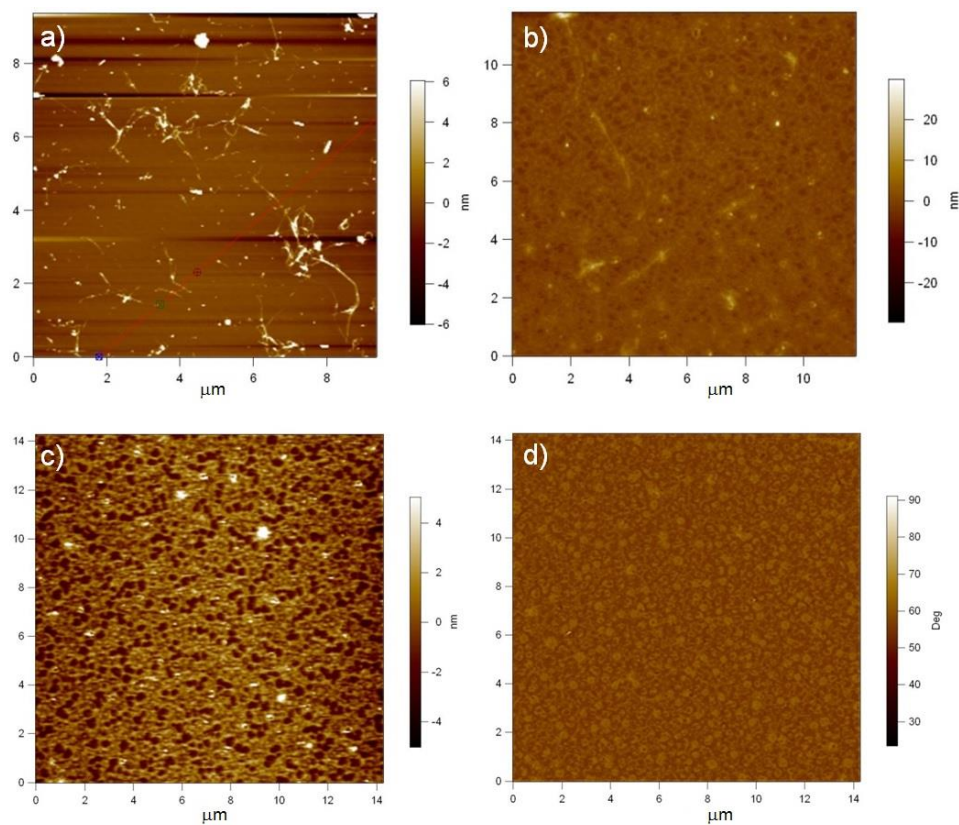


**Figure 3.6.** AFM images of a) height image of SWCNT after deposition onto freshly-cleaved mica from a solution in DMF and drying *in vacuo*; b) height image of 1-SWCNT composite after spin coating onto mica from the DMF gel state and drying *in vacuo*; c) height image of 1 after spin coating onto mica from the DMF gel state and drying *in vacuo*; d) phase image of the sample from c).

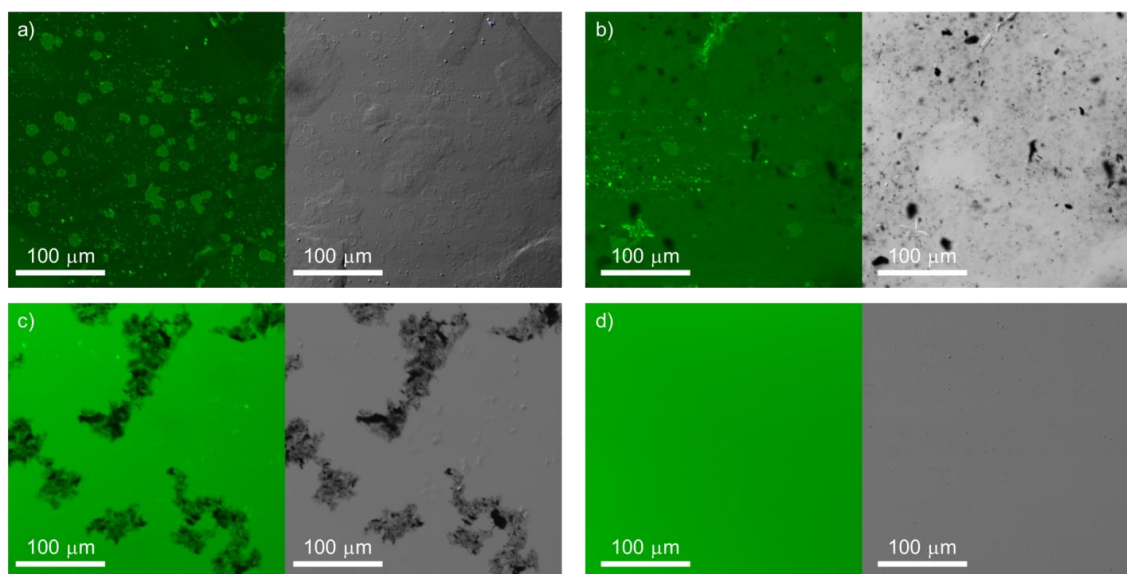


**Figure 3.7.** Confocal and differential interference contrast imaging of a) triblock 1 DMF gel; b) 1-SWCNT DMF gel; c) SWCNTs in DMF; d) DMF 5,6-FAM dye solution.

Microdomains of high concentration aggregates (*ca.* 10  $\mu\text{m}$  bright spots, Fig. 3.7) were observed for both gel systems, however, the 1-SWCNT gel expresses a ten-fold lower density of such species. The emissivity of the main-phase in the 1-SWCNT gel is also increased with respect to the triblock 1 gel under identical imaging conditions. Observation of the SWCNTs in DMF with 5,6-FAM dye displays no emission enhancement near the SWCNT aggregates, indicating that the presence of SWCNTs alone does not give rise to the main-phase emission increase. Taken together, these observations indicate that the 1-SWCNT gel is more homogeneous than the triblock 1 gel alone at the micro/meso scale.

A small amount of quenching ( $\tau$  decrease) was observed in the SWCNT and 5,6-FAM dye solution when compared with the dye solution (Fig. 3.8). This quenching is

reasonable given that SWCNTs are broadband photon absorbers and energy transfer distance requirements for a fraction of the excited dye to the SWCNT will be met. These profiles can be taken as characteristic in representing the sol phase signal for the 5,6-FAM dye with and without SWCNTs and possess total decay to <1% initial intensity completed in the 0 to 20 ns regime.

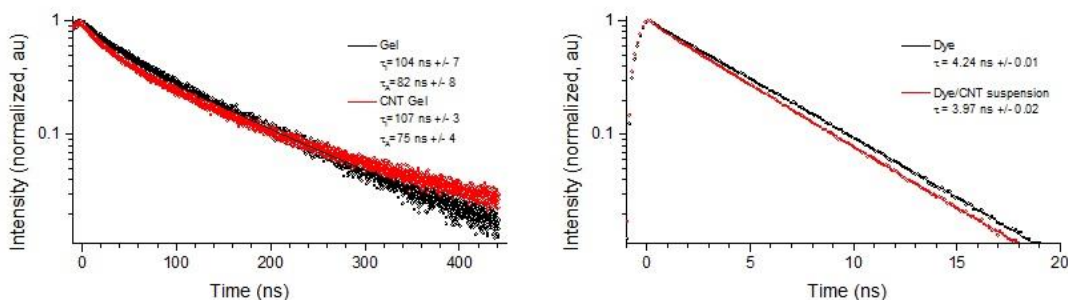


**Figure 3.8.** Emission decay profiles for 5,6-FAM dye in the presence of DMF (left, black), SWCNT DMF (left, red), 1 DMF gel (right, black), 1-SWCNT DMF gel (right, red).

While this same effect can be observed in the first 20 ns of the triblock 1 and 1-SWCNT DMF gels, the majority of the decay was observed in the form of long-lived emission where dye-SWCNT FRET is not occurring. Looking just at this region, it is clear that the 1-SWCNT gel possesses a much longer tail emission than does the 1 gel. Given that the rate of emission for dyes in sol-like environments is much shorter, this tail region can be taken as the signal from gel-like environments. Recognizing the relationship between emission life-time and non-radiative relaxation process (*e.g.* solvent collisions) of  $\tau = f(knr^{-1})$ , it is clear that the 1-SWCNT gel is providing a much

more protected environment for the dye species. Specifically, one in which solvent mobility is suppressed and a greater extent of crosslinking and matrix stiffening is occurring.

Characterization by FT-IR spectroscopy was conducted to investigate the secondary structure and the binding between **1** and SWCNTs (Fig. 3.9 and 3.10). Signatures of the  $\beta$ -sheet secondary structure for **1** were observed at  $1670\text{ cm}^{-1}$  and  $1620\text{ cm}^{-1}$  (both in amide I), in combination with a peak at  $1520\text{ cm}^{-1}$  (amide II). The spectra of **1** and **1**-SWCNT composites were almost identical, as the SWCNT did not present peaks in these frequency ranges, which suggests that the supramolecular structure of the oligopeptide gelator was unperturbed<sup>196</sup> by the SWCNTs.

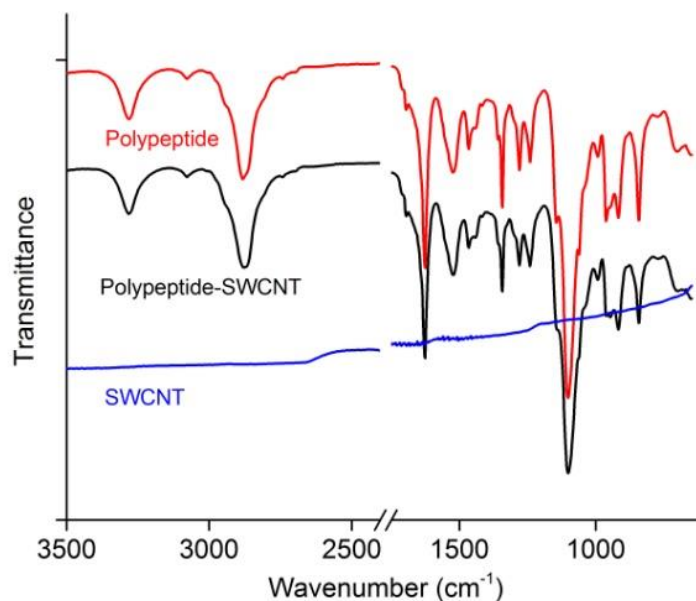


**Figure 3.9.** FT-IR spectra of dried **1**, **1**-SWCNT composites and SWCNT.

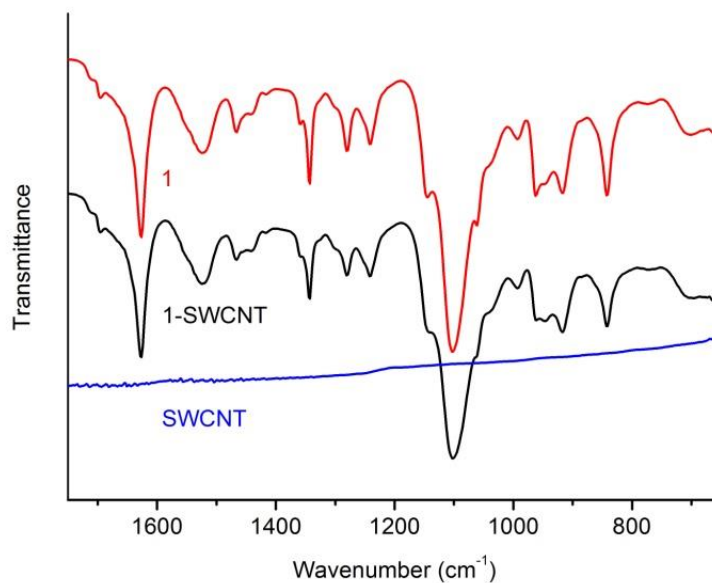


**Figure 3.10.** Expanded amide region from FT-IR spectra of dried 1, 1-SWCNT composites and SWCNT.

Raman spectroscopy measurements also indicated that the triblock structure could disperse SWCNTs in DMF solutions as well as in DMF gels without changing the structure of the SWCNTs (Fig. 3.11). The D band  $\sim 1300\text{ cm}^{-1}$  and G band  $\sim 1600\text{ cm}^{-1}$  of 1-SWCNT gels and 1-SWCNT solutions are almost identical to the pristine SWCNT in a DMF suspension. Compared with the SWCNT DMF suspension, the significantly increased G-band intensity with respect to the D-band intensity in the 1-SWCNT gel indicates a decrease in disruption of  $\pi$ -rich lattice (SWCNT-SWCNT interactions), further confirming the dispersive capability of the oligopeptide triblock.

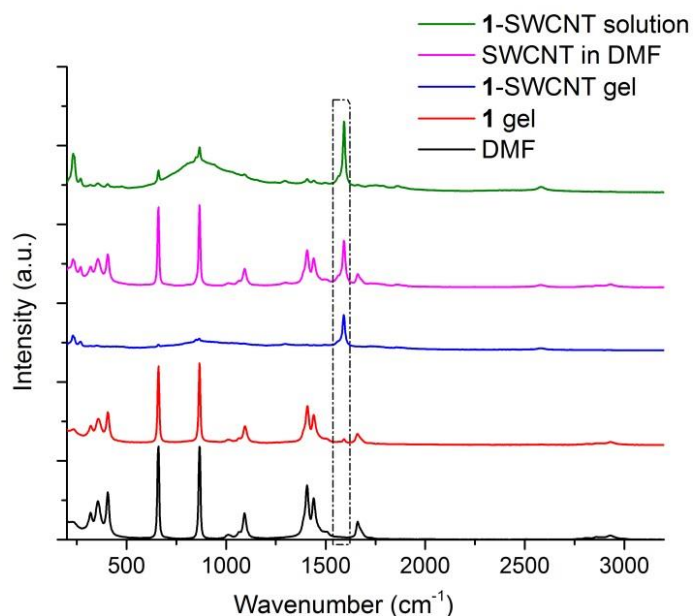


**Figure 3.11.** Raman spectra of triblock 1 DMF gel (50 mg/mL, red line), 1-SWCNT gel (50 mg/mL polymer with 2 wt% SWCNT loading, blue line), SWCNT in DMF suspension (pink line), 1-SWCNT solution (5 mg/mL polymer with 2 wt% SWCNT loading, green line).

The thermogravimetric analyses (TGA) were conducted to measure the mass loss of 1-SWCNT composites, 1 and SWCNT (Fig. 3.12). The 1-SWCNT composites exhibited two decompositions at 300-400 °C and at 400-650 °C, which can be attributed to the decomposition of 1 (75.2% mass loss at 300-425 °C) and SWCNTs (84.1% mass loss at 400-660 °C), respectively.

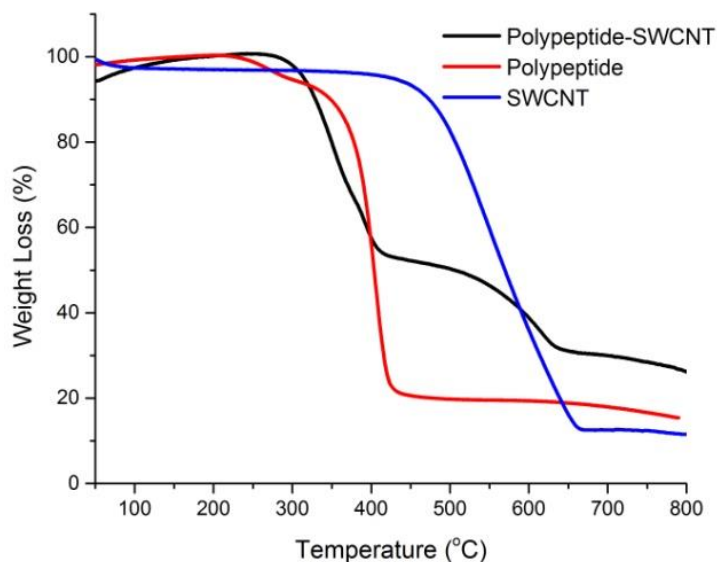


**Figure 3.12.** TGA measurements of dried 1, 1-SWCNT composites and SWCNT.

The mechanical properties of 1-SWCNT DMF gels were characterized by DMA. With 1.5 wt% incorporation of SWCNTs, the 1-SWCNT composites DMF gel (50 mg/mL) had a storage modulus ~400 kPa, (Fig. 3.13) which is >2 orders-of-magnitude greater than the 1 gel without SWCNT. The 1 DMF gel with same concentration (50 mg/mL) was too soft to be measured by DMA (storage modulus < 1 kPa). Given the evidence for high dispersion of SWCNTs in this system, this result was expected as the SWCNTs provide reinforcement to the gel network through exceptionally strong SWCNT-polymer binding. The triblock 1 DMF gel (conc. = 50 mg/mL) was crushed during the measurements, which indicate the storage modulus ( $E'$ ) of the DMF gel without SWCNT incorporation, usually below 1 kPa.



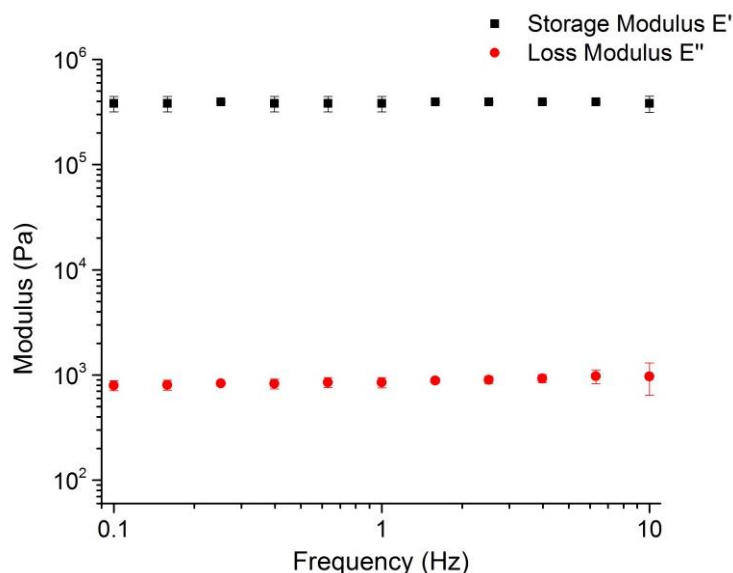


**Figure 3.13.** (a) Moduli of organogels from ODLAG<sub>6</sub>-PEG<sub>68</sub>-ODLAG<sub>6</sub> SWCNT gel (50 mg/mL, with 1.5 wt% SWCNT incorporation) as a function of frequency conducted by DMA.  $E'$  and  $E''$  indicate storage and loss modulus, respectively.

### 3.4 Conclusions

In conclusion, single-walled carbon nanotubes were efficiently dispersed in a novel A-B-A type triblock network, with low compositional and structural complexity, being based upon a hydrophilic PEG middle block and two hydrophobic racemic synthetic oligopeptide end segments. Detailed characterization studies indicated that the supramolecular self-assembly of  $\beta$ -sheets in the oligopeptide blocks form one dimensional stacked nanoribbons, in which allyl-rich ODLAG peptide domains have strong propensity for  $\pi$ - $\pi$  stacking with SWCNT surfaces, and consequently, efficiently separated and dispersed SWCNTs in organic solvent. The ODLAG peptide  $\beta$ -sheets could both noncovalently associate with the SWCNTs and assemble peptide-coated nanotubes into hierarchically-ordered structures *via* peptide-peptide interactions.



Despite these structures manifesting on the nanoscale, micro/mesoscale homogeneity was increased in the composite gels when compared to the triblock gel alone. With the incorporation of SWCNTs the mechanical properties of triblock-based organogels increased greatly, further displaying a dispersed (not merely encapsulated) state in the gel matrix. This work provides an interesting strategy that uses secondary structure control to stabilize SWCNTs, allowing for the efficient noncovalent incorporation of SWCNTs in the polymeric matrix without disrupting the band-structure of the SWCNTs (Raman). Moreover, sonication-responsive properties, enhanced mechanical properties and the presence of known biodegradable moieties enable further study and potential applications in sensor design, construction of adaptive materials and controlled release systems.

## CHAPTER IV

### REVERSIBLE PHOTO-PATTERNING OF SOFT CONDUCTIVE MATERIALS VIA SPATIALLY-DEFINED SUPRAMOLECULAR ASSEMBLY\*

#### 4.1 Introduction

The recent five years have witnessed the development of reversible photo-printing technologies, which include pioneering work to apply reversible covalent bond exchange reactions on functionalized surfaces, for light-healable coatings, repairable microarray technologies, patterned synthetic biomaterials, among others.<sup>197-199</sup> Nevertheless, the requirement on initial surface functionalization may complicate the process and limit the choice of available substrates. Being able to circumvent this complication, supramolecular assembly *via* noncovalent interactions has been applied in patterning through photo-triggered molecular assembly and subsequent sol-gel transitions, as the assembly process can occur without reliance on reactive functional groups on substrates.<sup>15,200,201</sup> In addition, supramolecular assembly usually possesses reversibility and stimuli-responsiveness, and, therefore, is a competitive approach to develop smart and reprocessable materials.<sup>202</sup>

Inspired by the reversible printing techniques and advantages of supramolecular assembly outlined above, we designed a new strategy that integrates conductive materials into stimuli-responsive gelators for rapid and reversible construction of

---

\* Reprinted (adapted) with permission from “Reversible Photo-patterning of Soft Conductive Materials *via* Spatially-defined Supramolecular Assembly” by He, X.; Fan, J.; Zou, J.; Wooley, K. L., *Chem. Commun.* **2016**, 52, 8455-8458. Copyright 2016 The Royal Society of Chemistry.

conductive soft materials with spatiotemporal definition *via* supramolecular assembly. This strategy was created as an approach to the current challenge to print reprocessable and rewritable conductive materials, as previous photo-patterning process typically relies on irreversible, and thus ‘dead’ reactions.<sup>203,204</sup> In this design, it was expected that a cascading series of events would occur, by which a photo-thermal conductive material would absorb light and generate heat, to be absorbed by a thermo-responsive hydrogelator, resulting in a triggered supramolecular assembly process and affording conductive, patterned, flexible materials. Based upon the demonstration of this strategy reported herein, a broad scope of applications can be anticipated, including patternable and flexible conductive materials with various dimensions, injectable and near IR curable hydrogels for bioelectronics or tissue engineering, and 3D printing materials for permanent or temporary layers.

## **4.2 Experimental section**

### *4.2.2 Instrumentation*

<sup>1</sup>H and <sup>13</sup>C NMR spectra were recorded on a Varian Inova 500 spectrometer interfaced to a UNIX computer using VnmrJ software. Chemical shifts were referenced to the solvent resonance signals. Attenuated total reflection Fourier transform infrared spectroscopy (ATR-FTIR) spectra were recorded on an IR Prestige 21 system (Shimadzu Corp.) and analyzed using IRsolution v. 1.40 software. Ultraviolet visible spectroscopy (UV/Vis) absorption measurements were made using a UV-2550 system (Shimadzu Corp.). Measurements were performed in nanopure water in cuvettes with path lengths of 1 cm. Thermogravimetric analysis (TGA) was performed under argon atmosphere

using a Mettler Toledo model TGA/DSC 1 (Mettler Toledo), with a heating rate of 10 °C/min. Measurements were analyzed using Mettler Toledo STAR<sup>e</sup> v. 7.01 software. Glass transition temperatures ( $T_g$ ) were measured by differential scanning calorimetry (DSC) on a Mettler Toledo DSC822<sup>®</sup>, with a heating rate of 5 °C/min and a cooling rate of 5 °C/min. Measurements were analyzed using Mettler Toledo STAR<sup>e</sup> v. 7.01 software. The  $T_g$  was taken as the midpoint of the inflection tangent, upon the third heating scan. Dynamic mechanical analysis (DMA) was performed on a Mettler Toledo TT-DMA system. DMA measurements of the hydrogels were performed through compression on a 3.3 mm thick, 10 mm diameter cylinder. Dynamic measurements were recorded over a range of 0.1 to 10 Hz at room temperature with 5% compression and a dynamic force applied to provide  $\pm 5\%$  deformation. Kinetic data presented were obtained as a single exponential decay using Origin Pro 8.1 software. Transmission electron microscopy (TEM) images were collected on a JEOL 1200 EX operating at 100 kV and micrographs were recorded at calibrated magnifications using a SLA-15C CCD camera. Samples for TEM measurements were prepared as follows: 10  $\mu$ L of the dilute solution was deposited onto a carbon-coated copper grid, and after 2 min, the excess of the solution was quickly wicked away by a piece of filter paper. Some of the indicated samples were then negatively stained with 1 wt% phosphotungstic acid (PTA) aqueous solution. After 30 s, the excess staining solution was quickly wicked away by a piece of filter paper and the samples were left to dry under vacuum overnight. The widths of the nanotubes were obtained by counting multiple ( $> 5$ ) tubes at 100 positions in the TEM images, an average value with standard deviation for a sample was calculated

accordingly. Scanning electron microscopy (SEM) imaging was performed in JOEL JSM-6400 SEM operated at an acceleration voltage of 15 kV. The preparation of samples for SEM involved placing a drop of hydrogel on a carbon thin film. The gel was then subjected to immediate freezing by liquid nitrogen, followed by lyophilization for 3 days. The surface of the resulting aerogel was sputter coated with gold for 3 min under argon before imaging. Sonication was performed in an ultrasonic homogenizer (maximum power, 150 W, 20 kHz, Model 150 V/T, Biologics, Inc.) equipped with a micro tip with a diameter of 3.81 mm, employing the power output of 30 W in the frequency of 20 kHz at room temperature. Photo-triggered sol-to-gel transition was performed through irradiation from a 532 nm continuous wave diode-pumped solid-state laser (250 mW). Heat-pressing was performed using a hydraulic hot-press 3912 system (Carver, Inc.), composite films were compressed with a force of 4.5 metric tons under 80 °C for 10 min. Four-point probe measurements were done with an Agilent Digital Multimeter (Agilent Technology) with the tip spacing set at 1.6 mm. The average electrical conductivity values were obtained by measuring four different locations on the same film sample after hot-press. Conductivities were calculated according to  $\sigma = I \cdot C^{-1} V^{-1} t^{-1}$ , where V and I were obtained from the digital multimeter, C is a correction factor related the film diameter<sup>205</sup>, and t is the film thickness measured by a micrometer at multiple positions (> 5) of a film.

#### 4.2.1 Materials

Ethyl acetate, *n*-hexane, tetrahydrofuran (THF), diethyl ether, *N,N*-dimethylformamide (DMF, anhydrous, ≥ 99.8%), trifluoroacetic acid (TFA),  $\alpha$ -pinene,

triphosgene, and single-walled carbon nanotube (SWCNT, product number 724777, prepared by CoMoCAT<sup>®</sup> Catalytic Chemical Vapor Deposition (CVD) Method, 90% carbon and 10% non-carbon composition,  $\geq 80.0\%$  carbon as SWCNT, diameter 0.7-1.4 nm, median length 1.10  $\mu\text{m}$ ) were purchased from Sigma-Aldrich Company (USA). DL-Allylglycine was received from Chem-Impex International, Inc. (USA).  $\alpha$ -Methoxy- $\omega$ -amino polyethylene glycol (product number: 122000-2,  $M_n = 2000$  g/mol) was purchased from Rapp Polymere (Germany). All chemicals were used without further purification, unless otherwise noted. Nanopure water (18  $\text{M}\Omega \cdot \text{cm}$ ) was acquired by means of a Milli-Q water filtration system, Millipore Corp (USA).

#### 4.2.3 Synthesis

**Synthesis of DLAG-NCA monomer.** DL-Allylglycine (10.0151 g, 86.99 mmol) and triphosgene (14.5318 g, 48.97 mmol) were stirred in a mixed solvent of dry THF (300 mL) and  $\alpha$ -pinene (34 mL) for 2.5 h at 50  $^{\circ}\text{C}$  under  $\text{N}_2$ . The solution was concentrated, then precipitated twice into hexane, recrystallized twice from ethyl acetate/hexane, and dried under vacuum; which gave a white needle-like solid in a yield of 4.744 g (38.6%).  $^1\text{H}$  NMR (500 MHz,  $\text{CDCl}_3\text{-d}$ ,  $\delta$ ): 2.53 and 2.72 (m, 2 H,  $\text{CH}_2$ ), 4.40 (m, 1 H, CH), 5.28 (m, 2 H,  $\text{H}_2\text{C}=\text{CH}$ ), 5.75 (m, 1 H,  $\text{H}_2\text{C}=\text{CH}$ ), 6.52 (br, 1 H, NH) (Fig 4.1).  $^{13}\text{C}$  NMR (125 MHz,  $\text{CDCl}_3\text{-d}$ ,  $\delta$ ): 36.0 ( $\text{CHCH}_2\text{CH}$ ), 57.3 ( $\text{NHCH}(\text{CO})\text{CH}_2$ ), 121.61 ( $\text{CH}=\text{CH}_2$ ), 130.0 ( $\text{CH}_2\text{CH}=\text{CH}_2$ ), 152.5 ( $\text{NHCOO}$ ), 168.9 ( $\text{OCOCH}$ ). FT-IR:  $\nu = 3345$  (s), 3095 (w), 3017 (w), 2934 (w), 1842 (m), 1827 (s), 1748 (vs), 1290 (s), 926 (vs)  $\text{cm}^{-1}$ . HRMS (ESI,  $m/z$ ):  $[\text{M} - \text{H}]^-$  calcd for  $\text{C}_6\text{H}_7\text{NO}_3$ : 140.0348, found: 140.0345.

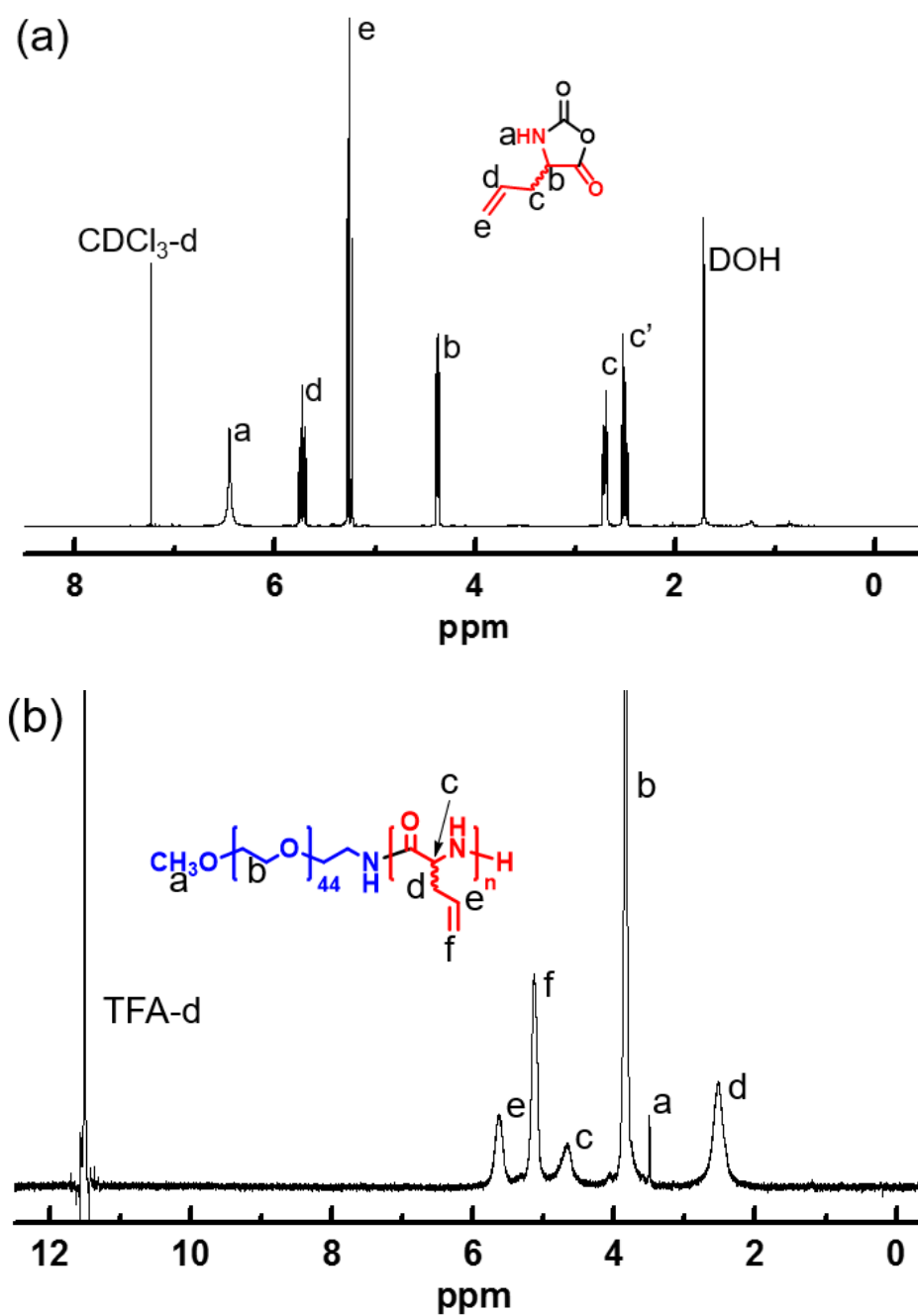


**Figure 4.1.**  $^1\text{H}$  NMR of (a) DLAG-NCA monomer and (b) PEG-b-PDLAG block copolymer.

**Synthesis of PEG-*b*-PDLAG diblock copolymer.** A typical procedure for the preparation of PEG-*b*-PDLAG was as follows: into a flame-dried 250 mL Schlenk flask equipped with a stir bar and capped with a rubber septum with a needle outlet connected to a tube filled with drying agent, DLAG-NCA (2.6160 g, 18.54 mmol) in DMF (150 mL) was injected. After being stirred at room temperature for 5 min, mPEG<sub>45</sub>-NH<sub>2</sub> (1.2317 g, 615.9  $\mu$ mol) in DMF (10 mL) was injected *via* a syringe. The reaction mixture was stirred at room temperature (stir rate = 800 rpm) under continuous nitrogen flow (flow rate = 100 mL min<sup>-1</sup>) for 48 h. The reaction mixture was then precipitated into diethyl ether (1 L) three times. The diblock copolymer was centrifuged, collected, and dried *in vacuo* to yield 2.1480 g (71.2%) as a white powder. <sup>1</sup>H NMR (500 MHz, TFA-d,  $\delta$ ): 2.65 (br, 60 H, CHCH<sub>2</sub>CHCH<sub>2</sub>), 3.63 (s, 3 H, CH<sub>3</sub>O), 3.97 (br, 180 H, OCH<sub>2</sub>CH<sub>2</sub>), 4.78 (br, 30 H, NHCHCO), 5.27 (br, 60 H, CH<sub>2</sub>CHCH<sub>2</sub>), 5.76 (br, 30 H, CH<sub>2</sub>CHCH<sub>2</sub>). <sup>13</sup>C NMR (125 MHz, TFA-d,  $\delta$ ): 38.5 (CHCH<sub>2</sub>CH), 56.1 (NHCH(CO)CH<sub>2</sub>), 59.9 (CH<sub>3</sub>O), 71.9 (CH<sub>2</sub>CH<sub>2</sub>O), 122.2 (CH=CH<sub>2</sub>), 132.6 (CH<sub>2</sub>CH=CH<sub>2</sub>), 175.7 (NHC(CO)CH<sub>2</sub>). FT-IR:  $\nu$  = 3426-3149 (m), 3079 (w), 2871 (m), 1697 (m), 1627 (vs), 1515 (s), 1103 (vs), 701 (m) cm<sup>-1</sup>. DSC:  $T_g$  = -63 °C,  $T_c$  = -40 °C,  $T_m$  = 10 °C,  $T_g$  = 78 °C. TGA: 25-340 °C: 0% mass loss, 340-430 °C: 73.3% mass loss, 430-500 °C: 1.4% mass loss, 25.3% mass remaining above 500 °C.

### 4.3 Results and discussions

The thermo-responsive hydrogelator employed in this study was comprised of the amphiphilic block copolymer poly(ethylene glycol)-*block*-poly(DL-allylglycine) (PEG-*b*-PDLAG). These and similar  $\beta$ -sheet-rich polypeptides have displayed



reversible gelation in response to heat and sonication.<sup>206</sup> Synthesis of a series of three PEG-*b*-PDLAGs was performed through polymerization of the *N*-carboxyanhydride (NCA) of DL-allylglycine *via* a N<sub>2</sub> flow method (Fig. 4.2), to tune the hydrophilic-hydrophobic balance and optimize the gel transition temperature ( $T_{\text{gel}}$ ) to be slightly above room temperature.<sup>57</sup>

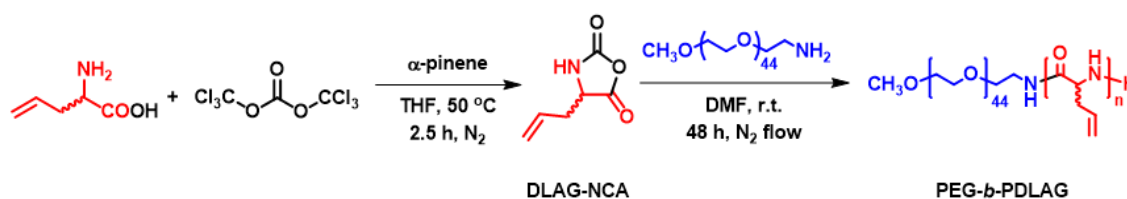


**Figure 4.2.** Synthetic route for PEG-*b*-PDLAG block copolymer.

Reversible and responsive hydrogelations of PEG-*b*-PDLAG were confirmed (Fig. 4.3a). Hydrogels were prepared by direct dissolution of PEG-*b*-PDLAG in water, followed by heating above the sol-to-gel transition temperature ( $T_{\text{gel}}$ ), which was determined by the test tube inversion method. In order to improve the stimuli-responsive sensitivity and achieve rapid response for printing and injection applications, we optimized the  $T_{\text{gel}}$  of the diblock gelator through control of the hydrophilic-hydrophobic balance, which could be tuned by the number of repeating units of the polypeptide block segment. According to Fig. 4.3b, a lower  $T_{\text{gel}}$  transition temperature can be achieved through extension of the PDLAG block, which strengthens the physical

interactions between polymer chains and facilitates the supramolecular assembly process.

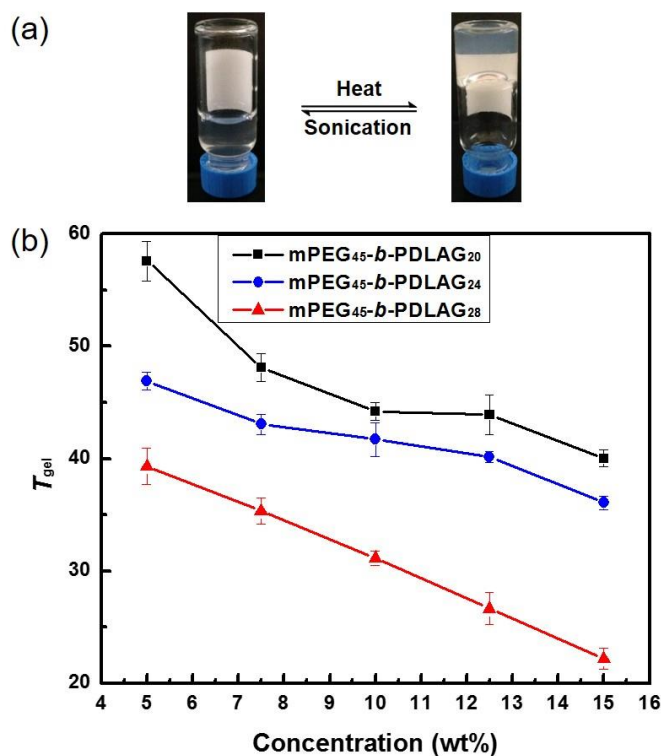


**Figure 4.3.** (a) Stimuli-responsive reversible sol-gel transitions of PEG-*b*-PDLAG block copolymer in water. (b) Change of  $T_{gel}$  as a function of polymer concentration for a series of PEG-*b*-PDLAG, having consistent PEG chain length and variation of the PDLAG chain lengths.

The heat-induced sol-to-gel transitions were attributed to the construction of  $\beta$  sheets and dehydration of PEG, resulting in the formation of  $\beta$ -sheet-rich peptide nanofibrils (Fig. 4.4a); while the sonication-triggered gel-to-sol transitions were assigned to the disruption of long range interactions between these nanofibrils.<sup>79,99</sup> In this way,

the sol-gel transitions were correlated with reversible noncovalent transformation of supramolecularly-assembled nanostructures instead of chemical bond conversion, thus, no additional chemicals, such as a photoacid generator or exchange reagent, were needed.

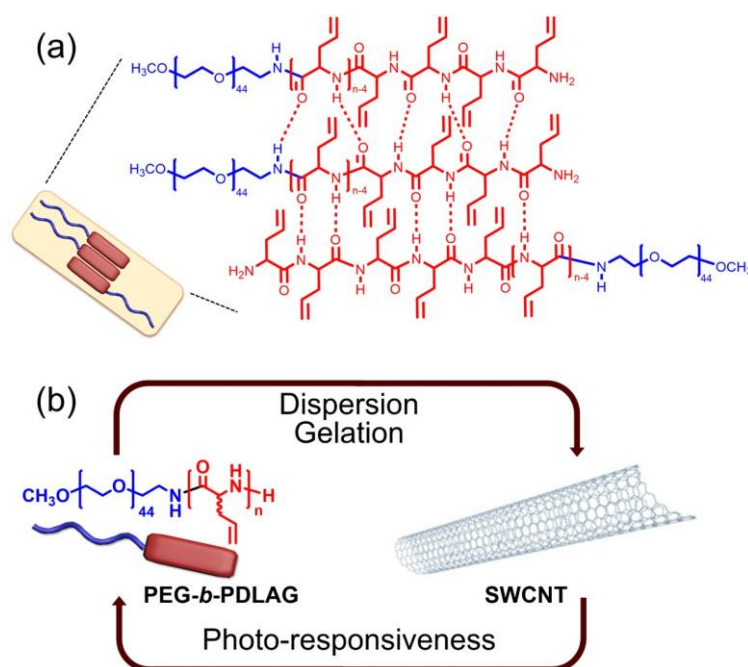


**Figure 4.4.** (a) Illustrative formation of  $\beta$  sheets as constructive units of nanofibrils. (b) Relationships between the functions of the PEG-*b*-PDLAG and SWCNT composite components.

For the conductive component, single-walled carbon nanotubes (SWCNTs) were selected, due to their excellent electrical conductivity, mechanical strength, high aspect ratio, and photo-thermal effect.<sup>207-213</sup> In order to be solution processable, SWCNTs have been dispersed through interaction with a wide variety of conjugated structures.<sup>167,214</sup>

One of the conjugated structures reported was allyl-rich  $\beta$  sheet peptide domain, which has been shown to interact with SWCNT surfaces for dispersion, and display hierarchically ordered assembly behaviors.<sup>100</sup> Therefore, it was anticipated that the  $\pi$ - $\pi$  stacking between the pseudo-aligned allyl groups of PDLAGs and SWCNT surfaces could allow for dispersion of the nanotubes in water, facilitated by the amphiphilic polymers. The working hypothesis for the overall cascading strategy was that there would be a stagewise synergistic effect that would translate the photo-thermal behavior of SWCNTs to a thermo-induced gelation of the polymers, to result in photo-triggered spatially-defined gelation and patterning (Fig. 4.4b).

Preparation of the composite sol dispersion was industry friendly as it merely required 10 min sonication after direct mixing of the two components in nanopure water, as confirmed visually (Fig. 4.5) and by UV/vis spectroscopy (Fig. 4.6).<sup>215</sup> Herein, PEG-*b*-PDLAG served as both a dispersant and a stimuli-responsive component. Dispersion was further characterized microscopically by comparing the difference in transmission electron microscopic (TEM) images between freshly sonicated SWCNT and PEG-*b*-PDLAG/SWCNT composite sol (Fig. 4.7a and 4.7b), as the composite exhibited better dispersion and less aggregation into bundles.

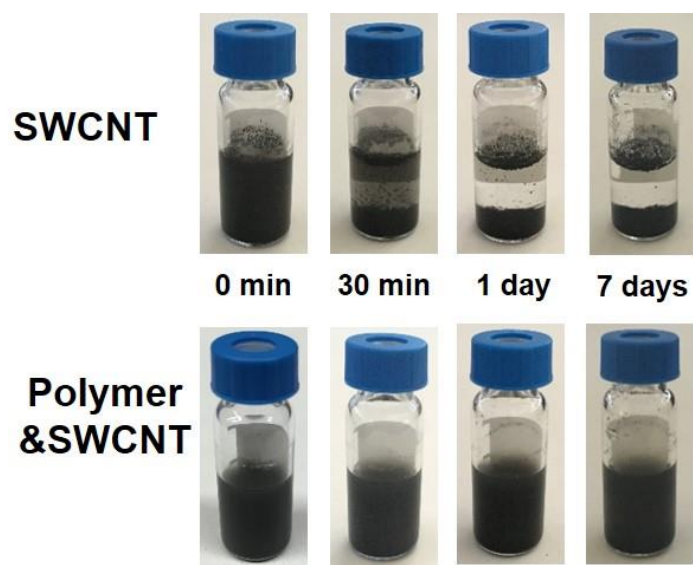


**Figure 4.5.** Images of SWCNTs in H<sub>2</sub>O without (upper images) and with polymer (lower images), correlated with various time points after sonication (1 mg/mL SWCNTs, 0 or 10 mg/mL polymer).

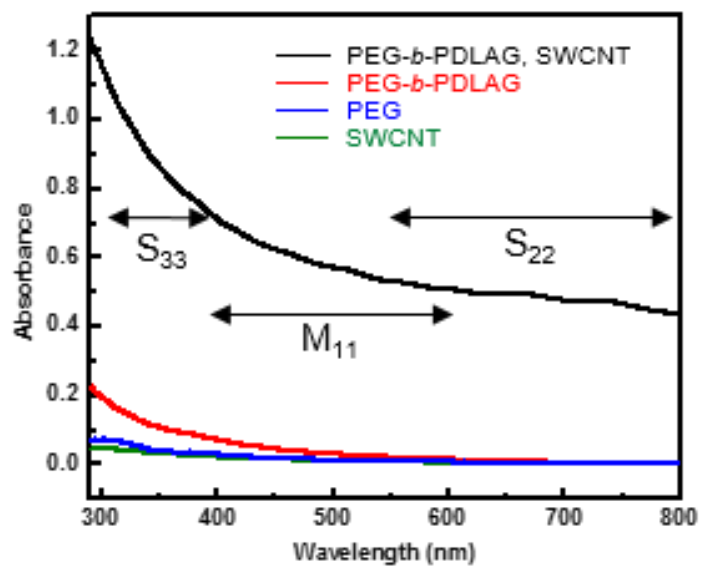


**Figure 4.6.** UV/vis spectra of assorted systems (with 0.05 mg/mL SWCNTs, 1 mg/mL polymer, if applicable).

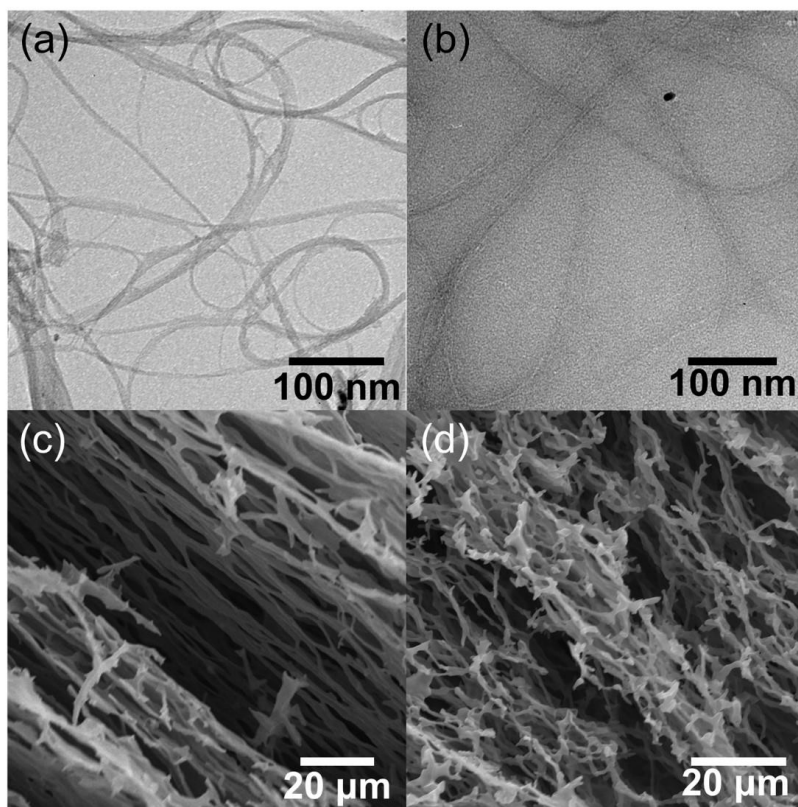


**Figure 4.7.** TEM images of (a) SWCNT sol and (b) PEG-*b*-PDLA/SWCNT composite sol, without staining. SEM images of aerogels of (c) 5 wt% PEG-*b*-PDLA and (d) 5 wt% PEG-*b*-PDLA/0.5 wt% SWCNT composite.

The UV/vis absorbance spectra illustrate comparatively high absorbance through the entire measured range for the PEG-*b*-PDLA/SWCNT composite, while SWCNT in water barely displayed any absorbance due to precipitation.

$S_{33}$  refers to third order Van Hove singularities of semiconducting SWCNTs,  $M_{11}$  refers to first order Van Hove singularities of metallic SWCNTs, and  $S_{33}$  refers to second order Van Hove singularities of semiconducting SWCNTs.<sup>216,217</sup>

PEG-*b*-PDLAG/SWCNT hydrogels were prepared by heating sols to their  $T_{gel}$  values, which decreased upon the addition of SWCNTs (Fig. 4.8). Scanning electron microscopic (SEM) images showed fibrillar network structures, but with different fibrillar curvature, for matrices of PEG-*b*-PDLAG with and without SWCNTs, indicating SWCNTs affected or participated in the formation of composite gel matrix (Fig. 4.7c and 4.7d).

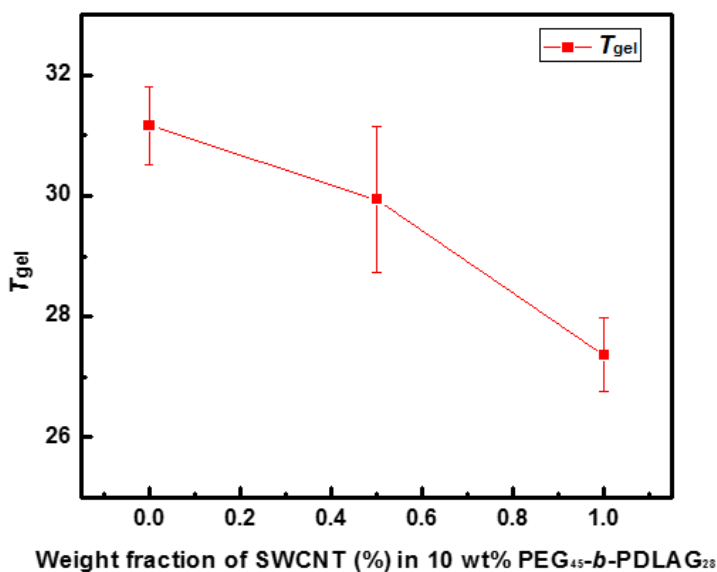


**Figure 4.8.** Incorporation of SWCNTs increased the thermal responsive sensitivity of the composite gel materials.

As expected, composite gels at 1 wt% SWCNT expressed higher stiffness in dynamic mechanical analysis (DMA), compared with polymer gels (Fig. 4.9), which can

be attributed to the high mechanical strength and a certain extent of entanglement of SWCNTs in the composite. However, the depressed stiffness with even higher (2 wt%) SWCNT incorporation might be a result of the over-consumption of the gelators in dispersing the nanotube fillers, resulting in a difficulty to form an interconnected network.

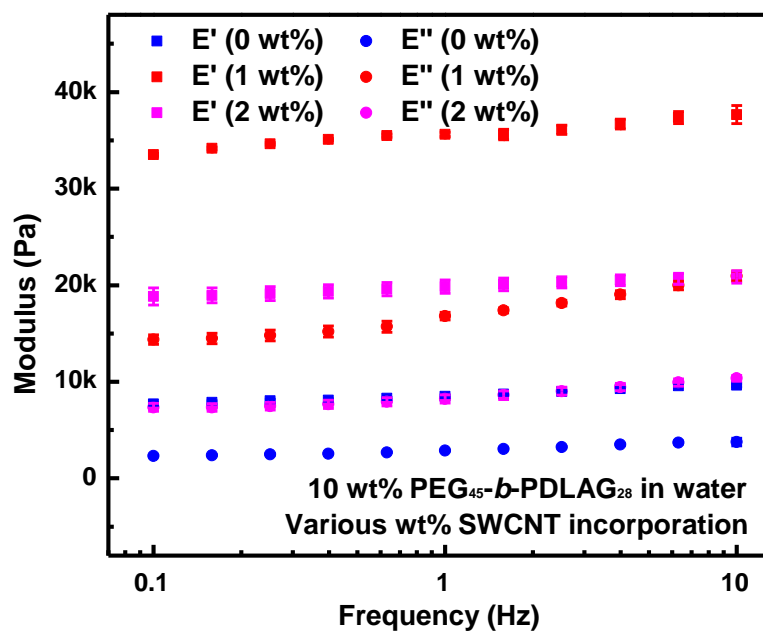


**Figure 4.9.** Moduli of PEG-*b*-PDLA/SWCNT hydrogels as a function of frequency conducted by DMA ( $E'$  and  $E''$  indicate storage and loss modulus, respectively).

In order to understand the potential driving force for gelation, IR spectroscopy was utilized to examine the supramolecular structure within freeze-dried samples. The



IR spectra of polymer and polymer/SWCNT composite were almost identical, with the presence of signatures of  $\beta$ -sheet secondary structures, demonstrating that formation of  $\beta$ -sheet structures remained as a potential driving force for the gelation of the composite (Fig. 4.10).<sup>68</sup>

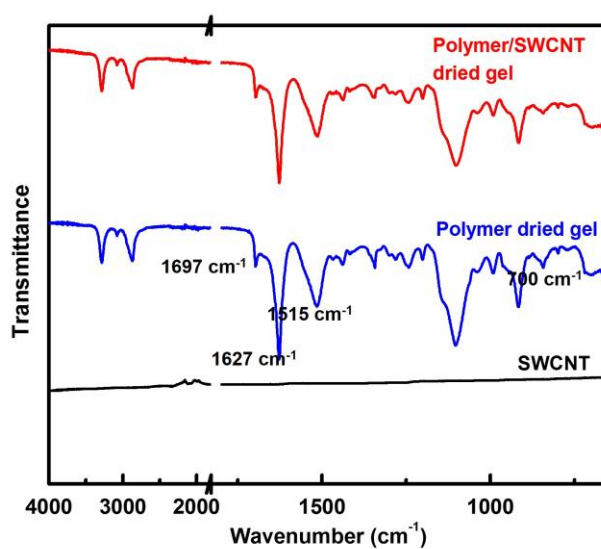


**Figure 4.10.** IR spectra of polymer/SWCNT aerogel, polymer aerogel, and SWCNTs.

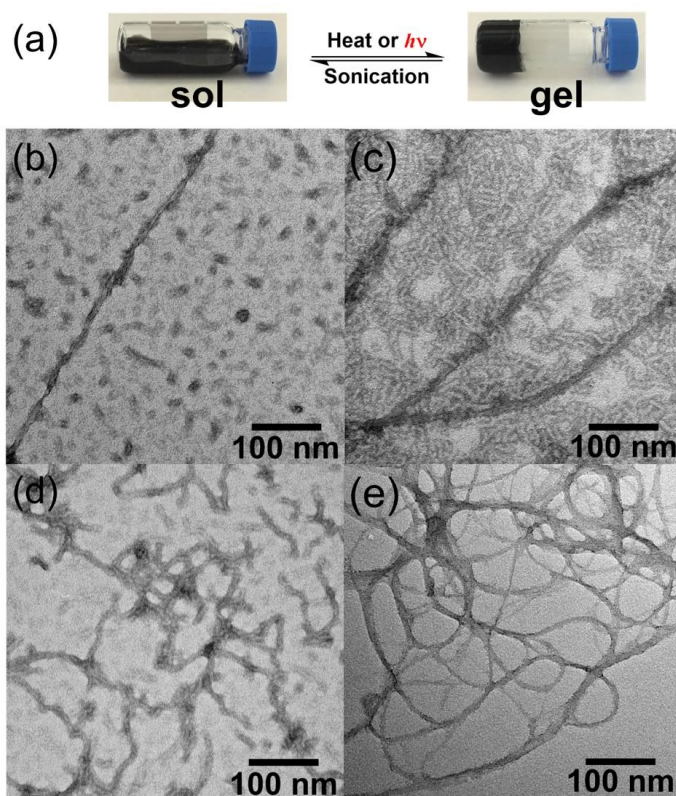


**Figure 4.11.** (a) Reversible stimuli-responsive sol-gel transitions of the composite material having 5 wt% PEG-*b*-PDLA and 0.5 wt% SWCNT. TEM images of (b) PEG-*b*-PDLA/SWCNT composite sol, (c) PEG-*b*-PDLA/SWCNT composite gel, (d) PEG-*b*-PDLA gel, and (e) SWCNT sol, with phosphotungstic acid stain. For each TEM image, the sample concentrations were at 1 mg/mL PEG-*b*-PDLA and 0.1 mg/mL SWCNT, if applicable.

Based on the dispersion and gelation studies, the stimuli-responsive behaviors were then explored to verify the feasibility of our material design. In addition to thermo- and sonication-responsive behaviors, it is worth noting that irradiation of the composite sol with light (532 nm or 785 nm, 250 mW, 2 mm diameter laser beam) induced sol-to-gel transitions (Fig. 4.11a), agreeing with our hypothesis on the synergistic photo-to-thermal cascading effects. Moreover, either the sols or gels were highly sensitive

towards light, heat or mechanical stimulus, as controllable sol-gel transitions typically took place within 10 seconds. The differences of nanostructural morphologies were then visualized by TEM to further study the dispersion and phase transition mechanisms. In TEM images, polymers adopted shapes as spherical aggregates and short nanofibrils in sol (Fig. 4.11b), and converted reversibly to longer nanofibrils with inter-fibrillar interactions and entanglements in the gel state (Fig. 4.11c). These transformations of polymeric nanostructures accounted for the sol-gel transitions on a macroscale (Fig. 4.12). On the other hand, SWCNTs in both sol and gel states (Fig. 4.11b and 4.11c) remained as longer fibers with less curvature, compared with polymer nanofibrils in the absence of SWCNT (Fig. 4.11d). Furthermore, the stained composite nanotubes displayed larger diameters (Fig. 4.11b:  $15.3 \pm 4.0$  nm, and Fig. 4.11c:  $18.9 \pm 3.6$  nm), compared with unstained composite nanotubes (Fig. 4.7b,  $2.4 \pm 0.4$  nm). Due to staining of the polymers in the sample, the width increase can then be attributed to the noncovalent attachment of polymers on nanotube surfaces, and, thus, resulting in nanotube dispersion (*vide supra*).

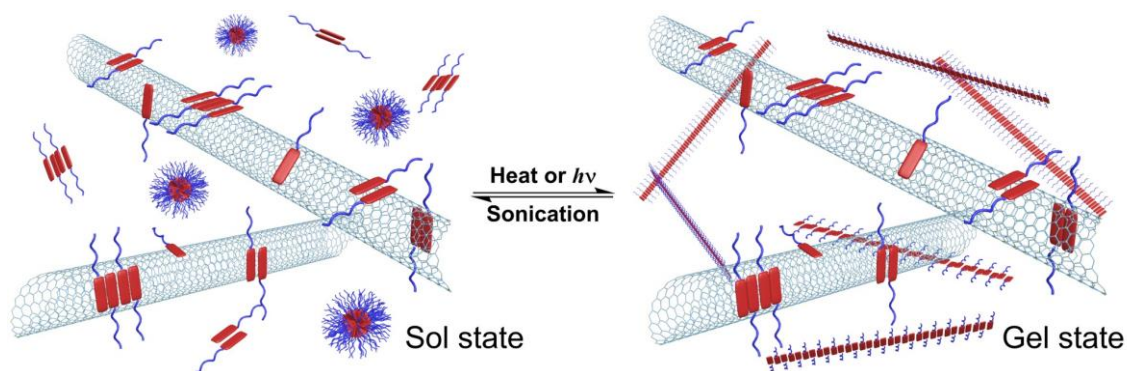


**Figure 4.12.** Schematic illustration of a PEG-*b*-PDLA/SWCNT dispersion, and reversible conversion of polymeric supramolecular structures that correlates to the formation or break-down of gel matrix in response to a stimulus.

The potential application of this smart composite system as patternable and rewritable conductive materials was then investigated, taking advantage of the rapid and reversible phase transition through supramolecular assembly. As an example for the patterning process, the composite sol was applied to a glass substrate, then followed by direct irradiation with a laser beam. The irradiated region underwent a photo-curing process, giving a sol-to-gel transition and producing a spatially-defined gel pattern that remained on the surface after removal of the sol (Fig. 4.13). The gel could be reverted to sol by sonication, or could be air dried to produce a composite film, which can be recycled as well for another writing process. Electrical conductivities of dried composite films were determined by four point probe measurements. For a composite film with 25 wt% SWCNT (derived from a pre-gelled film of a 7.5 wt% PEG<sub>45</sub>-*b*-PDLA<sub>28</sub>/2.5 wt% SWCNT sample, followed by allowing the film to dry under ambient conditions and heat-pressing), the electrical conductivity was determined to be ca. 130 S·m<sup>-1</sup> (Fig. 4.14),

which is comparable to the highest reported values of hybrid films derived from conductive hydrogels that typically contain conductive polymers.<sup>218</sup>

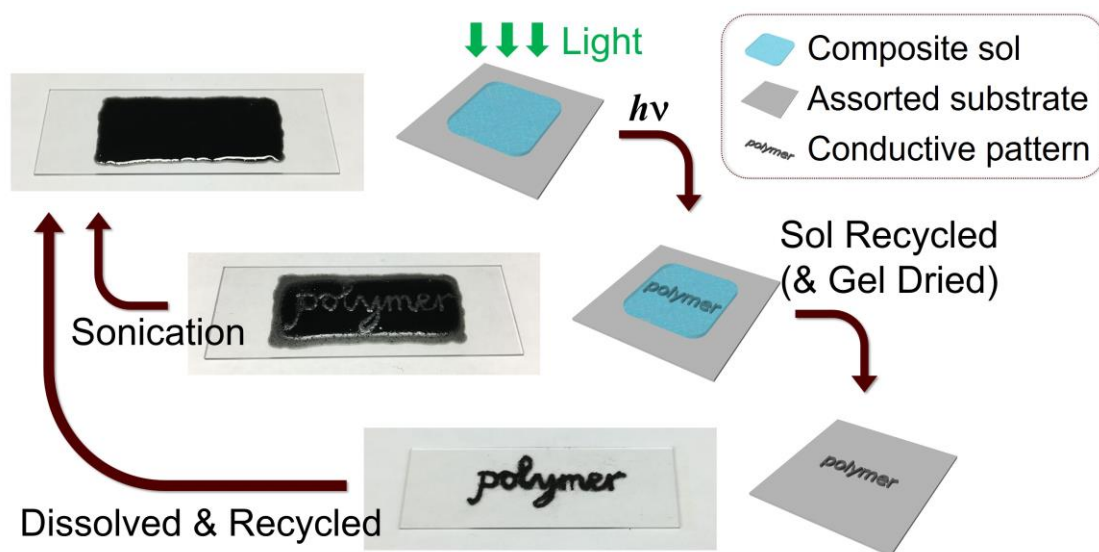


**Figure 4.13.** Schematic illustration of the reversible photo-patterning process for production of soft electronics.

To further examine the reversibility and recyclability, electrical conductivities of composite films of up to three reprocessing cycles were obtained and found to remain similar after repeated recycling (Fig. 4.16).

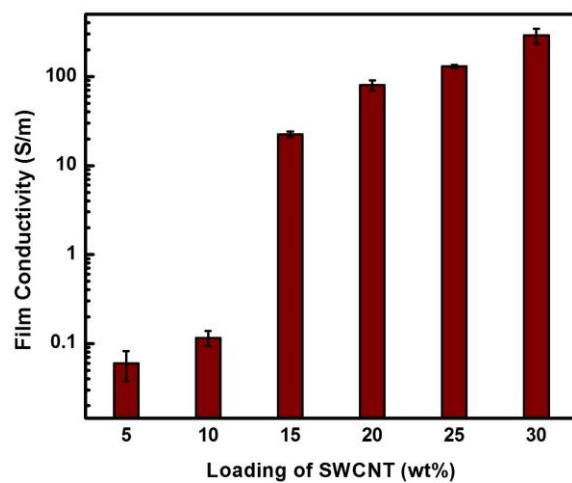


**Figure 4.14.** Electrical conductivity of composite films (PEG<sub>45</sub>-*b*-PDLA G<sub>28</sub>/SWCNT) as a function of percentage SWCNT incorporation.

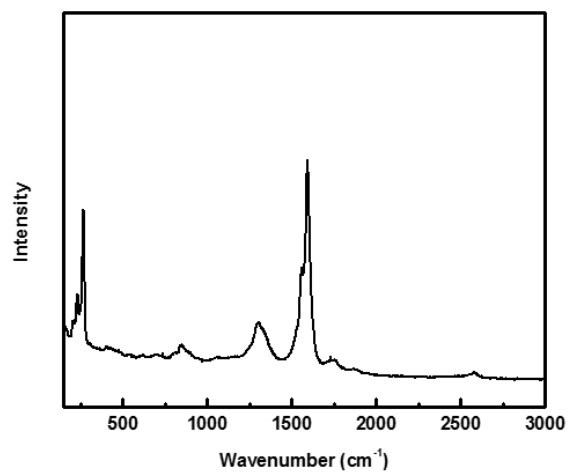


**Figure 4.15.** Raman spectrum of SWCNTs in solid form.

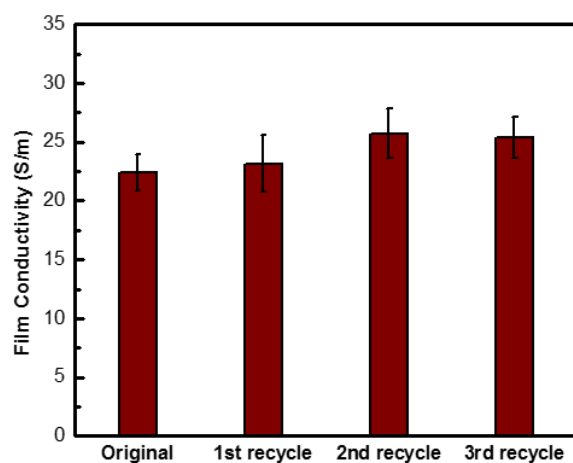


**Figure 4.16.** Conductivities of films composed of 15 wt% of SWCNTs and 85 wt% of PEG<sub>45</sub>-*b*-PDLA<sub>28</sub>. One recycle process involves resuspension of the composite into water with sonication, responsive sol-to-gel transition, and film formation through air dry.

Moreover, a printed free standing thin film was fabricated into a Möbius strip (Fig. 4.17), suggesting that these thin films are flexible towards bending and twisting for soft electronics.

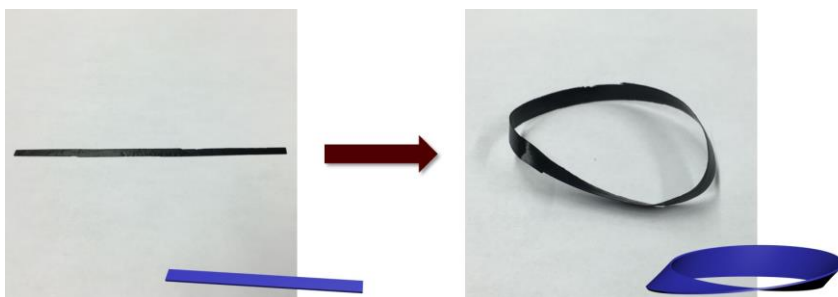


**Figure 4.17.** A printed free standing thin film fabricated into a Möbius strip.

The average electrical conductivity values were obtained by measuring four different locations on the same film sample. After each measurement, the film was turned 45 degrees for the next measurement. Based on multiple measurements, linear fitted I-V curves of films are now attached as Fig. 4.18. Accordingly, the sheet resistance values, film thickness and calculated electrical conductivities were summarized in Table 4.1.

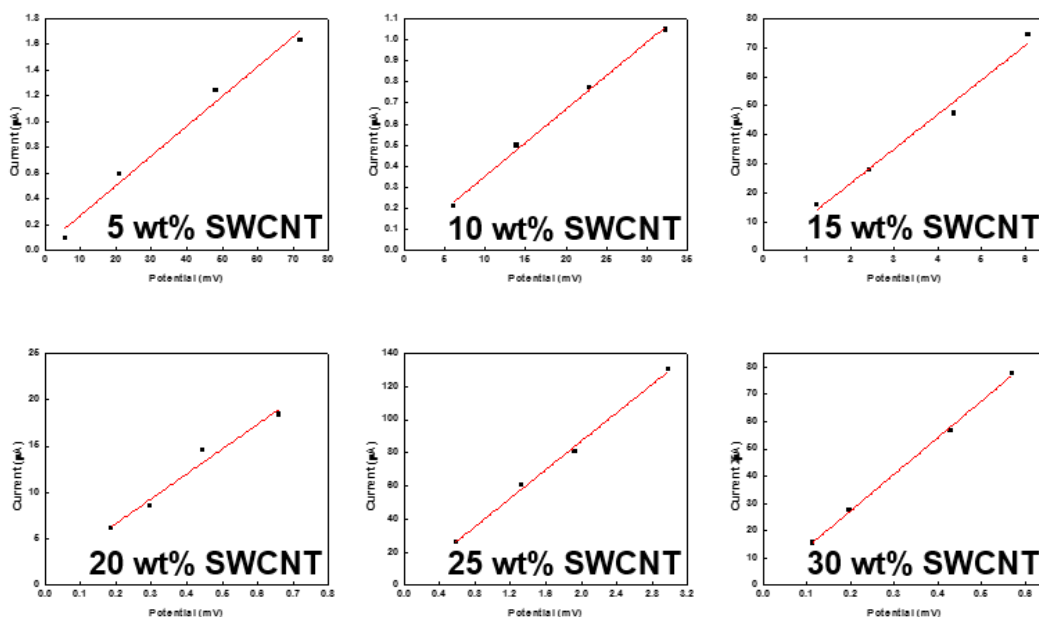


**Figure 4.18.** Linear fitted I-V curves of composite films with various percentage of SWCNT incorporation. Each spot was generated by measuring conductivity at a different location.



**Table 4.1.** Sheet resistance, thickness, and electrical conductivity of composite films as a function of percentage of SWCNT incorporation.

Loading of SWCNT (wt%)	Sheet resistance $R_s$ ( $\Omega/\text{sq}$ )	Film thickness $t$ ( $\mu\text{m}$ )	Electrical conductivity $\sigma$ (S/m)
5	$(2.1 \pm 0.8) \times 10^5$	$79 \pm 1$	$(6.0 \pm 2.2) \times 10^{-2}$
10	$(1.1 \pm 0.2) \times 10^5$	$77 \pm 6$	$(1.2 \pm 0.2) \times 10^{-1}$
15	$(4.0 \pm 0.3) \times 10^2$	$112 \pm 1$	$(2.2 \pm 0.2) \times 10^1$
20	$(1.2 \pm 0.2) \times 10^2$	$102 \pm 1$	$(8.0 \pm 1.0) \times 10^1$
25	$(9.0 \pm 0.4) \times 10^1$	$85 \pm 1$	$(1.3 \pm 0.1) \times 10^2$
30	$(2.9 \pm 0.1) \times 10^1$	$119 \pm 22$	$(2.9 \pm 0.6) \times 10^2$

#### 4.4 Conclusions

In summary, we developed a hydrogel-based block copolymeric/inorganic composite system that exhibited a wide range of thermo-, mechano- and photo-responsive properties. These materials are highly processable with assorted stimuli inputs, including temperature increase or photo irradiation for gelation and patterning, and sonication for material recycling. Furthermore, this system provided a novel method to process conductive materials in a liquid phase, followed by facile and rapid curing into desired patterns with the potential to take advantage of the modern photo stereolithographic technologies, without the requirement of a pre-treated substrate or a specific irradiation wavelength. The application of this composite system into 3D conductive networks for energy storage devices and neural signal harvesting are subjects of our current investigations.

## CHAPTER V

### CONCLUSIONS

Gels with stimuli-triggered sol-gel transitions have been extensively studied for applications in controlled drug release, tissue engineering, selective sensing, and photolithography fields, owing to their capability to respond to stimuli rapidly, the versatility to assemble into specific nano- and/or microstructures in various environments, and the ability to exhibit changes in macroscopic characteristics. The drastic difference of the physical properties between sol and gel states, and the rapid switch of sol-gel transitions have rendered smart gels as potential materials for applications that require both sol and gel type behaviors during different stages of operation. The stimuli-triggered sol-gel transition process enables the localization and breakdown of the soft gelation materials with spatial and temporal precision, which is of great significance for controlled material fabrication, implantation and degradation.

Among the smart stimuli-responsive gelators, synthetic polypeptides are of great interest toward biomedical applications due to their innate biocompatibility, biodegradability, facile synthesis through NCA ROP, versatile side chain functionalities, and capability to adopt unique ordered conformations in response to stimuli, with correlations between the conformational switch of secondary structures and the sol-gel phase transition. For example, through the stimuli-triggered construction/destruction of  $\alpha$ -helix or  $\beta$ -sheet, supramolecular assembly of polypeptides can be controlled, resulting in formation/break down of gel matrix.

The investigation of polypeptide-based amphiphilic gelators originated from our serendipitous discovery of gelation during polymerization of DL-allylglycine, initiated with  $\alpha$ -amino-PEG in DMF. Research into the gelation mechanism laid the first solid foundation of the work discussed in this dissertation. Another solid foundation was laid as a result of an “unfortunate” situation: the temporarily inoperable status of glovebox. During waiting for the repair of glovebox, a new synthetic method for the syntheses of polypeptide materials was developed, in which N<sub>2</sub> flow was firstly utilized to keep the moisture out of the reaction setup to maintain the dry condition of NCA polymerization. Surprisingly, accelerated polymerization rates were observed, which further led into the exploration and development of the straightforward and readily-adoptable N<sub>2</sub> flow method for the preparation of polypeptides with well-defined structures. This N<sub>2</sub> flow method enables rapid and facile synthesis of polypeptides with different molecular weight, derived from a variety of amino acids, making it easier to control the properties of targeted polypeptides.

Based on the above two solid foundations laid by Dr. Jiong Zou and Dr. Jingwei Fan, we targeted on expanding the gelation property of polypeptides from organic solvents to water, which could have a broader application. In this regard, A multi-responsive triblock hydrogelator ODLAG-*b*-PEG-*b*-ODLAG was synthesized facilely by ROP of DLAG NCA with a diamino-terminated PEG as the macroinitiator, as described in Chapter II. The ability to form hydrogels is shown to be dependent on the hydrophobic and hydrophilic balance and is dictated by the block length of the oligopeptide blocks, which is in turn easily controlled by reaction feed ratio. This

system exhibited heat-induced sol-to-gel transitions and either sonication- or enzyme-induced gel-to-sol transitions. The  $\beta$ -sheeting of the oligopeptide segments was confirmed by ATR-FTIR and WAXS. Detailed characterization studies indicated that hydrogelation may be driven by a combination of oligopeptide  $\beta$ -sheeting and a balance between PEG-PEG interactions and PEG-water interactions, with effects observed at the supramolecular, nano-, micro- and macro-scales. Moreover, the oligopeptide segments carry reactive allyl side chain groups, which have the potential to be further functionalized into intelligently-designed systems of increased complexity and functionality. The  $\beta$ -sheets further displayed tertiary ordering into fibrillar structures that, in turn generated a porous and interconnected hydrogel matrix, as observed *via* TEM and SEM. The reversible macroscopic sol-to-gel transitions triggered by heat and gel-to-sol transitions triggered by sonication were correlated with the transformation of nanostructural morphologies, with fibrillar structures observed in gel and spherical aggregates in sol, respectively. The enzymatic breakdown of the hydrogels was also investigated. This allyl-functionalized hydrogelator can serve as a platform for the design of smart hydrogels, appropriate for expansion into biological systems as bio-functional and bio-responsive materials.

The above triblock hydrogelator ODLAG-*b*-PEG-*b*-ODLAG was capable of dispersing and gelating SWCNTs, as discussed in Chapter III. This triblock tethered oligopeptide, which formed  $\beta$ -sheet secondary structures, displayed the ability to homogeneously disperse SWCNTs in DMF solution. In addition to binding with SWCNTs, the ODLAG peptide  $\beta$ -sheets also regulated the assembly of the peptide-

coated nanotubes into hierarchically-ordered structures *via* peptide-peptide interactions between adjacent oligopeptide wrapped SWCNTs. Detailed characterization studies indicated that the supramolecular self-assembly of  $\beta$ -sheets in the oligopeptide blocks form one dimensional stacked nanoribbons, in which allyl-rich ODLAG peptide domains have strong propensity for  $\pi$ - $\pi$  stacking with SWCNT surfaces, and consequently, efficiently separated and dispersed SWCNTs in organic solvent. The ODLAG peptide  $\beta$ -sheets could both noncovalently associate with the SWCNTs and assemble peptide-coated nanotubes into hierarchically-ordered structures *via* peptide-peptide interactions. On increase in polymer concentration, the triblock-SWCNT composites formed fibrillar networks that resulted in organogels. Compared with the ODLAG-*b*-PEG-*b*-ODLAG organogel without SWCNTs, the SWCNT organogel composite expressed a *ca.* 400 fold increase in stiffness (storage modulus = 400 kPa), as characterized by dynamic mechanical analysis. Despite these structures manifesting on the nanoscale, micro/mesoscale homogeneity was increased in the composite gels when compared to the triblock gel alone. With the incorporation of SWCNTs the mechanical properties of triblock-based organogels increased greatly, further displaying a dispersed (not merely encapsulated) state in the gel matrix. This work provides an interesting strategy that uses secondary structure control to stabilize SWCNTs, allowing for the efficient noncovalent incorporation of SWCNTs in the polymeric matrix without disrupting the band-structure of the SWCNTs. Moreover, sonication-responsive properties, enhanced mechanical properties and the presence of known biodegradable moieties enable further

study and potential applications in sensor design, construction of adaptive materials and controlled release systems.

Based upon the above the studies in Chapter II and III, in Chapter IV, a hydrogel-based block copolymeric/inorganic composite system that exhibited a wide range of thermo-, mechano- and photo-responsive properties was developed. These materials are highly processable with assorted stimuli inputs, including temperature increase or photo irradiation for gelation and patterning, and sonication for material recycling. This is a composition of matter and method of preparation for biologically-derived and compatible peptide-carbon nanotube hybrid systems that exhibit unique rapid and stimulus-responsive fluid-to-gel reversible behavior, conductive properties and reversible patterning capabilities. In terms of biologically-related applications, the sol-to-gel transition can be realized by near infrared light irradiation, which makes it possible for patterning after injection. However, many previously reported photo-induced sol-to-gel transition materials required irradiation with UV light. The sol-to-gel transition is realized by supramolecular assembly while other reports rely on photo-polymerization. In terms of application as patternable flexible conductive materials, the carbon nanotubes become photo-patternable through a facile bottom-up process on various substrates, while the previous reports on carbon nanotube patterning that use the bottom-up techniques require special treatment on the substrates or carbon nanotubes. And top-down approaches may require expensive equipment and time-consuming processes. Compared with organic materials, organic materials such as PEDOT:PSS usually have poor stability that may limit their application in electronic devices, while

SWCNTs are regarded as a comparatively stable materials. In terms of reversibly-patternable materials, the photo-patterning is realized through supramolecular assembly and sol-gel transition, and the pattern can be written, erased and recycled in a reversible process. In comparison, for most of the previously reported photo-patterning systems, pattern writing or erasing is usually irreversible because the procedure relies on the formation or cleavage of certain chemical bonds, which is typically irreversible. Photo-induced supramolecular assembly systems may have an advantage over photopolymerization systems in that assembly systems do not require the generation of radicals, which may cause damage or death to cells. Furthermore, this system provided a novel method to process conductive materials in a liquid phase, followed by facile and rapid curing into desired patterns with the potential to take advantage of the modern photolithographic technologies, without the requirement of a pre-treated substrate or a specific irradiation wavelength.

In summary, polypeptide gelators possess great potential to be used for biomedical and patterning applications resulting from their structural characteristics and synthetic feasibility. In this dissertation, the fundamental investigations of gelation mechanisms and behaviors of polypeptide-based gelators, including their design, and relationship between nanoscopic and macroscopic morphologies were performed. Following these projects in this dissertation, several future investigations are underway. For example, the development of *helix-block-sheet* hydrogelators for the potentially more defined fibrillar structures, better physical properties and new responsive behaviors is being realized through the construction of poly( $\gamma$ -Propargyl-L-glutamate)-*block*-

poly(DL-allylglycine) (PPLG-*b*-PDLAG). Thiol-yne click reactions were carried out to incorporate charges onto the PPLG block, increasing the solubility of the block copolymers. Another future direction is the advancement of synthetic techniques that allow for the preparation of polypeptides with sequence control. Previous efforts showed that the synthesis of dipeptide NCA was not successful, while tetrapeptide NCA would be more promising according to theoretical calculation. The synthesis of tetrapeptide through solid-phase peptide synthesis was proposed, and the ring-closure to form tetrapeptide NCAs will be investigated. Clearly, there is more progress to be achieved in both fundamental studies and application/commercialization of the patterning technologies, with this work contributing to the current advancement of smart polypeptide-derived gelators towards potential biomedical and patterning applications.



## REFERENCES

- (1) Ahn, S.-K.; Kasi, R. M.; Kim, S.-C.; Sharma, N.; Zhou, Y. *Soft Matter* **2008**, *4*, 1151-1157.
- (2) Zou, J.; Zhang, F.; Zhang, S.; Pollack, S. F.; Elsabahy, M.; Fan, J.; Wooley, K. L. *Adv. Healthc. Mater.* **2014**, *3*, 441-448.
- (3) Zhang, H.; Zhao, T.; Newland, B.; Duffy, P.; Annaidh, A. N.; O'Cearbhaill, E. D.; Wang, W. *J. Mater. Chem. B* **2015**, *3*, 6420-6428.
- (4) He, C.; Kim, S. W.; Lee, D. S. *J. Control. Release* **2008**, *127*, 189-207.
- (5) Tsitsilianis, C. *Soft Matter* **2010**, *6*, 2372-2388.
- (6) Yu, L.; Ding, J. *Chem. Soc. Rev.* **2008**, *37*, 1473-1481.
- (7) Park, M. H.; Joo, M. K.; Choi, B. G.; Jeong, B. *Acc. Chem. Res.* **2011**, *45*, 424-433.
- (8) Ding, C.; Zhao, L.; Liu, F.; Cheng, J.; Gu, J.; Dan, S.; Liu, C.; Qu, X.; Yang, Z. *Biomacromolecules* **2010**, *11*, 1043-1051.
- (9) Zhang, F.; Zhang, S.; Pollack, S. F.; Li, R.; Gonzalez, A. M.; Fan, J.; Zou, J.; Leininger, S. E.; Pavia-Sanders, A.; Johnson, R.; Nelson, L. D.; Raymond, J. E.; Elsabahy, M.; Hughes, D. M. P.; Lenox, M. W.; Gustafson, T. P.; Wooley, K. L. *J. Am. Chem. Soc.* **2015**, *137*, 2056-2066.
- (10) Shen, Y.; Zhang, S.; Zhang, F.; Loftis, A.; Pavia-Sanders, A.; Zou, J.; Fan, J.; Taylor, J. S. A.; Wooley, K. L. *Adv. Mater.* **2013**, *25*, 5609-5614.
- (11) Hunt, J. A.; Chen, R.; van Veen, T.; Bryan, N. *J. Mater. Chem. B* **2014**, *2*, 5319-5338.

- (12) Li, Y.; Rodrigues, J.; Tomas, H. *Chem. Soc. Rev.* **2012**, *41*, 2193-2221.
- (13) Shibata, H.; Heo, Y. J.; Okitsu, T.; Matsunaga, Y.; Kawanishi, T.; Takeuchi, S. *Proc. Natl. Acad. Sci. U.S.A.* **2010**, *107*, 17894-17898.
- (14) Ikeda, M.; Tanida, T.; Yoshii, T.; Kurotani, K.; Onogi, S.; Urayama, K.; Hamachi, I. *Nat. Chem.* **2014**, *6*, 511-518.
- (15) Maity, C.; Hendriksen, W. E.; van Esch, J. H.; Eelkema, R. *Angew. Chem. Int. Ed.* **2015**, *54*, 998-1001.
- (16) Huynh, C. T.; Nguyen, M. K.; Lee, D. S. *Macromolecules* **2011**, *44*, 6629-6636.
- (17) Deng, C.; Wu, J.; Cheng, R.; Meng, F.; Klok, H.-A.; Zhong, Z. *Prog. Polym. Sci.* **2014**, *39*, 330-364.
- (18) Kricheldorf, H. R. *Angew. Chem. Int. Ed.* **2006**, *45*, 5752-5784.
- (19) Huang, J.; Heise, A. *Chem. Soc. Rev.* **2013**, *42*, 7373-7390.
- (20) Shen, Y.; Fu, X.; Fu, W.; Li, Z. *Chem. Soc. Rev.* **2015**, *44*, 612-622.
- (21) Krannig, K.-S.; Sun, J.; Schlaad, H. *Biomacromolecules* **2014**, *15*, 978-984.
- (22) Dong, H.; Shu, J. Y.; Dube, N.; Ma, Y.; Tirrell, M. V.; Downing, K. H.; Xu, T. *J. Am. Chem. Soc.* **2012**, *134*, 11807-11814.
- (23) Deming, T. J. *Chem. Rev.* **2016**, *116*, 786-808.
- (24) Fan, J.; Li, R.; He, X.; Seetho, K.; Zhang, F.; Zou, J.; Wooley, K. L. *Polym Chem.* **2014**, *5*, 3977-3981.
- (25) Engler, A. C.; Lee, H. I.; Hammond, P. T. *Angew. Chem. Int. Ed.* **2009**, *48*, 9334-9338.
- (26) Quadir, M. A.; Martin, M.; Hammond, P. T. *Chem. Mater.* **2014**, *26*, 461-476.

- (27) Wang, Y.; Fan, J.; Darensbourg, D. J. *Angew. Chem.* **2015**, *127*, 10344-10348.
- (28) Habraken, G. J. M.; Heise, A.; Thornton, P. D. *Macromol. Rapid Comm.* **2012**, *33*, 272-286.
- (29) Cheng, J.; Deming, T. J. *Top. Curr. Chem.* **2012**, *310*, 1-26.
- (30) Hehir, S.; Cameron, N. R. *Polym. Int.* **2014**, *63*, 943-954.
- (31) Lu, H.; Wang, J.; Song, Z.; Yin, L.; Zhang, Y.; Tang, H.; Tu, C.; Lin, Y.; Cheng, J. *Chem. Commun.* **2014**, *50*, 139-155.
- (32) Leuchs, H. *Ber. Dtsch. Chem. Ges.* **1906**, *39*, 857-861.
- (33) Leuchs, H.; Manasse, W. *Ber. Dtsch. Chem. Ges.* **1907**, *40*, 3235-3249.
- (34) Leuchs, H.; Geiger, W. *Ber. Dtsch. Chem. Ges.* **1908**, *41*, 1721-1726.
- (35) Hadjichristidis, N.; Iatrou, H.; Pitsikalis, M.; Sakellariou, G. *Chem. Rev.* **2009**, *109*, 5528-5578.
- (36) Huesmann, D.; Birke, A.; Klinker, K.; Türk, S.; Räder, H. J.; Barz, M. *Macromolecules* **2014**, *47*, 928-936.
- (37) Wong, S.; Kwon, Y. J. *J. Polym. Sci. A Polym. Chem.* **2015**, *53*, 280-286.
- (38) Zhao, W.; Gnanou, Y.; Hadjichristidis, N. *Polym. Chem.* **2015**, *6*, 6193-6201.
- (39) Wei, Z.; Zhu, S.; Zhao, H. *Polym. Chem.* **2015**, *6*, 1316-1324.
- (40) Ulkoski, D.; Meister, A.; Busse, K.; Kressler, J.; Scholz, C. *Colloid Polym. Sci.* **2015**, *293*, 2147-2155.
- (41) Wibowo, S. H.; Sulistio, A.; Wong, E. H. H.; Blencowe, A.; Qiao, G. G. *Adv. Funct. Mater.* **2015**, *25*, 3147-3156.

- (42) Lu, Y.; Ngo Ndjock Mbong, G.; Liu, P.; Chan, C.; Cai, Z.; Weinrich, D.; Boyle, A. J.; Reilly, R. M.; Winnik, M. A. *Biomacromolecules* **2014**, *15*, 2027-2037.
- (43) Tang, H.; Ling, Y.; Deng, Y.; Zhang, D. *J. Polym. Sci. A Polym. Chem.* **2014**, *52*, 1905-1915.
- (44) Aliferis, T.; Iatrou, H.; Hadjichristidis, N. *Biomacromolecules* **2004**, *5*, 1653-1656.
- (45) Pickel, D. L.; Politakos, N.; Avgeropoulos, A.; Messman, J. M. *Macromolecules* **2009**, *42*, 7781-7788.
- (46) Vayaboury, W.; Giani, O.; Cottet, H.; Deratani, A.; Schue, F. *Macromol. Rapid Comm.* **2004**, *25*, 1221-1224.
- (47) Habraken, G. J. M.; Wilsens, K. H. R. M.; Koning, C. E.; Heise, A. *Polym Chem.* **2011**, *2*, 1322-1330.
- (48) Deming, T. J. *Nature* **1997**, *390*, 386-389.
- (49) Nowak, A. P.; Breedveld, V.; Pakstis, L.; Ozbas, B.; Pine, D. J.; Pochan, D.; Deming, T. J. *Nature* **2002**, *417*, 424-428.
- (50) Dimitrov, I.; Schlaad, H. *Chem. Commun.* **2003**, 2944-2945.
- (51) Conejos-Sanchez, I.; Duro-Castano, A.; Birke, A.; Barz, M.; Vicent, M. J. *Polym Chem.* **2013**, *4*, 3182-3186.
- (52) Lu, H.; Cheng, J. *J. Am. Chem. Soc.* **2007**, *129*, 14114-14115.
- (53) Lu, H.; Cheng, J. *J. Am. Chem. Soc.* **2008**, *130*, 12562-12563.

- (54) Stukenkemper, T.; Dose, A.; Caballo Gonzalez, M.; Groenen, A. J. J.; Hehir, S.; Andrés-Guerrero, V.; Herrero Vanrell, R.; Cameron, N. R. *Macromol. Biosci.* **2015**, *15*, 138-145.
- (55) Zhao, W.; Gnanou, Y.; Hadjichristidis, N. *Chem. Commun.* **2015**, *51*, 3663-3666.
- (56) Zhao, W.; Gnanou, Y.; Hadjichristidis, N. *Biomacromolecules* **2015**, *16*, 1352-1357.
- (57) Zou, J.; Fan, J.; He, X.; Zhang, S.; Wang, H.; Wooley, K. L. *Macromolecules* **2013**, *46*, 4223-4226.
- (58) Deming, T. J. *Nat. Mater.* **2010**, *9*, 535-536.
- (59) Kopecek, J.; Yang, J. *Angew. Chem. Int. Ed.* **2012**, *51*, 7396-7417.
- (60) Babu, S. S.; Prasanthkumar, S.; Ajayaghosh, A. *Angew. Chem. Int. Ed.* **2012**, *51*, 1766-1776.
- (61) Suzuki, M.; Hanabusa, K. *Chem. Soc. Rev.* **2010**, *39*, 455-463.
- (62) Hartgerink, J. D.; Beniash, E.; Stupp, S. I. *Science* **2001**, *294*, 1684-1688.
- (63) Appel, E. A.; del Barrio, J.; Loh, X. J.; Scherman, O. A. *Chem. Soc. Rev.* **2012**, *41*, 6195-6214.
- (64) Banerjee, S.; Das, R. K.; Maitra, U. *J. Mater. Chem.* **2009**, *19*, 6649-6687.
- (65) Kim, K. T.; Park, C.; Vandermeulen, G. W. M.; Rider, D. A.; Kim, C.; Winnik, M. A.; Manners, I. *Angew. Chem. Int. Ed.* **2005**, *44*, 7964-7968.
- (66) Kim, K. T.; Park, C.; Kim, C.; Winnik, M. A.; Manners, I. *Chem. Commun.* **2006**, 1372-1374.
- (67) Gibson, M. I.; Cameron, N. R. *Angew. Chem. Int. Ed.* **2008**, *47*, 5160-5162.

- (68) Zou, J.; Zhang, F.; Chen, Y.; Raymond, J. E.; Zhang, S.; Fan, J.; Zhu, J.; Li, A.; Seetho, K.; He, X.; Pochan, D. J.; Wooley, K. L. *Soft Matter* **2013**, *9*, 5951-5958.
- (69) Rosler, A.; Klok, H. A.; Hamley, I. W.; Castelletto, V.; Mykhaylyk, O. O. *Biomacromolecules* **2003**, *4*, 859-863.
- (70) Choi, Y. Y.; Joo, M. K.; Sohn, Y. S.; Jeong, B. *Soft Matter* **2008**, *4*, 2383-2387.
- (71) Oh, H. J.; Joo, M. K.; Sohn, Y. S.; Jeong, B. *Macromolecules* **2008**, *41*, 8204-8209.
- (72) Kim, E. H.; Joo, M. K.; Bahk, K. H.; Park, M. H.; Chi, B.; Lee, Y. M.; Jeong, B. *Biomacromolecules* **2009**, *10*, 2476-2481.
- (73) Choi, Y. Y.; Jang, J. H.; Park, M. H.; Choi, B. G.; Chi, B.; Jeong, B. *J. Mater. Chem.* **2010**, *20*, 3416-3421.
- (74) Jang, J. H.; Choi, Y. M.; Choi, Y. Y.; Joo, M. K.; Park, M. H.; Choi, B. G.; Kang, E. Y.; Jeong, B. *J. Mater. Chem.* **2011**, *21*, 5484-5491.
- (75) Kang, E. Y.; Moon, H. J.; Joo, M. K.; Jeong, B. *Biomacromolecules* **2012**, *13*, 1750-1757.
- (76) Huang, J.; Hastings, C. L.; Duffy, G. P.; Kelly, H. M.; Raeburn, J.; Adams, D. J.; Heise, A. *Biomacromolecules* **2013**, *14*, 200-206.
- (77) Cheng, Y.; He, C.; Xiao, C.; Ding, J.; Cui, H.; Zhuang, X.; Chen, X. *Biomacromolecules* **2013**, *14*, 468-475.
- (78) Zhang, S.; Fu, W.; Li, Z. *Polym. Chem.* **2014**, *5*, 3346-3351.
- (79) He, X.; Fan, J.; Zhang, F.; Li, R.; Pollack, K. A.; Raymond, J. E.; Zou, J.; Wooley, K. L. *J. Mater. Chem. B* **2014**, *2*, 8123-8130.

- (80) Jeong, Y.; Joo, M. K.; Sohn, Y. S.; Jeong, B. *Adv. Mater.* **2007**, *19*, 3947-3950.
- (81) Hamley, I. W.; Daniel, C.; Mingvanish, W.; Mai, S. M.; Booth, C.; Messe, L.; Ryan, A. J. *Langmuir* **2000**, *16*, 2508-2514.
- (82) Liu, D.-L.; Chang, X.; Dong, C.-M. *Chem. Commun.* **2013**, *49*, 1229-1231.
- (83) Djabourov, M.; Leblond, J.; Papon, P. *J. Phys. France* **1988**, *49*, 319-332.
- (84) Petka, W. A.; Harden, J. L.; McGrath, K. P.; Wirtz, D.; Tirrell, D. A. *Science* **1998**, *281*, 389-392.
- (85) Tohyama, K.; Miller, W. G. *Nature* **1981**, *289*, 813-814.
- (86) Kuo, S.-W.; Lee, H.-F.; Huang, C.-F.; Huang, C.-J.; Chang, F.-C. *J. Polym. Sci. A Polym. Chem.* **2008**, *46*, 3108-3119.
- (87) Kotharangannagari, V. K.; Sánchez-Ferrer, A.; Ruokolainen, J.; Mezzenga, R. *Macromolecules* **2012**, *45*, 1982-1990.
- (88) Kim, J. Y.; Park, M. H.; Joo, M. K.; Lee, S. Y.; Jeong, B. *Macromolecules* **2009**, *42*, 3147-3151.
- (89) Cheng, Y.; He, C.; Xiao, C.; Ding, J.; Zhuang, X.; Huang, Y.; Chen, X. *Biomacromolecules* **2012**, *13*, 2053-2059.
- (90) Zhang, S.; Alvarez, D. J.; Sofroniew, M. V.; Deming, T. J. *Biomacromolecules* **2015**, *16*, 1331-1340.
- (91) Chen, C.; Wang, Z.; Li, Z. *Biomacromolecules* **2011**, *12*, 863.
- (92) Moon, H. J.; Choi, B. G.; Park, M. H.; Joo, M. K.; Jeong, B. *Biomacromolecules* **2011**, *12*, 1234-1242.

- (93) Joo, J. H.; Ko, D. Y.; Moon, H. J.; Shinde, U. P.; Park, M. H.; Jeong, B. *Biomacromolecules* **2014**, *15*, 3664-3670.
- (94) Cravotto, G.; Cintas, P. *Chem. Soc. Rev.* **2009**, *38*, 2684-2697.
- (95) Yu, X.; Chen, L.; Zhang, M.; Yi, T. *Chem. Soc. Rev.* **2014**, *43*, 5346-5371.
- (96) Naota, T.; Koori, H. *J. Am. Chem. Soc.* **2005**, *127*, 9324-9325.
- (97) Das Mahapatra, R.; Dey, J. *Langmuir* **2015**, *31*, 8703-8709.
- (98) Roth, P. J.; Quek, J. Y.; Zhu, Y.; Blunden, B. M.; Lowe, A. B. *Chem. Commun.* **2014**, *50*, 9561-9564.
- (99) Fan, J.; Zou, J.; He, X.; Zhang, F.; Zhang, S.; Raymond, J. E.; Wooley, K. L. *Chem. Sci.* **2014**, *5*, 141-150.
- (100) Zou, J.; He, X.; Fan, J.; Raymond, J. E.; Wooley, K. L. *Chem. Eur. J.* **2014**, *20*, 8842-8847.
- (101) Jeong, Y.; Joo, M. K.; Bahk, K. H.; Choi, Y. Y.; Kim, H.-T.; Kim, W.-K.; Jeong Lee, H.; Sohn, Y. S.; Jeong, B. *J. Control. Release* **2009**, *137*, 25-30.
- (102) Ohkawa, K.; Kitsuki, T.; Amaike, M.; Saitoh, H.; Yamamoto, H. *Biomaterials* **1998**, *19*, 1855-1860.
- (103) Sun, Y.; Hou, Y.; Zhou, X.; Yuan, J.; Wang, J.; Lu, H. *ACS Macro Lett.* **2015**, *4*, 1000-1003.
- (104) Ren, K.; He, C.; Cheng, Y.; Li, G.; Chen, X. *Polym. Chem.* **2014**, *5*, 5069-5076.
- (105) Haines, L. A.; Rajagopal, K.; Ozbas, B.; Salick, D. A.; Pochan, D. J.; Schneider, J. P. *J. Am. Chem. Soc.* **2005**, *127*, 17025-17029.
- (106) Li, X.; Gao, Y.; Kuang, Y.; Xu, B. *Chem. Commun.* **2010**, *46*, 5364-5366.



- (107) Ohkawa, K.; Shoumura, K.; Yamada, M.; Nishida, A.; Shirai, H.; Yamamoto, H. *Macromol. Biosci.* **2001**, *1*, 149-156.
- (108) Yamamoto, H.; Kitsuki, T.; Nishida, A.; Asada, K.; Ohkawa, K. *Macromolecules* **1999**, *32*, 1055-1061.
- (109) Huynh, D. P.; Nguyen, M. K.; Pi, B. S.; Kim, M. S.; Chae, S. Y.; Lee, K. C.; Kim, B. S.; Kim, S. W.; Lee, D. S. *Biomaterials* **2008**, *29*, 2527-2534.
- (110) Chen, Y.; Pang, X.-H.; Dong, C.-M. *Adv. Funct. Mater.* **2010**, *20*, 579-586.
- (111) Vacogne, C.; Brosnan, S.; Masic, A.; Schlaad, H. *Polym. Chem.* **2015**, *6*, 5040-5052.
- (112) Pang, X.; Wu, J.; Chu, C.-C.; Chen, X. *Acta Biomater.* **2014**, *10*, 3098-3107.
- (113) Nakahata, M.; Takashima, Y.; Yamaguchi, H.; Harada, A. *Nat. Commun.* **2011**, *2*.
- (114) Zhang, Y.; Zhang, B.; Kuang, Y.; Gao, Y.; Shi, J.; Zhang, X. X.; Xu, B. *J. Am. Chem. Soc.* **2013**, *135*, 5008-5011.
- (115) Yang, F.; Wang, J.; Cao, L.; Chen, R.; Tang, L.; Liu, C. *J. Mater. Chem. B* **2014**, *2*, 295-304.
- (116) Islam, M. R.; Gao, Y.; Li, X.; Serpe, M. J. *J. Mater. Chem. B* **2014**, *2*, 2444-2451.
- (117) Cui, H.; Liu, Y.; Cheng, Y.; Zhang, Z.; Zhang, P.; Chen, X.; Wei, Y. *Biomacromolecules* **2014**, *15*, 1115-1123.
- (118) Beebe, D. J.; Moore, J. S.; Bauer, J. M.; Yu, Q.; Liu, R. H.; Devadoss, C.; Jo, B.-H. *Nature* **2000**, *404*, 588-590.

- (119) Moon, H. J.; Ko, D. Y.; Park, M. H.; Joo, M. K.; Jeong, B. *Chem. Soc. Rev.* **2012**, *41*, 4860-4883.
- (120) He, M.; Li, J.; Tan, S.; Wang, R.; Zhang, Y. *J. Am. Chem. Soc.* **2013**, *135*, 18718-18721.
- (121) Kozlovskaya, V.; Chen, J.; Tedjo, C.; Liang, X.; Campos-Gomez, J.; Oh, J.; Saeed, M.; Lungu, C. T.; Kharlampieva, E. *J. Mater. Chem. B* **2014**, *2*, 2494-2507.
- (122) Li, J.; Gao, Y.; Kuang, Y.; Shi, J.; Du, X.; Zhou, J.; Wang, H.; Yang, Z.; Xu, B. *J. Am. Chem. Soc.* **2013**, *135*, 9907-9914.
- (123) Yan, B.; Boyer, J.-C.; Habault, D.; Branda, N. R.; Zhao, Y. *J. Am. Chem. Soc.* **2012**, *134*, 16558-16561.
- (124) Huang, J.; Heise, A. *Chem. Soc. Rev.* **2013**, *42*, 7373-7390.
- (125) Hunt, J. N.; Feldman, K. E.; Lynd, N. A.; Deek, J.; Campos, L. M.; Spruell, J. M.; Hernandez, B. M.; Kramer, E. J.; Hawker, C. J. *Adv. Mater.* **2011**, *23*, 2327-2331.
- (126) Fraix, A.; Gref, R.; Sortino, S. *J. Mater. Chem. B* **2014**, *2*, 3443-3449.
- (127) Zhuang, J.; Gordon, M. R.; Ventura, J.; Li, L.; Thayumanavan, S. *Chem. Soc. Rev.* **2013**, *42*, 7421-7435.
- (128) Nguyen, M. K.; Huynh, C. T.; Gao, G. H.; Kim, J. H.; Huynh, D. P.; Chae, S. Y.; Lee, K. C.; Lee, D. S. *Soft Matter* **2011**, *7*, 2994-3001.
- (129) Xu, X.-D.; Liang, L.; Cheng, H.; Wang, X.-H.; Jiang, F.-G.; Zhuo, R.-X.; Zhang, X.-Z. *J. Mater. Chem.* **2012**, *22*, 18164-18171.

- (130) Purcell, B. P.; Lobb, D.; Charati, M. B.; Dorsey, S. M.; Wade, R. J.; Zellars, K. N.; Doviak, H.; Pettaway, S.; Logdon, C. B.; Shuman, J. A.; Freels, P. D.; Gorman Iii, J. H.; Gorman, R. C.; Spinale, F. G.; Burdick, J. A. *Nat. Mater.* **2014**, *13*, 653-661.
- (131) Giano, M. C.; Pochan, D. J.; Schneider, J. P. *Biomaterials* **2011**, *32*, 6471-6477.
- (132) Adams, D. J.; Topham, P. D. *Soft Matter* **2010**, *6*, 3707-3721.
- (133) Kuang, Y.; Xu, B. *Angew. Chem. Int. Ed.* **2013**, *52*, 6944-6948.
- (134) Aggeli, A.; Bell, M.; Boden, N.; Keen, J. N.; Knowles, P. F.; McLeish, T. C. B.; Pitkeathly, M.; Radford, S. E. *Nature* **1997**, *386*, 259-262.
- (135) Chen, C.; Wu, D.; Fu, W.; Li, Z. *Biomacromolecules* **2013**, *14*, 2494-2498.
- (136) Thornton, P. D.; Billah, S. M. R.; Cameron, N. R. *Macromol. Rapid Comm.* **2013**, *34*, 257-262.
- (137) Sun, J.; Schlaad, H. *Macromolecules* **2010**, *43*, 4445-4448.
- (138) Kang, E. Y.; Yeon, B.; Moon, H. J.; Jeong, B. *Macromolecules* **2012**, *45*, 2007-2013.
- (139) Oelker, A. M.; Morey, S. M.; Griffith, L. G.; Hammond, P. T. *Soft Matter* **2012**, *8*, 10887-10895.
- (140) Joo, M. K.; Ko, D. Y.; Jeong, S. J.; Park, M. H.; Shinde, U. P.; Jeong, B. *Soft Matter* **2013**, *9*, 8014-8022.
- (141) Lee, C.-U.; Lu, L.; Chen, J.; Garno, J. C.; Zhang, D. *ACS Macro Lett.* **2013**, *2*, 436-440.
- (142) Krannig, K.-S.; Doriti, A.; Schlaad, H. *Macromolecules* **2014**, *47*, 2536-2539.
- (143) Miyazawa, T.; Masuda, Y.; Fukushima, K. *J. Polym. Sci.* **1962**, *62*, S62-S64.

- (144) Panitch, A.; Matsuki, K.; Cantor, E. J.; Cooper, S. J.; Atkins, E. D. T.; Fournier, M. J.; Mason, T. L.; Tirrell, D. A. *Macromolecules* **1997**, *30*, 42-49.
- (145) Kirschner, D. A.; Abraham, C.; Selkoe, D. J. *Proc. Natl. Acad. Sci. U.S.A.* **1986**, *83*, 503-507.
- (146) Shao, H.; Nguyen, T.; Romano, N. C.; Modarelli, D. A.; Parquette, J. R. *J. Am. Chem. Soc.* **2009**, *131*, 16374-16376.
- (147) Castelletto, V.; Cheng, G.; Furzeland, S.; Atkins, D.; Hamley, I. W. *Soft Matter* **2012**, *8*, 5434-5438.
- (148) Lin, Y.-A.; Ou, Y.-C.; Cheetham, A. G.; Cui, H. *Biomacromolecules* **2014**, *15*, 1419-1427.
- (149) Top, A.; Roberts, C. J.; Kiick, K. L. *Biomacromolecules* **2011**, *12*, 2184-2192.
- (150) Iijima, S. *Nature* **1991**, *354*, 56-58.
- (151) Shulaker, M. M.; Hills, G.; Patil, N.; Wei, H.; Chen, H.-Y.; PhilipWong, H.-S.; Mitra, S. *Nature* **2013**, *501*, 526-530.
- (152) Subramaniam, C.; Yamada, T.; Kobashi, K.; Sekiguchi, A.; Futaba, D. N.; Yumura, M.; Hata, K. *Nat. Commun.* **2013**, *4*, 2202.
- (153) Franklin, A. D.; Luisier, M.; Han, S. J.; Tulevski, G.; Breslin, C. M.; Gignac, L.; Lundstrom, M. S.; Haensch, W. *Nano Lett.* **2012**, *12*, 758-762.
- (154) Brunetti, F. G.; Romero-Nieto, C.; López-Andarias, J.; Atienza, C.; López, J. L.; Guldi, D. M.; Martín, N. *Angew. Chem. Int. Ed.* **2013**, *52*, 2180-2184.
- (155) Yang, L.; Wang, S.; Zeng, Q.; Zhang, Z.; Peng, L.-M. *Small* **2013**, *9*, 1225-1236.
- (156) Liu, Y.; Wang, X.; Qi, K.; Xin, J. H. *J. Mater. Chem.* **2008**, *18*, 3454-3460.

- (157) Chen, T.; Wang, S.; Yang, Z.; Feng, Q.; Sun, X.; Li, L.; Wang, Z.-S.; Peng, H. *Angew. Chem. Int. Ed.* **2011**, *50*, 1815-1819.
- (158) Peng, H. *J. Am. Chem. Soc.* **2008**, *130*, 42-43.
- (159) Peng, H.; Sun, X.; Cai, F.; Chen, X.; Zhu, Y.; Liao, G.; Chen, D.; Li, Q.; Lu, Y.; Zhu, Y.; Jia, Q. *Nat Nanotechnol* **2009**, *4*, 738-741.
- (160) Calvaresi, M.; Zerbetto, F. *Acc. Chem. Res.* **2013**, *46*, 2454-2463.
- (161) Yang, Y.; Gupta, M. C. *Nano Lett.* **2005**, *5*, 2131-2134.
- (162) Kam, N. W. S.; O'Connell, M.; Wisdom, J. A.; Dai, H. *Proc. Natl. Acad. Sci. U.S.A.* **2005**, *102*, 11600-11605.
- (163) Liu, Z.; Chen, K.; Davis, C.; Sherlock, S.; Cao, Q.; Chen, X.; Dai, H. *Cancer Res.* **2008**, *68*, 6652-6660.
- (164) Harrison, B. S.; Atala, A. *Biomaterials* **2007**, *28*, 344-353.
- (165) Ji, S.-R.; Liu, C.; Zhang, B.; Yang, F.; Xu, J.; Long, J. A.; Jin, C.; Fu, D.-L.; Ni, Q.-X.; Yu, X.-J. *Biochim. Biophys. Acta* **2010**, *1806*, 29-35.
- (166) Yu, H.; Hermann, S.; Schulz, S. E.; Gessner, T.; Dong, Z.; Li, W. J. *Chem. Phys.* **2012**, *408*, 11-16.
- (167) Tasis, D.; Tagmatarchis, N.; Bianco, A.; Prato, M. *Chem. Rev.* **2006**, *106*, 1105-1136.
- (168) Grossiord, N.; Loos, J.; Regev, O.; Koning, C. E. *Chem. Mater.* **2006**, *18*, 1089-1099.
- (169) Hirsch, A. *Angew. Chem. Int. Ed.* **2002**, *41*, 1853-1859.

- (170) Lee, J. J.; Yamaguchi, A.; Alam, M. A.; Yamamoto, Y.; Fukushima, T.; Kato, K.; Takata, M.; Fujita, N.; Aida, T. *Angew. Chem. Int. Ed.* **2012**, *51*, 8490-8494.
- (171) Fukushima, T.; Kosaka, A.; Ishimura, Y.; Yamamoto, T.; Takigawa, T.; Ishii, N.; Aida, T. *Science* **2003**, *300*, 2072-2074.
- (172) Tuncel, D. *Nanoscale* **2011**, *3*, 3545-3554.
- (173) Chen, R. J.; Zhang, Y.; Wang, D.; Dai, H. *J. Am. Chem. Soc.* **2001**, *123*, 3838-3839.
- (174) Cao, L.; Chen, H.-Z.; Zhou, H.-B.; Zhu, L.; Sun, J.-Z.; Zhang, X.-B.; Xu, J.-M.; Wang, M. *Adv. Mater.* **2003**, *15*, 909-913.
- (175) Sprafke, J. K.; Stranks, S. D.; Warner, J. H.; Nicholas, R. J.; Anderson, H. L. *Angew. Chem. Int. Ed.* **2011**, *50*, 2313-2316.
- (176) Jain, D.; Saha, A.; Marti, A. A. *Chem. Commun.* **2011**, *47*, 2246-2248.
- (177) Li, Q. W.; Zhang, J.; Yan, H.; He, M. S.; Liu, Z. F. *Carbon* **2004**, *42*, 287-291.
- (178) Dodziuk, H.; Ejchart, A.; Anczewski, W.; Ueda, H.; Krinichnaya, E.; Dolgonos, G.; Kutner, W. *Chem. Commun.* **2003**, 986-987.
- (179) Tu, X.; Manohar, S.; Jagota, A.; Zheng, M. *Nature* **2009**, *460*, 250-253.
- (180) Du, F.; Fischer, J. E.; Winey, K. I. *J. Polym. Sci. B Polym. Phys.* **2003**, *41*, 3333-3338.
- (181) Jin, L.; Bower, C.; Zhou, O. *Appl. Phys. Lett.* **1998**, *73*, 1197-1199.
- (182) Rice, N. A.; Adronov, A. *Macromolecules* **2013**, *46*, 3850-3860.
- (183) Srinivasan, S.; Babu, S. S.; Praveen, V. K.; Ajayaghosh, A. *Angew. Chem. Int. Ed.* **2008**, *47*, 5746-5749.

- (184) Liang, S.; Zhao, Y.; Adronov, A. *J. Am. Chem. Soc.* **2013**, *136*, 970-977.
- (185) Olivier, J.-H.; Deria, P.; Park, J.; Kumbhar, A.; Andrian-Albescu, M.; Therien, M. J. *Angew. Chem. Int. Ed.* **2013**, *52*, 13080-13085.
- (186) Ding, W.; Eitan, A.; Fisher, F. T.; Chen, X.; Dikin, D. A.; Andrews, R.; Brinson, L. C.; Schadler, L. S.; Ruoff, R. S. *Nano Lett.* **2003**, *3*, 1593-1597.
- (187) Sitharaman, B.; Shi, X.; Walboomers, X. F.; Liao, H.; Cuijpers, V.; Wilson, L. J.; Mikos, A. G.; Jansen, J. A. *Bone* **2008**, *43*, 362-370.
- (188) Montenegro, J.; Vázquez-Vázquez, C.; Kalinin, A.; Geckeler, K. E.; Granja, J. R. *J. Am. Chem. Soc.* **2014**, *136*, 2484-2491.
- (189) Tang, H.; Zhang, D. *J. Polym. Sci. A Polym. Chem.* **2013**, *51*, 4489-4497.
- (190) Arnold, M. S.; Guler, M. O.; Hersam, M. C.; Stupp, S. I. *Langmuir* **2005**, *21*, 4705-4709.
- (191) Zorbas, V.; Ortiz-Acevedo, A.; Dalton, A. B.; Yoshida, M. M.; Dieckmann, G. R.; Draper, R. K.; Baughman, R. H.; Jose-Yacaman, M.; Musselman, I. H. *J. Am. Chem. Soc.* **2004**, *126*, 7222-7227.
- (192) Wang, S.; Humphreys, E. S.; Chung, S.-Y.; Delduco, D. F.; Lustig, S. R.; Wang, H.; Parker, K. N.; Rizzo, N. W.; Subramoney, S.; Chiang, Y.-M.; Jagota, A. *Nat. Mater.* **2003**, *2*, 196-200.
- (193) Dieckmann, G. R.; Dalton, A. B.; Johnson, P. A.; Razal, J.; Chen, J.; Giordano, G. M.; Munoz, E.; Musselman, I. H.; Baughman, R. H.; Draper, R. K. *J. Am. Chem. Soc.* **2003**, *125*, 1770-1777.
- (194) Jeong, W. J.; Lim, Y. B. *Macromol. Biosci.* **2012**, *12*, 49-54.

- (195) Shvartzman-Cohen, R.; Nativ-Roth, E.; Baskaran, E.; Levi-Kalisman, Y.; Szleifer, I.; Yerushalmi-Rozen, R. *J. Am. Chem. Soc.* **2004**, *126*, 14850-14857.
- (196) Mandal, S. K.; Kar, T.; Das, P. K. *Chem. Eur. J.* **2013**, *19*, 12486-12496.
- (197) Du, X.; Li, J.; Welle, A.; Li, L.; Feng, W.; Levkin, P. A. *Adv. Mater.* **2015**, *27*, 4997-5001.
- (198) Gandavarapu, N. R.; Azagarsamy, M. A.; Anseth, K. S. *Adv. Mater.* **2014**, *26*, 2521-2526.
- (199) Arumugam, S.; Popik, V. V. *J. Am. Chem. Soc.* **2012**, *134*, 8408-8411.
- (200) Draper, E. R.; Eden, E. G. B.; McDonald, T. O.; Adams, D. J. *Nat. Chem.* **2015**, *7*, 848-852.
- (201) Cornwell, D. J.; Daubney, O. J.; Smith, D. K. *J. Am. Chem. Soc.* **2015**, *137*, 15486–15492.
- (202) Yan, X.; Wang, F.; Zheng, B.; Huang, F. *Chem. Soc. Rev.* **2012**, *41*, 6042-6065.
- (203) Du, J.; Pei, S.; Ma, L.; Cheng, H.-M. *Adv. Mater.* **2014**, *26*, 1958-1991.
- (204) Sun, G.; Cho, S.; Clark, C.; Verkhoturov, S. V.; Eller, M. J.; Li, A.; Pavía-Jiménez, A.; Schweikert, E. A.; Thackeray, J. W.; Trefonas, P.; Wooley, K. L. *J. Am. Chem. Soc.* **2013**, *135*, 4203-4206.
- (205) Smits, F. M. *Bell Syst. Tech. J.* **1958**, *37*, 711-718.
- (206) He, X.; Fan, J.; Wooley, K. L. *Chem. Asian J.* **2016**, *11*, 437-447.
- (207) Wen, J.; Xu, Y.; Li, H.; Lu, A.; Sun, S. *Chem. Commun.* **2015**, *51*, 11346-11358.
- (208) Huang, S.; Zhao, C.; Pan, W.; Cui, Y.; Wu, H. *Nano Lett.* **2015**, *15*, 1609-1614.



- (209) Habisreutinger, S. N.; Leijtens, T.; Eperon, G. E.; Stranks, S. D.; Nicholas, R. J.; Snaith, H. J. *Nano Lett.* **2014**, *14*, 5561-5568.
- (210) Zhang, X.; Yu, Z.; Wang, C.; Zarrouk, D.; Seo, J.-W. T.; Cheng, J. C.; Buchan, A. D.; Takei, K.; Zhao, Y.; Ager, J. W.; Zhang, J.; Hettick, M.; Hersam, M. C.; Pisano, A. P.; Fearing, R. S.; Javey, A. *Nat. Commun.* **2014**, *5*, 2983.
- (211) Liang, C.; Diao, S.; Wang, C.; Gong, H.; Liu, T.; Hong, G.; Shi, X.; Dai, H.; Liu, Z. *Adv. Mater.* **2014**, *26*, 5646-5652.
- (212) Chen, P.-Y.; Hyder, M. N.; Mackanic, D.; Courchesne, N.-M. D.; Qi, J.; Klug, M. T.; Belcher, A. M.; Hammond, P. T. *Adv. Mater.* **2014**, *26*, 5101-5107.
- (213) Byrne, M. T.; Gun'ko, Y. K. *Adv. Mater.* **2010**, *22*, 1672-1688.
- (214) Samanta, S. K.; Fritsch, M.; Scherf, U.; Gomulya, W.; Bisri, S. Z.; Loi, M. A. *Acc. Chem. Res.* **2014**, *47*, 2446-2456.
- (215) Haggemueller, R.; Rahatekar, S. S.; Fagan, J. A.; Chun, J.; Becker, M. L.; Naik, R. R.; Krauss, T.; Carlson, L.; Kadla, J. F.; Trulove, P. C.; Fox, D. F.; DeLong, H. C.; Fang, Z.; Kelley, S. O.; Gilman, J. W. *Langmuir* **2008**, *24*, 5070-5078.
- (216) Liu, H.; Nishide, D.; Tanaka, T.; Kataura, H. *Nat. Commun.* **2011**, *2*, 309.
- (217) Backes, C.; Hauke, F.; Hirsch, A. *Adv. Mater.* **2011**, *23*, 2588-2601.
- (218) Shi, Y.; Wang, M.; Ma, C.; Wang, Y.; Li, X.; Yu, G. *Nano Lett.* **2015**, *15*, 6276-6281.